공학박사 학위논문

Development of Skin-mountable Bio-integrated Sensors, Charge-trap Memory, and Quantum-dot Information Display

피부 부착이 가능한 생체 통합 센서, 전하 트랩 메모리, 및 양자점 정보 디스플레이의 개발

2017 년 2 월

서울대학교 대학원

화학생물공학부

김 재 민

Development of Skin-mountable Bio-integrated Sensors, Charge-trap Memory, and Quantum-dot Information Display

지도교수 김 대 형

이 논문을 공학박사 학위논문으로 제출함

2017 년 1 월

서울대학교 대학원

화학생물공학부

김 재 민

김재민의 박사학위논문을 인준함

2017 년 1 월

위 원 장 성 영은 (인)

부 위 원 장 김 대 형 (인)

위 원 현 택환 (인)

위 원 이 탁희 (인)

위 원 이 민백 (인)

Abstract

Development of Skin-mountable Bio-integrated Sensors, Charge-trap Memory, and Quantum-dot Information Display

Jaemin Kim
School of Chemical and Biological Engineering
The Graduate School
Seoul National University

Recently, many researchers have devoted significant efforts to develop flexible/stretchable biomedical devices because many physiological data can be obtained by installing electronic devices on human body. However, the soft and curvilinear human skin makes the integration of rigid electronic devices with it challenging, which induces the need for the deformability of electronic devices. In this regard, inherently flexible materials such as semiconducting organic materials as well as materials that are not intrinsically flexible, but possess the flexibility owing to their ultrathin and/or tiny form factors, such as nanoparticles, nanowires and nanoribbons, have been widely incorporated as active materials for

flexible/stretchable electronics. This dissertation includes three examples of skin-like devices which incorporate such nanomaterials for various purposes.

First, smart prosthetic skin instrumented with ultrathin, single crystalline silicon nanoribbon strain, pressure, and temperature sensor arrays as well as associated humidity sensors, electroresistive heaters, and stretchable multi-electrode arrays for nerve stimulation are demonstrated. This collection of stretchable sensors and actuators facilitate highly localized mechanical and thermal skin-like perception in response to external stimuli, thus providing unique opportunities for emerging classes of prostheses and peripheral-nervous-system interface technologies.

Second, a wearable fully multiplexed silicon nonvolatile memory array with nanocrystal floating gates is developed. The nanocrystal monolayer is assembled over a large area using the Langmuir-Blodgett method. Efficient particle-level charge confinement is verified by the modified atomic force microscopy technique. Uniform nanocrystal charge traps evidently improve the memory window margin and retention performance. Furthermore, the multiplexing of memory devices in conjunction with the amplification of sensor signals based on ultrathin silicon nanomembrane circuits in stretchable layouts enables wearable healthcare applications such as long-term data storage of monitored heart rates.

Third, an ultra-thin skin-like quantum dot (QD) light-emitting diode (QLED) display is developed. The key materials, QDs, are well optimized through intensive engineering to achieve high brightness with a low

operation voltage. To validate the fabricated QLED display, various patterns, including those comprised of letters, numbers, symbols, and animations are visualized using the proposed QLED display conformally laminated on human skin. Furthermore, the QLED display is subjected to various mechanical deformations, such as crumpling and repeated bending to demonstrate its reliability-in-use. Finally, the QLED display is integrated with conventional flexible electronic circuits for constructing a stand-alone wearable display that can directly visualize measured data against the user's skin.

The abovementioned three examples are important electronic components for future skin-like wearable devices. The advances introduced in this dissertation may create new opportunities in the field of deformable sensors, actuators, data storage devices, and displays, thereby accelerating the development of fully integrated skin-like electronic devices.

Keywords: Flexible electronics, Stretchable electronics, Wearable electronics, Wearable sensor, Wearable memory, Wearable Display

***Student Number*: 2012-30955**

Contents

List of Figures

Chapter 1. Recent advances in deformable devices with integrated functional nanomaterials for wearable electronics

Preface

As the market and related industry for wearable electronics dramatically expands, there are continuous and strong demands for flexible and stretchable devices to be seamlessly integrated with soft and curvilinear human skin or clothes. However, the mechanical mismatch between the rigid conventional electronics and the soft human body causes many problems. Therefore, various prospective nanomaterials that possess a much lower flexural rigidity than their bulk counterparts have rapidly established themselves as promising electronic materials replacing rigid silicon and/or compound semiconductors in next-generation wearable devices. Many hybrid structures of multiple nanomaterials have been also developed to pursue both high performance and multifunctionality. Here, I provide an overview of state-of-the-art wearable devices based on one- or two-dimensional nanomaterials (*e.g.*, carbon nanotubes, graphene, single-crystal silicon and oxide nanomembranes, and their hybrids) in combination with zero-dimensional functional nanomaterials (*e.g.*, metal/oxide nanoparticles and quantum dots). Starting from an introduction of materials strategies, I describe device designs and the roles of

individual ones in integrated systems. Detailed application examples of wearable sensors/actuators, memories, and displays are also presented.

*** The contents of this chapter were published in *Nano Convergence*, 2016, *3*, 4.**

1.1 Introduction

In the rapid technology development of low-power silicon electronics, various wearable electronic devices such as smart glasses, watches, and lenses have been unveiled both in academic journals and on the market. In spite of their superb performance, wearable form factors, and compact size, challenges still remain mainly owing to their large thickness and mechanical rigidity, which result in a mechanical mismatch between the device and the skin. This mismatch induces a low signal-to-noise ratio, and measurement errors.[1] In this regard, achieving mechanical deformability of the wearable electronic/optoelectronic devices while maintaining high performances has been a major research goal.[2-6]

One promising strategy is to replace the rigid electronic materials (*e.g.*, silicon wafer) with flexible nanomaterials (*e.g.*, silicon nanomembrane (SiNM),[7-11] carbon nanotubes (CNTs)[12-14] and graphene (GP)[1, 15, 16]). The electronic properties of the SiNM (down to tens of nanometers) remain the same as the bulk silicon wafer,[17] but its bendability dramatically increases owing to the reduced thickness.[5] SiNM-based devices outperform their competitors including low-temperature polycrystalline silicon (LTPS) and organic devices by virtue of their high electron mobility.[18] However, SiNM alone may not be fully compatible with the multifunctionality required for some applications. Meanwhile, carbon nanomaterials (*e.g.*, CNTs and GP)[19, 20] have been getting attentions as next-generation semiconducting nanomaterials. The mobilities

of single-walled CNTs (SWNTs) and exfoliated GP have been reported up to 100,000[19] and 230,000 cm^2 V^{-1} s^{-1}, [20] respectively, which are much higher than that of single-crystal silicon. Their ultrathin thickness enables them to be seamlessly integrated in wearable devices while achieving the transparency.[21-23] The mass production, device performance, and fabrication processes of these carbon nanomaterials, however, have many remaining challenges for commercial device applications.[24]

Another approach to achieve both high performance and multifunctionality is to utilize hybrids of nanomaterials.[25-29] Functional hybrid nanomaterials often exhibit substantially different physical, mechanical, magnetic, chemical, and optical properties compared to their individual and/or bulk counterparts.[30-33] By integrating different functional nanomaterials, the performance of wearable devices can be dramatically improved and/or diversified.[1, 7, 34-39] For the realization of this goal, the type, size, thickness, and concentration of the nanomaterials should be carefully designed.[39] In the following, recently reported wearable sensors/actuators,[7, 13, 40] memories,[34, 41] and displays[42, 43] that exploit various nanomaterials[7, 37, 39, 44, 45] and their hybrids (Figure 1) are summarized. In addition, the roles of each nanomaterial in specific devices, integration methods are described, and brief perspectives on future research directions are also provided.

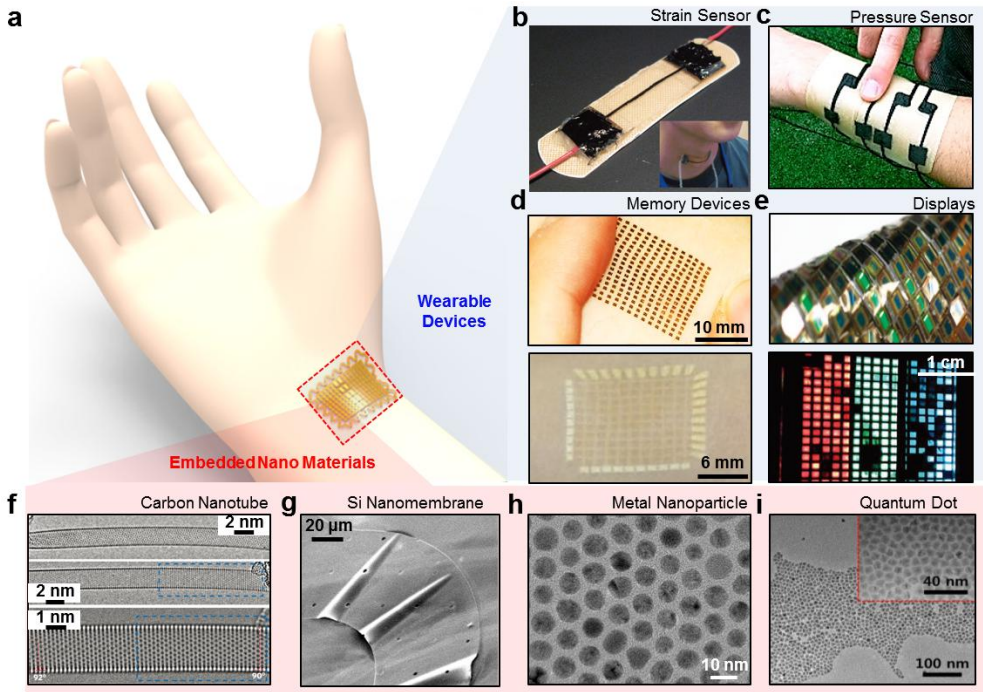

Figure 1.1. Overview of wearable devices with integrated nanomaterials. a, Schematic of a wearable device mounted on human skin. **b–e,** Optical images of representative wearable devices consisting of functional nanomaterials: **b,** strain sensor;[13] **c,** pressure sensor;[40] **d,** memory arrays;[34, 41] and **e,** displays.[42, 43] **f–i,** Transmission/scanning electron microscopy (TEM/SEM) images of representative functional nanomaterials integrated into wearable devices: **f,** CNTs;[44] **g,** an SiNM;[7] **h,** metal nanoparticles;[39] and **i,** quantum dots.[37]

1.2. Wearable Sensors and Actuators

Wearable sensors/actuators have recently attracted considerable interest because of their mobile healthcare[46] and virtual reality applications.[47] Sensors/actuators worn on the body, in particular, have drawn attention for the continuous and accurate monitoring of physiological (*e.g.*, motion[1, 40] and temperature[48, 49]) and electrophysiological (*e.g.*, electrocardiograms[50, 51] and electromyograms[52, 53]) signals and appropriate instant feedback on them[1], which are important for point-of-care medical diagnostics and therapy. This section describes representative wearable sensors/actuators based on functional nanomaterials and their application examples in healthcare and human–machine interfaces.

1.2.1. SiNM-based sensors

Deformability, which is one of the key characteristics of wearable electronics, can be achieved by making inorganic materials (*i.e.* silicon) as thin as possible, down to the nanometer scale (*i.e.* nanomembrane).[5] SiNM can be fabricated through several processes. One easy fabrication method is to remove the buried oxide of a silicon-on-insulator (SOI) wafer and pick the top part up or to etch the bottom silicon of the SOI wafer and use the remaining top part.[7] The obtained SiNM can be located in the desired position of the designed layout by using previously reported transfer printing techniques.[3] SiNM maintains the high carrier mobility[18]

and intrinsic piezoresistivity[7] of the bulk monocrystalline silicon, while having a high flexibility, which enables diverse wearable electronics applications.

For instance, multiplexing through SiNM transistors integrated into the flexible high-density electrode array achieves the real-time analysis of electrophysiological signals over a large area of the brain[10] and heart[54] surface. SiNM strain gauges integrated onto polymeric substrates are applied as wearable motion sensors thanks to their high piezoresistive sensitivity.[7, 8] Figure 2a shows images of a SiNM strain gauge array integrated with a finger tube that conforms to the thumb. The bending motion of the thumb applies a tensile stress to the SiNM strain gauges, and their resistance increases accordingly without any hysteresis (Figure 2b). Multiplexing by SiNM p-i-n junction (PIN) diodes is also advantageous for constructing a wearable high-spatial-resolution temperature sensor array. Figure 2c depicts an 8 × 8 PIN diode array located on a heated Cu element (left) and its measured temperature distribution (right). The rectifying characteristics of SiNM PIN diodes enable each cell to be individually addressable with the minimum number of wires and crosstalk, achieving a high spatial resolution. The ultrathin dimensions of the sensor array facilitate not only conformal contacts with the target surface but also a fast response time by virtue of its extremely low thermal mass.

By combining the SiNM strain gauge, pressure sensor, and temperature sensor array in a single platform, a skin-like device conformally mounted onto a prosthetic limb is demonstrated.[7] For decades,

prosthetic limbs have been used mostly for cosmetic purposes, replacing lost limbs of amputees. To enhance quality of life, prosthetic limbs fitted with wearable platform of sensors for mimicking the sensory reception of actual human skin have become a central area of research. Although significant progress has been made in flexible and stretchable electronics and their wearable applications, there still remain limitations in their sensitivity, spatial resolution, deformability, and detection ranges. Therefore, a novel integrated electronic skin platform considering site-specifically different deformation ranges of skin is highly needed. Chapter 2 describes a skin prosthesis that incorporates site-specifically optimized silicon nanoribbons (SiNRs) having spatio-temporal strain, pressure, and temperature sensing capabilities, as well as associated humidity sensors and electro-resistive heaters to mimic the actual skin.

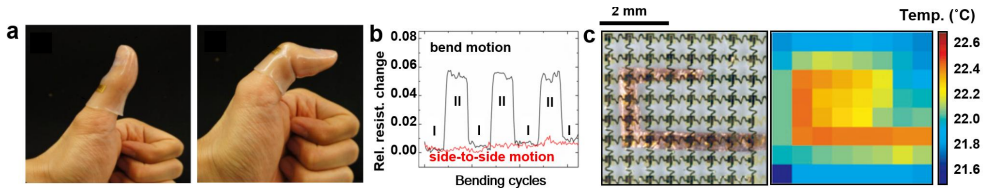

Figure 1.2. SiNM-based wearable sensors. a, SiNM-based strain gauge array on a polymer-based finger tube mounted on a relaxed (left) and bent thumb (right).[8] **b,** Relative change in the resistance of the SiNM strain gauge according to the bending (black) and side-to-side (red) motion of the thumb.[8] **c,** SiNM-diode-based wearable temperature sensor located on a heated metal element (left) and the measured temperature distribution (right).[49]

1.2.2. CNT-based wearable sensors

The macroscopic form of CNTs in most devices is either their aligned arrays or random networks. Hata *et al.* developed a synthesis method for ultra-long vertically aligned CNTs using the water-assisted chemical vapor deposition (CVD) process.[12] The vertically aligned CNTs could be selectively grown on a patterned catalyst layer and transferred onto a stretchable substrate for device applications such as a strain sensor (Figure 3a).[13] In this strain measurement, the CNT film deforms as the substrate is stretched and its resistance increases. This relative change in the resistance according to the applied strain can be used for human-motion detection. When the sensor is attached to a human knee, the change in the resistance exhibits variations corresponding to the wearer's motion (Figure 3b). Although vertical CNTs are densely aligned similar to a forest and therefore have a dark color, randomly oriented CNT networks are relatively transparent, particularly at reduced CNT concentrations.[14] Figure 3c shows a schematic of a transparent patch-type strain sensor using random-network CNTs integrated with a conducting polymer. By virtue of its optical transparency (62%), it was inconspicuously patched onto a human face and successfully distinguished facial motions (Figures 3d–f).

CNTs are also excellent nanoscale filler materials owing to their small size with good dispersion and exceptional electrical and physical properties.[55, 56] In this regard, electrically conductive rubber (ECR), which

is a composite of CNTs and elastomeric polymers, is prepared and used for a wearable mechanical sensor.[40] To enhance the sensitivity, nanopores and micropores are introduced into the ECR, thereby increasing its piezoresistivity and maximizing the locally induced strain when deformed.[40] Figure 3g shows a representative method for introducing pores with a uniform size and distribution in the ECR. The key idea of this method is to use a reverse micelle solution (RMS) comprising an emulsifier, deionized (DI) water, and an organic solvent. In accordance with careful sequential heat treatments, the migration and merging of the reverse micelles and subsequent pore generations occur (Figure 3h). A larger porosity and lower elastic modulus are achieved if a larger amount of solvent is included in the RMS, thereby resulting in a higher pressure sensitivity (Figure 3i). An ECR-based strain gauge fabricated on a medical bandage by using ink-jet printing forms a conformal contact with the human wrist and successfully monitors wrist motions. Although sensors based on CNT networks/composites are relatively cheap, especially those that are solution-processed, and mechanically compatible when worn on the human body, several issues such as a slow response time, a large area uniformity, and the hysteresis and drift of signals still need to be solved.

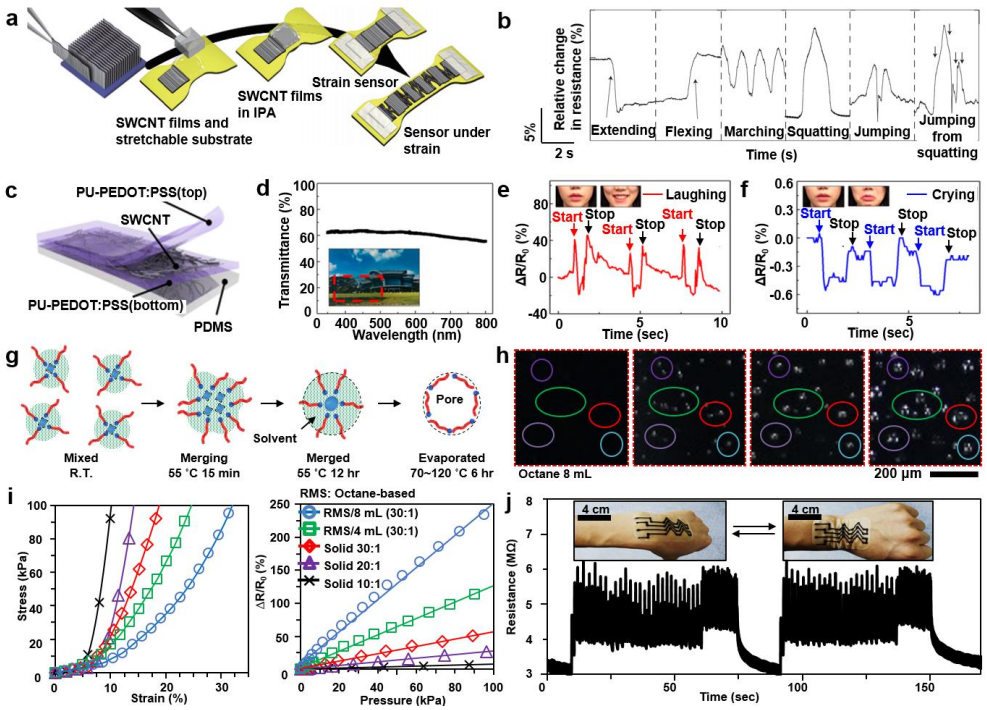

Figure 1.3. CNT-based wearable sensors. a, Schematic of the fabrication process of the aligned CNT strain sensor.[13] **b,** Relative change in the resistance of the strain sensor patched onto the knee depending on his/her specific movements.[13] **c,** Schematic exploded view of the transparent patchable strain gauge.[14] **d,** Transmittance of the strain gauge depending on the wavelength and a photograph showing the device placed on a picture (inset).[14] **e–f,** Relative change in the resistance of the strain sensor patched onto the face while **e,** he/she is laughing and **f,** crying.[14] **g,** Schematics of the pore generation process according to the heat treatment conditions.[40] **h,** Successive images of the ECR under heat treatment, showing the gradually forming pores inside.[40] **i,** Stress–strain curves of various types of ECRs, obtained by deforming them and measuring the

strain and applied stress (left), and the relative change in the resistance of the ECRs with respect to the applied pressure (right).[40] **j,** Change in the resistance of the wearable porous ECRs according to the repetitive bending and relaxing motions of the wrist.[40]

1.2.3. Wearable sensors/actuators based on nanomaterial hybrids

In several cases, electronic materials having a relatively poor performance are unavoidably utilized owing to the limited processing temperature and chemical resistance of plastic substrates.[57] Appropriately chosen functional nanomaterials can compensate for these limitations and improve the device performance.[39] Figure 4a shows a transparent piezoelectric motion sensor and electrotactile stimulator (inset) conformally laminated onto the human skin. The piezoelectric motion sensor consists of GP layers as the transparent electrodes, polylactic acid (PLA) as the piezoelectric material, and SWNTs as the piezoelectric performance enhancer (Figure 4b, left). Moreover, the electrotactile stimulator utilizes doped GP layers as transparent electrodes and silver nanowires (AgNWs) as a conductivity enhancer (Figure 4b, right). The strain-induced charge separation in PLA is the main mechanism for piezoelectric energy generation. The local increase in the modulus by the CNTs increases the locally induced strain inside PLA under deformation, which maximizes charge generation (Figure 4c). Figure 4d shows the conductivity enhancement by AgNWs sandwiched between GP layers. The enhanced conductivity of the GP/AgNWs/GP hybrid contributes to effective electrotactile stimulation (Figure 4e).

Figure 4f shows an illustration and optical image (inset) of a semitransparent piezoelectric strain sensor and resistive temperature sensor for measuring wrist motions and body-temperature changes for wheelchair

control and hypothermia diagnosis, respectively. The strain sensor consists of a ZnO nanomembrane as the piezoelectric material and SWNT networks as the performance enhancer (Figure 4g). The temperature sensor consists of silver nanoparticles (AgNPs) embedded in the ZnO:Al (AZO) nanomembrane for improving its sensitivity (Figure 4h). For the strain sensor, co-deposited Cr and SWNTs layers improve the crystallinity of ZnO and passivate intrinsic defects, respectively (Figure 4i). These modifications dramatically amplify the piezoelectric voltage output of the intrinsic ZnO nanomembrane (Figure 4j). For the temperature sensor, $E_C - E_F$ (E_C, minimum energy of the conduction band; E_F, Fermi energy level) is proportional to the concentration of AgNPs inside the ZnO nanomembrane (Figure 4k). The high concentration of AgNPs increases the carrier density and therefore improves the sensitivity of the temperature sensor (Figure 4l). A more in-depth study of functional hybrid nanomaterials would provide new opportunities for high-performance wearable devices.

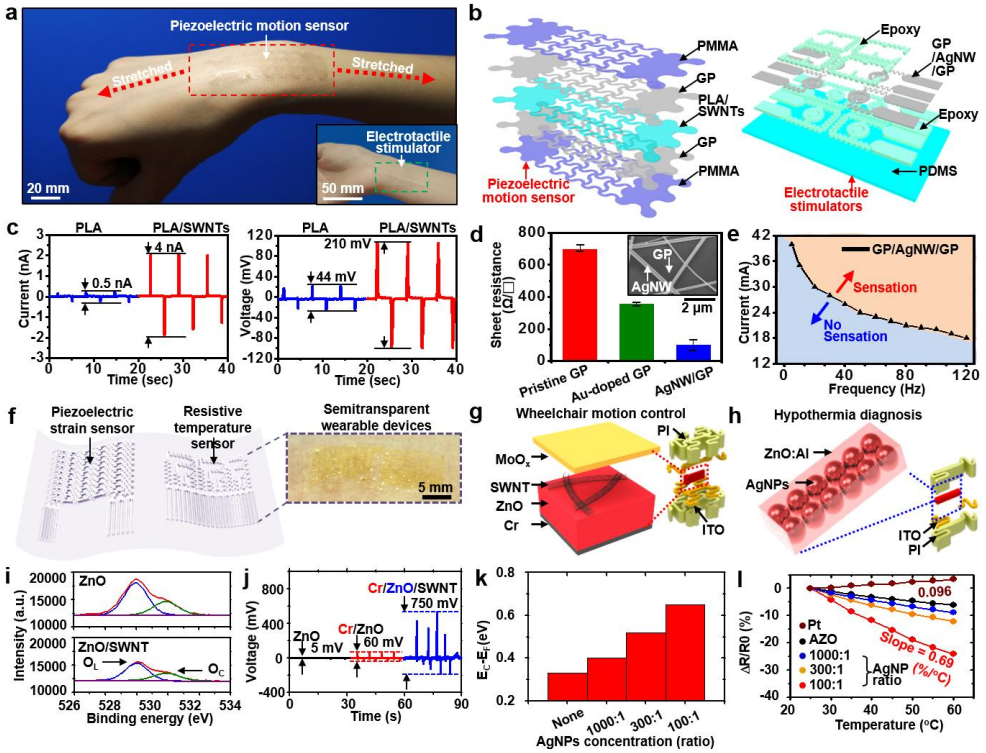

Figure 1.4. Wearable devices with performance-enhancing nanomaterials. a, Photographs showing a transparent wearable motion sensor based on a GP heterostructure and the wearable electrotactile stimulator mounted onto human skin.[1] **b,** Schematic exploded structure of the transparent wearable motion sensor (left) and electrotactile stimulator (right).[1] **c,** Output current (left) and voltage (right) of the wearable motion sensor consisting of PLA (blue) and PLA/SWNTs (red) according to the bending and relaxing motions of the device.[1] **d,** Sheet resistance of pristine GP (red), GP doped with a $AuCl_3$ solution (green), an AgNW/GP composite (blue), and its SEM image (inset).[1] **e,** Minimum required current for the wearer to sense stimulation with respect to the stimulation frequency.[1] **f,** Schematics of a

semitransparent piezoelectric strain sensor, resistive sensor, and photograph of their applied form on skin (inset).[39] **g–h,** Schematics of **g,** the wearable piezoelectric strain sensor and **h,** resistive temperature sensor.[39] **i,** X-ray photoelectron spectroscopy results obtained from a ZnO nanomembrane (top) and ZnO/SWNT composite (bottom).[39] **j,** Output voltage of the piezoelectric strain sensor consisting of ZnO (black), Cr/ZnO (red), and Cr/ZnO/SWNT (blue) for repetitive bending and relaxing of the sensor.[39] **k,** $E_C - E_F$ of the AZO nanomembrane with different concentrations of AgNPs.[39] **l**, Relative change in the resistance of various types of temperature sensors with respect to temperature.[39]

1.3. Wearable memories

Data recorded by wearable sensors should be either transferred or stored for the analysis. Usually, the data are stored in memory devices and retrieved when needed. In this section, two types of ultrathin deformable nonvolatile memory devices—charge-trap floating-gate memory (CTFM)[41] and resistive random access memory (RRAM)[34]—are described.

1.3.1. Deformable charge-trap floating-gate memory

Since the concept of memory devices using floating gates was first proposed,[58] field-effect transistor (FET)-based CTFM has established itself as a dominant data storage device owing to its small area and compatibility with the complementary metal–oxide–semiconductor (CMOS) process.[59, 60] For the realization of deformable CTFMs as next-generation devices, the rigid active materials are replaced with deformable ones such as organic materials,[61, 62] SWNTs,[41] and 2D nanomembranes.[63] Figures 5a and b show the device structure of an SWNT-based CTFM and its laminated form on the human skin, respectively. The Au nanomembrane as a floating gate maximizes the charge capturing functionality (Figure 5c). Soft active layers of SWNT networks are located at the neutral mechanical plane and allow stable operation under deformation.

The floating gate of a continuous metal film has a critical limitation for the retention time.[64] Instead, metal nanoparticles (NPs) are a

promising candidate as the floating gate to realize a fast program/erase speed and long retention time.[64] Figure 5e shows an optical image of a fabricated flexible CTFM using poly(4-vinylphenol) (PVP), pentacene, and gold nanoparticles (AuNPs) as the dielectric, semiconductor, and charge-trap layer, respectively. AuNPs are electrostatically adsorbed onto the PVP blocking oxide, thereby forming a monolayer of AuNPs (Figure 5f). A large on/off window (>10 V) is obtained owing to the high density of AuNPs (Figure 5g). Repetitive bending up to 1,000 cycles with a bending radius of 20 mm does not diminish the performance of the CTFM.

In continuing efforts to develop wearable devices and stretchable electronics, new advances in a wearable high-density nonvolatile memory array integrated with stretchable silicon electronics have been reported.[65] For decades, silicon-based flash memory has been the dominant nonvolatile data storage device owing to the silicon's superb electrical properties. With the rapid development of wearable electronics, many attempts have been made to realize such flash memory on deformable platforms by using organic semiconductors as mentioned above. However, the memory density, multiplexing capability, stretchability, reliability/performance, and charge confinement capability remain limited. Therefore, new advances in stretchable memory technology using single crystal silicon are needed urgently. Chapter 3 describes a wearable multiplexed array of silicon nonvolatile memory that incorporates closely packed AuNP layer as a floating gate for facilitating nanoscale charge confinement.

1.3.2. Nanoparticle-embedded wearable RRAM

RRAM is another promising candidate for future nonvolatile memory devices.[66-68] By integrating RRAM with wearable sensors, a low power consumption and mechanical deformability are important for long-term use in mobile environments.[34] Figure 5i shows wearable RRAM consisting of AuNP charge-trap layers that reduce its operation current. Serpentine interconnections make the wearable RRAM stretchable up to 25% strain (Figures 5j–l). AuNPs embedded between TiO_2 nanomembranes by Langmuir–Blodgett assembly form a uniform layer over a large area (Figures 5m–o). The operation current of the wearable RRAM with one AuNP layer is decreased by one order of magnitude compared to that without AuNPs (Figure 5p). Three layers of AuNPs exhibit a larger current decrease (by almost a factor of three).

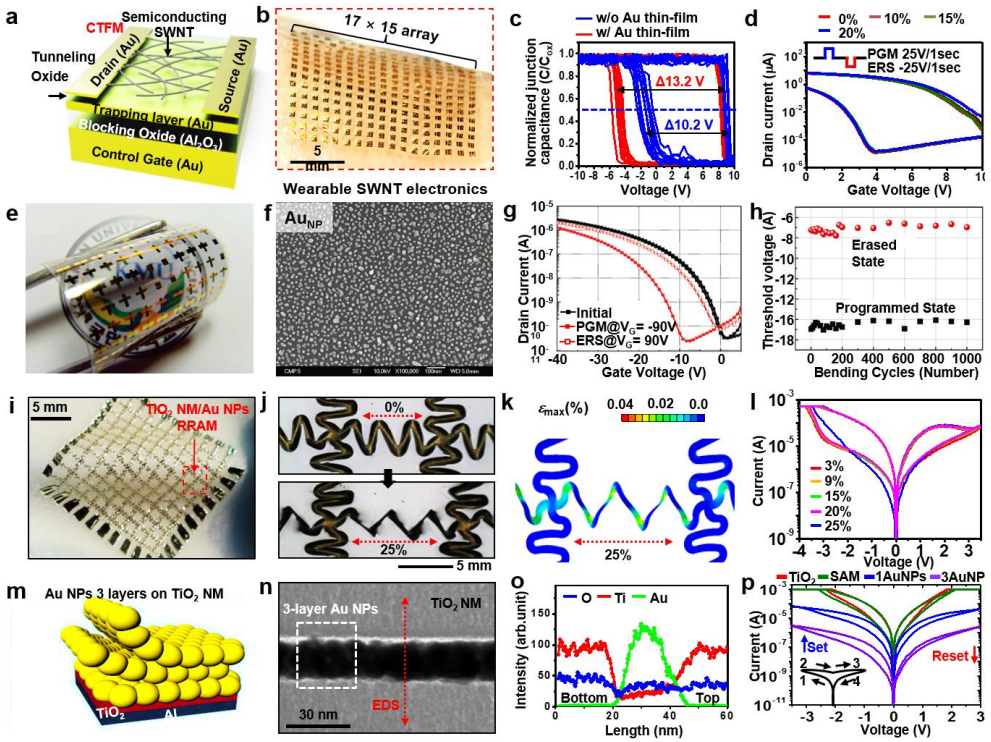

Figure 1.5. Nanomaterial-embedded wearable memory devices. a, Schematic of CTFM.[41] **b,** Photograph of the CTFM array conformally attached to human skin.[41] **c,** C–V hysteresis curves of a CNT-based memory capacitor with (red) and without(blue) a Au thin-film floating gate.[41] **d,** Transfer curves of stretched (0–20%) CTFM for the program and erase modes.[41] **e,** Photograph of a flexible organic memory device with an AuNP floating gate.[62] **f,** SEM image of AuNPs attached to the blocking oxide.[62] **g,** Transfer curves of the flexible organic memory device for the initial, programmed, and erased states.[62] **h,** Threshold voltage of the flexible organic memory device for the programmed and erased states according to the number of bending cycles.[62] **i,** Photograph showing wearable RRAM

attached to a medical bandage.[34] **j,** Optical images of wearable RRAM in the initial (top) and stretched (bottom) states.[34] **k,** Finite-element-analysis results showing the strain distribution of stretched (25%) wearable RRAM.[34] **l,** I–V characteristic curves of wearable RRAM for different stretched states.[34] **m,** Schematic structural view of three layers of AuNPs assembled on a TiO_2 nanomembrane,[34] **n,** TEM image showing three layers of AuNPs embedded between TiO_2 nanomembranes.[34] **o,** Energy-dispersive X-ray spectroscopy results showing the quantitative material composition scanned along the red arrow in Figure 5n.[34] **p,** I–V characteristic curves showing the bipolar switching of wearable RRAM for different trap materials.[34]

1.4. Wearable displays

To construct user-interactive wearable electronic systems, deformable displays that visualize measured or stored data are indispensable for users. Recently, several breakthroughs in deformable light-emitting diode (LED) technologies, including deformable inorganic/organic LEDs,[43, 69-72] polymer LEDs,[73-75] and quantum-dot (QD) LEDs (QLEDs),[76, 77] have been reported.

Figures 6a–c show an image of a deformable actively multiplexed organic LED array, the device structure, and the bending capability, respectively. However, organic light-emitting materials have a low stability in air and a low photostability, and thus they need thick encapsulation under ambient conditions. QDs, on the other hand, have favorable properties such as a good stability in air, good photostability, printability on various substrates, and a high brightness at low operating voltages, which are important key factors for deformable/wearable displays.[78, 79] Figures 6d and e show the structure of recently reported wearable QLED devices.[37] Thanks to ultrathin active and encapsulation layers, the total thickness of the device is ~2.6 μm, enabling conformal contact with the wearer's skin. The wearable QLED is turned on at a low voltage (2 V; Figure 6j) and endures 20% stretching up to 1,000 cycles without any degradation in its brightness (Figure 6g).

Although extensive research efforts have been devoted to the development of ultra-thin light-emitting devices for wearable optoelectronic

applications, significant challenges remain. For example, most deformable light-emitting devices reported to date have focused on showing their light-emitting capabilities from a single device, rather than considering their practical functionality on the human body and degree of integration with wearable electronics. The original purpose of the wearable display is information visualization using co-integrated wearable electronics. Chapter 4 describes ultra-thin skin-like quantum dot (QD) light-emitting diode (QLED) display that can freely visualize various patterns against wearers' skin.

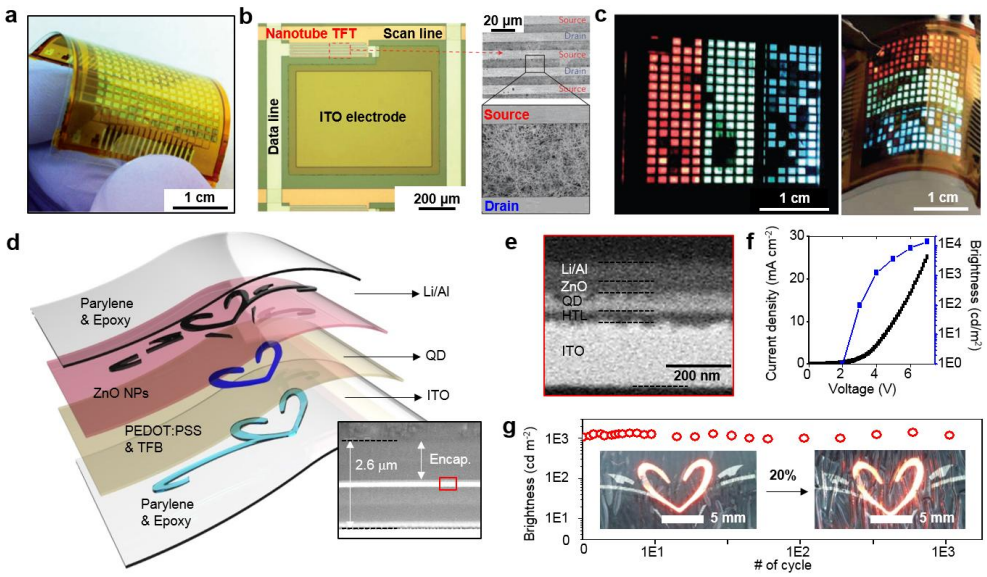

Figure 1.6. Deformable displays. a, Photograph of a fabricated flexible OLED display containing 16×16 pixels.[42] **b,** Optical image of one pixel of the flexible OLED (left) and an enlarged view of the multiplexing CNT FET (right).[42] **c,** Full-color flexible OLED display in which all pixels are turned on (left) and its bent form (right).[42] **d,** Schematic exploded view showing the device structure of a wearable QLED and an SEM image showing the cross section of the display.[37] **e,** TEM image of the active layer indicated by the red box in the inset of Figure 6d.[37] **f,** J–V–L characteristic curves of the wearable QLED.[37] **g,** Stable brightness of the wearable QLED during repetitive stretching cycles. Insets show the initial and stretched states of the wearable QLED.[37]

1.5. Conclusion

The mechanical, electrical, and optical properties of bulk materials change as their size is reduced and/or nanoscale structure engineering is introduced. By using the unique properties of such nanomaterials or their hybrids, many breakthroughs in wearable devices have been accomplished. In this chapter, we reviewed the current status of wearable devices including sensors/actuators, memory devices, and displays. we particularly focused on the wearable devices composed of functional nanomaterials which is utilized to enhance the deformability and performance of the devices. The following chapters will deal with recent research achievements in developing skin-like sensors, memories, and displays for pursuing an integrated wearable system.

References

1. Lim, S., Son, D., Kim, J., Lee, Y. B., Song, J. K., Choi, S., Lee, D. J., Kim, J. H., Lee, M., Hyeon, T., Kim, D. H. Transparent and stretchable interactive human machine interface based on patterned graphene heterostructures. *Adv. Funct. Mater.* **25**, 375-383 (2015).
2. Kim, J., Lee, M., Rhim, J., Wang, P., Lu, N., Kim, D.-H. Next-generation flexible neural and cardiac electrode arrays. *Biomed. Eng. Lett.* **4**, 95-108 (2014).
3. Kim, D. H., Ahn, J. H., Choi, W. M., Kim, H. S., Kim, T. H., Song, J. Z., Huang, Y. G. Y., Liu, Z. J., Lu, C., Rogers, J. A. Stretchable and foldable silicon integrated circuits. *Science* **320**, 507-511 (2008).
4. Kim, D. H., Ghaffari, R., Lu, N. S., Rogers, J. A. Flexible and stretchable electronics for biointegrated devices. *Annu. Rev. Biomed. Eng., Vol 14* **14**, 113-128 (2012).
5. Kim, D. H., Lu, N. S., Ghaffari, R., Rogers, J. A. Inorganic semiconductor nanomaterials for flexible and stretchable bio-integrated electronics. *NPG Asia Mater.* **4**, e15 (2012).
6. Kim, D. H., Xiao, J. L., Song, J. Z., Huang, Y. G., Rogers, J. A. Stretchable, curvilinear electronics based on inorganic materials. *Adv. Mater.* **22**, 2108-2124 (2010).
7. Kim, J., Lee, M., Shim, H. J., Ghaffari, R., Cho, H. R., Son, D., Jung, Y. H., Soh, M., Choi, C., Jung, S., Chu, K., Jeon, D., Lee, S. T., Kim, J. H., Choi, S. H., Hyeon, T., Kim, D. H.

Stretchable silicon nanoribbon electronics for skin prosthesis. *Nat. Commun.* **5**, 5747 (2014).

8. Ying, M., Bonifas, A. P., Lu, N. S., Su, Y. W., Li, R., Cheng, H. Y., Ameen, A., Huang, Y. G., Rogers, J. A. Silicon nanomembranes for fingertip electronics. *Nanotechnology* **23**, 344004 (2012).
9. Kim, D. H., Lu, N. S., Huang, Y. G., Rogers, J. A. Materials for stretchable electronics in bioinspired and biointegrated devices. *MRS Bull.* **37**, 226-235 (2012).
10. Viventi, J., Kim, D. H., Vigeland, L., Frechette, E. S., Blanco, J. A., Kim, Y. S., Avrin, A. E., Tiruvadi, V. R., Hwang, S. W., Vanleer, A. C., Wulsin, D. F., Davis, K., Gelber, C. E., Palmer, L., Van Der Spiegel, J., Wu, J., Xiao, J. L., Huang, Y. G., Contreras, D., Rogers, J. A., Litt, B. Flexible, foldable, actively multiplexed, high-density electrode array for mapping brain activity in vivo. *Nat. Neurosci.* **14**, 1599-1605 (2011).
11. Kim, D.-H., Choi, W. M., Ahn, J.-H., Kim, H.-S., Song, J., Huang, Y., Liu, Z., Lu, C., Koh, C. G., Rogers, J. A. Complementary metal oxide silicon integrated circuits incorporating monolithically integrated stretchable wavy interconnects. *Appl. Phys. Lett.* **93**, 044102 (2008).
12. Hata, K., Futaba, D. N., Mizuno, K., Namai, T., Yumura, M., Iijima, S. Water-assisted highly efficient synthesis of impurity-free single-waited carbon nanotubes. *Science* **306**, 1362-1364 (2004).
13. Yamada, T., Hayamizu, Y., Yamamoto, Y., Yomogida, Y., Izadi-Najafabadi, A., Futaba, D. N., Hata, K. A stretchable carbon

nanotube strain sensor for human-motion detection. *Nat. Nanotech.* **6**, 296-301 (2011).

14. Roh, E., Hwang, B. U., Kim, D., Kim, B. Y., Lee, N. E. Stretchable, transparent, ultrasensitive, and patchable strain sensor for human-machine interfaces comprising a nanohybrid of carbon nanotubes and conductive elastomers. *ACS Nano* **9**, 6252-6261 (2015).
15. Yang, X. W., Cheng, C., Wang, Y. F., Qiu, L., Li, D. Liquid-mediated dense integration of graphene materials for compact capacitive energy storage. *Science* **341**, 534-537 (2013).
16. Lee, S. M., Kim, J. H., Ahn, J. H. Graphene as a flexible electronic material: mechanical limitations by defect formation and efforts to overcome. *Mater. Today* **18**, 336-344 (2015).
17. Jang, H., Lee, W., Won, S. M., Ryu, S. Y., Lee, D., Koo, J. B., Ahn, S. D., Yang, C. W., Jo, M. H., Cho, J. H., Rogers, J. A., Ahn, J. H. Quantum confinement effects in transferrable silicon nanomembranes and their applications on unusual substrates. *Nano Lett.* **13**, 5600-5607 (2013).
18. Kim, D. H., Ahn, J. H., Kim, H. S., Lee, K. J., Kim, T. H., Yu, C. J., Nuzzo, R. G., Rogers, J. A. Complementary logic gates and ring oscillators on plastic substrates by use of printed ribbons of single-crystalline silicon. *IEEE Electron Device Lett.* **29**, 73-76 (2008).
19. Durkop, T., Getty, S. A., Cobas, E., Fuhrer, M. S. Extraordinary mobility in semiconducting carbon nanotubes. *Nano Lett.* **4**, 35-39 (2004).

20. Bolotin, K. I., Sikes, K. J., Jiang, Z., Klima, M., Fudenberg, G., Hone, J., Kim, P., Stormer, H. L. Ultrahigh electron mobility in suspended graphene. *Solid State Commun* **146**, 351-355 (2008).

21. Artukovic, E., Kaempgen, M., Hecht, D. S., Roth, S., Gruner, G. Transparent and flexible carbon nanotube transistors. *Nano Lett.* **5**, 757-760 (2005).

22. Hu, L. B., Yuan, W., Brochu, P., Gruner, G., Pei, Q. B. Highly stretchable, conductive, and transparent nanotube thin films. *Appl. Phys. Lett.* **94**, 044102 (2009).

23. Nair, R. R., Blake, P., Grigorenko, A. N., Novoselov, K. S., Booth, T. J., Stauber, T., Peres, N. M. R., Geim, A. K. Fine structure constant defines visual transparency of graphene. *Science* **320**, 1308-1308 (2008).

24. De Volder, M. F. L., Tawfick, S. H., Baughman, R. H., Hart, A. J. Carbon nanotubes: present and future commercial applications. *Science* **339**, 535-539 (2013).

25. Huang, X., Tan, C. L., Yin, Z. Y., Zhang, H. 25th anniversary article: hybrid nanostructures based on two-dimensional nanomaterials. *Adv. Mater.* **26**, 2185-2204 (2014).

26. Yan, Z., Ma, L. L., Zhu, Y., Lahiri, I., Hahm, M. G., Liu, Z., Yang, S. B., Xiang, C. S., Lu, W., Peng, Z. W., Sun, Z. Z., Kittrell, C., Lou, J., Choi, W. B., Ajayan, P. M., Tour, J. M. Three-dimensional metal-graphene-nanotube multifunctional hybrid materials. *ACS Nano* **7**, 58-64 (2013).

27. Singh, L. P., Srivastava, K., Mishra, R., Ningthoujam, R. S. Multifunctional hybrid nanomaterials from water dispersible

$CaF_2:Eu^{3+}$, Mn^{2+} and Fe_3O_4 for luminescence and hyperthermia application. *J. Phys. Chem. C* **118**, 18087-18096 (2014).

28. Strassert, C. A., Otter, M., Albuquerque, R. Q., Hone, A., Vida, Y., Maier, B., De Cola, L. Photoactive hybrid nanomaterial for targeting, labeling, and killing antibiotic-resistant bacteria. *Angew. Chem. Int. Edit.* **48**, 7928-7931 (2009).

29. Fahmi, A., Pietsch, T., Mendoza, C., Cheval, N. Functional hybrid materials. *Mater. Today* **12**, 44-50 (2009).

30. Zeng, S. W., Baillargeat, D., Ho, H. P., Yong, K. T. Nanomaterials enhanced surface plasmon resonance for biological and chemical sensing applications. *Chem. Soc. Rev.* **43**, 3426-3452 (2014).

31. Buzea, C., Pacheco, I. I., Robbie, K. Nanomaterials and nanoparticles: Sources and toxicity. *Biointerphases* **2**, MR17-71 (2007).

32. Park, T. J., Papaefthymiou, G. C., Viescas, A. J., Moodenbaugh, A., Wong, S. S. Size-dependent magnetic properties of single-crystalline multiferroic $BiFeO_3$ nanoparticles. *Nano Lett.* **7**, 766-772 (2007).

33. Guo, D., Xie, G. X., Luo, J. B. Mechanical properties of nanoparticles: basics and applications. *J. Phys. D Appl. Phys.* **47**, 013001 (2014).

34. Son, D., Lee, J., Qiao, S., Ghaffari, R., Kim, J., Lee, J. E., Song, C., Kim, S. J., Lee, D. J., Jun, S. W., Yang, S., Park, M., Shin, J., Do, K., Lee, M., Kang, K., Hwang, C. S., Lu, N. S., Hyeon, T., Kim, D. H. Multifunctional wearable devices for diagnosis and therapy of movement disorders. *Nat. Nanotech.* **9**, 397-404 (2014).

35. Choi, S., Park, J., Hyun, W., Kim, J., Kim, J., Lee, Y. B., Song, C., Hwang, H. J., Kim, J. H., Hyeon, T., Kim, D. H. Stretchable heater using ligand-exchanged silver nanowire nanocomposite for wearable articular thermotherapy. *ACS Nano* **9**, 6626-6633 (2015).

36. Choi, M. K., Park, O. K., Choi, C., Qiao, S., Ghaffari, R., Kim, J., Lee, D. J., Kim, M., Hyun, W., Kim, S. J., Hwang, H. J., Kwon, S.-H., Hyeon, T., Lu, N., Kim, D.-H. Cephalopod-inspired miniaturized suction cups for smart medical skin. *Adv. Healthc. Mater.* 80-87 (2015).

37. Choi, M. K., Yang, J., Kang, K., Kim, D. C., Choi, C., Park, C., Kim, S. J., Chae, S. I., Kim, T. H., Kim, J. H., Hyeon, T., Kim, D. H. Wearable red-green-blue quantum dot light-emitting diode array using high-resolution intaglio transfer printing. *Nat. Commun.* **6**, 7149 (2015).

38. Jung, S., Lee, J., Hyeon, T., Lee, M., Kim, D. H. Fabric-based integrated energy devices for wearable activity monitors. *Adv. Mater.* **26**, 6329-6334 (2014).

39. Park, M., Do, K., Kim, J., Son, D., Koo, J. H., Park, J., Song, J.-K., Kim, J. H., Lee, M., Hyeon, T., Kim, D.-H. Oxide nanomembrane hybrids with enhanced mechano- and thermo-sensitivity for semitransparent epidermal electronics. *Adv. Healthc. Mater.* **4**, 992-997 (2015).

40. Jung, S., Kim, J. H., Kim, J., Choi, S., Lee, J., Park, I., Hyeon, T., Kim, D. H. Reverse-micelle-induced porous pressure-sensitive rubber for wearable human-machine interfaces. *Adv. Mater.* **26**, 4825-4830 (2014).

41. Son, D., Koo, J. H., Song, J. K., Kim, J., Lee, M., Shim, H. J., Park, M., Lee, M., Kim, J. H., Kim, D. H. Stretchable carbon nanotube charge-trap floating-gate memory and logic devices for wearable electronics. *ACS Nano* **9**, 5585-5593 (2015).

42. Wang, C., Hwang, D., Yu, Z. B., Takei, K., Park, J., Chen, T., Ma, B. W., Javey, A. User-interactive electronic skin for instantaneous pressure visualization. *Nat. Mater.* **12**, 899-904 (2013).

43. Sekitani, T., Nakajima, H., Maeda, H., Fukushima, T., Aida, T., Hata, K., Someya, T. Stretchable active-matrix organic light-emitting diode display using printable elastic conductors. *Nat. Mater.* **8**, 494-499 (2009).

44. Warner, J. H., Young, N. P., Kirkland, A. I., Briggs, G. a. D. Resolving strain in carbon nanotubes at the atomic level. *Nat. Mater.* **10**, 958-962 (2011).

45. Urban, K. W. Electron microscopy: The challenges of graphene. *Nat. Mater.* **10**, 165-166 (2011).

46. Patel, S., Park, H., Bonato, P., Chan, L., Rodgers, M. A review of wearable sensors and systems with application in rehabilitation. *J. Neuroeng. Rehabil.* **9**, (2012).

47. Ponce, B. A., Menendez, M. E., Oladeji, L. O., Fryberger, C. T., Dantuluri, P. K. Emerging technology in surgical education: combining real-time augmented reality and wearable computing devices. *Orthopedics* **37**, 751-757 (2014).

48. Gao, L., Zhang, Y. H., Malyarchuk, V., Jia, L., Jang, K. I., Webb, R. C., Fu, H. R., Shi, Y., Zhou, G. Y., Shi, L. K., Shah, D., Huang, X., Xu, B. X., Yu, C. J., Huang, Y. G., Rogers, J.

A. Epidermal photonic devices for quantitative imaging of temperature and thermal transport characteristics of the skin. *Nat. Commun.* **5**, 4938 (2014).

49. Webb, R. C., Bonifas, A. P., Behnaz, A., Zhang, Y. H., Yu, K. J., Cheng, H. Y., Shi, M. X., Bian, Z. G., Liu, Z. J., Kim, Y. S., Yeo, W. H., Park, J. S., Song, J. Z., Li, Y. H., Huang, Y. G., Gorbach, A. M., Rogers, J. A. Ultrathin conformal devices for precise and continuous thermal characterization of human skin. *Nat. Mater.* **12**, 938-944 (2013).

50. Yeo, W. H., Kim, Y. S., Lee, J., Ameen, A., Shi, L. K., Li, M., Wang, S. D., Ma, R., Jin, S. H., Kang, Z., Huang, Y. G., Rogers, J. A. Multifunctional epidermal electronics printed directly onto the skin. *Adv. Mater.* **25**, 2773-2778 (2013).

51. Jeong, J. W., Kim, M. K., Cheng, H. Y., Yeo, W. H., Huang, X., Liu, Y. H., Zhang, Y. H., Huang, Y. G., Rogers, J. A. Capacitive epidermal electronics for electrically safe, long-term electrophysiological measurements. *Adv. Healthc. Mater.* **3**, 642-648 (2014).

52. Kim, D. H., Lu, N. S., Ma, R., Kim, Y. S., Kim, R. H., Wang, S. D., Wu, J., Won, S. M., Tao, H., Islam, A., Yu, K. J., Kim, T. I., Chowdhury, R., Ying, M., Xu, L. Z., Li, M., Chung, H. J., Keum, H., Mccormick, M., Liu, P., Zhang, Y. W., Omenetto, F. G., Huang, Y. G., Coleman, T., Rogers, J. A. Epidermal electronics. *Science* **333**, 838-843 (2011).

53. Jeong, J. W., Yeo, W. H., Akhtar, A., Norton, J. J. S., Kwack, Y. J., Li, S., Jung, S. Y., Su, Y. W., Lee, W., Xia, J., Cheng, H. Y., Huang, Y. G., Choi, W. S., Bretl, T., Rogers, J. A.

Materials and optimized designs for human-machine interfaces via epidermal electronics. *Adv. Mater.* **25**, 6839-6846 (2013).

54. Viventi, J., Kim, D. H., Moss, J. D., Kim, Y. S., Blanco, J. A., Annetta, N., Hicks, A., Xiao, J. L., Huang, Y. G., Callans, D. J., Rogers, J. A., Litt, B. A Conformal, bio-interfaced class of silicon electronics for mapping cardiac electrophysiology. *Sci. Transl. Med.* **2**, 24ra22 (2010).

55. Moniruzzaman, M., Winey, K. I. Polymer nanocomposites containing carbon nanotubes. *Macromolecules* **39**, 5194-5205 (2006).

56. Fiedler, B., Gojny, F. H., Wichmann, M. H. G., Nolte, M. C. M., Schulte, K. Fundamental aspects of nano-reinforced composites. *Composites Sci. Technol.* **66**, 3115-3125 (2006).

57. Sharma, B. K., Jang, B., Lee, J. E., Bae, S. H., Kim, T. W., Lee, H. J., Kim, J. H., Ahn, J. H. Load-controlled roll transfer of oxide transistors for stretchable electronics. *Adv. Funct. Mater.* **23**, 2024-2032 (2013).

58. Kahng, D., Sze, S. M. A Floating gate and its application to memory devices. *Bcll Syst. Tech. J.* **46**, 1288-1295 (1967).

59. Meena, J. S., Sze, S. M., Chand, U., Tseng, T. Y. Overview of emerging nonvolatile memory technologies. *Nanoscale Res. Lett.* **9**, 526 (2014).

60. Bez, R., Camerlenghi, E., Modelli, A., Visconti, A. Introduction to flash memory. *Proc. IEEE* **91**, 489-502 (2003).

61. Sekitani, T., Yokota, T., Zschieschang, U., Klauk, H., Bauer, S., Takeuchi, K., Takamiya, M., Sakurai, T., Someya, T. Organic

nonvolatile memory transistors for flexible sensor arrays. *Science* **326**, 1516-1519 (2009).

62. Kim, S.-J., Lee, J.-S. Flexible organic transistor memory devices. *Nano Lett.* **10**, 2884-2890 (2010).

63. Kim, S. M., Song, E. B., Lee, S., Zhu, J. F., Seo, D. H., Mecklenburg, M., Seo, S., Wang, K. L. Transparent and flexible graphene charge-trap memory. *ACS Nano* **6**, 7879-7884 (2012).

64. Lee, J.-S. Recent progress in gold nanoparticle-based non-volatile memory devices. *Gold Bull.* **43**, 189-199 (2010).

65. Kim, J., Son, D., Lee, M., Song, C., Song, J. K., Koo, J. H., Lee, D. J., Shim, H. J., Kim, J. H., Lee, M., Hyeon, T., Kim, D. H. A wearable multiplexed silicon nonvolatile memory array using nanocrystal charge confinement. *Sci. Adv.* **2**, e1501101 (2016).

66. Waser, R., Aono, M. Nanoionics-based resistive switching memories. *Nat. Mater.* **6**, 833-840 (2007).

67. Kwon, D. H., Kim, K. M., Jang, J. H., Jeon, J. M., Lee, M. H., Kim, G. H., Li, X. S., Park, G. S., Lee, B., Han, S., Kim, M., Hwang, C. S. Atomic structure of conducting nanofilaments in TiO2 resistive switching memory. *Nat. Nanotech.* **5**, 148-153 (2010).

68. Borghetti, J., Snider, G. S., Kuekes, P. J., Yang, J. J., Stewart, D. R., Williams, R. S. 'Memristive' switches enable 'stateful' logic operations via material implication. *Nature* **464**, 873-876 (2010).

69. Kim, R. H., Kim, D. H., Xiao, J. L., Kim, B. H., Park, S. I., Panilaitis, B., Ghaffari, R., Yao, J. M., Li, M., Liu, Z. J., Malyarchuk, V., Kim, D. G., Le, A. P., Nuzzo, R. G., Kaplan, D. L., Omenetto, F. G., Huang, Y. G., Kang, Z., Rogers, J. A.

Waterproof AlInGaP optoelectronics on stretchable substrates with applications in biomedicine and robotics. *Nat. Mater.* **9**, 929-937 (2010).

70. Kim, T. I., Mccall, J. G., Jung, Y. H., Huang, X., Siuda, E. R., Li, Y. H., Song, J. Z., Song, Y. M., Pao, H. A., Kim, R. H., Lu, C. F., Lee, S. D., Song, I. S., Shin, G., Al-Hasani, R., Kim, S., Tan, M. P., Huang, Y. G., Omenetto, F. G., Rogers, J. A., Bruchas, M. R. Injectable, cellular-scale optoelectronics with applications for wireless optogenetics. *Science* **340**, 211-216 (2013).

71. Park, S. I., Xiong, Y. J., Kim, R. H., Elvikis, P., Meitl, M., Kim, D. H., Wu, J., Yoon, J., Yu, C. J., Liu, Z. J., Huang, Y. G., Hwang, K., Ferreira, P., Li, X. L., Choquette, K., Rogers, J. A. Printed assemblies of inorganic light-emitting diodes for deformable and semitransparent displays. *Science* **325**, 977-981 (2009).

72. Han, T. H., Lee, Y., Choi, M. R., Woo, S. H., Bae, S. H., Hong, B. H., Ahn, J. H., Lee, T. W. Extremely efficient flexible organic light-emitting diodes with modified graphene anode. *Nat. Photon.* **6**, 105-110 (2012).

73. Liang, J. J., Li, L., Niu, X. F., Yu, Z. B., Pei, Q. B. Elastomeric polymer light-emitting devices and displays. *Nat. Photon.* **7**, 817-824 (2013).

74. Yu, Z. B., Niu, X. F., Liu, Z. T., Pei, Q. B. Intrinsically Stretchable polymer light-emitting devices using carbon nanotube-polymer composite electrodes. *Adv. Mater.* **23**, 3989-3994 (2011).

75. White, M. S., Kaltenbrunner, M., Glowacki, E. D., Gutnichenko, K., Kettlgruber, G., Graz, I., Aazou, S., Ulbricht, C., Egbe, D. a. M., Miron, M. C., Major, Z., Scharber, M. C., Sekitani, T., Someya, T., Bauer, S., Sariciftci, N. S. Ultrathin, highly flexible and stretchable PLEDs. *Nat. Photon.* **7**, 811-816 (2013).

76. Kim, T. H., Cho, K. S., Lee, E. K., Lee, S. J., Chae, J., Kim, J. W., Kim, D. H., Kwon, J. Y., Amaratunga, G., Lee, S. Y., Choi, B. L., Kuk, Y., Kim, J. M., Kim, K. Full-colour quantum dot displays fabricated by transfer printing. *Nat. Photon.* **5**, 176-182 (2011).

77. Yang, X. Y., Mutlugun, E., Dang, C., Dev, K., Gao, Y., Tan, S. T., Sun, X. W., Demir, H. V. Highly flexible, electrically driven, top-emitting, quantum dot light-emitting stickers. *ACS Nano* **8**, 8224-8231 (2014).

78. Kwak, J., Bae, W. K., Lee, D., Park, I., Lim, J., Park, M., Cho, H., Woo, H., Yoon, D. Y., Char, K., Lee, S., Lee, C. Bright and efficient full-color colloidal quantum dot light-emitting diodes using an inverted device structure. *Nano Lett.* **12**, 2362-2366 (2012).

79. Dai, X. L., Zhang, Z. X., Jin, Y. Z., Niu, Y., Cao, H. J., Liang, X. Y., Chen, L. W., Wang, J. P., Peng, X. G. Solution-processed, high-performance light-emitting diodes based on quantum dots. *Nature* **515**, 96-99 (2014).

Chapter 2. Stretchable silicon nanoribbon based sensor array for skin prosthesis

2.1 Introduction

Skin-based mechanoreceptors and thermo-receptors gather rich streams of information from the external environment.[1] The central and autonomic nervous systems analyze and transform these sensory inputs into regulated physiological responses and motor outputs[1]. Although there is significant progress in understanding the neural circuits underlying mechanical and thermal sensation,[2] replicating these capabilities in artificial skin and prosthetics remains challenging. As a result, many amputee patients wear prosthetic limbs for cosmetic utility[3] or as supplementary movement aids[4] rather than as a functional replacement for natural limbs. Recent advances in the design of prosthetic limbs integrated with rigid and/or semi-flexible tactile sensors provide sensory reception to enable feedback in response to variable environments.[5] However, there still exists a mechanical mismatch between conventional electronics in wearable prosthetics and soft biological tissues, which impede the utility and performance of prosthetics in amputee populations.

Several efforts are underway to bridge the technological gap between artificial and real skin. Flexible and/or stretchable tactile sensors based on various micro/nano materials and structures have been the focus

of intense study.[6-11] In particular, pressure sensitive rubbers (PSRs) are used as resistive elements that respond to tensile strains,[12-14] which can be integrated with flexible organic electronics[15-18] and nanomaterials-based (nanowires[19] and nanotubes[20]) transistors. However, conventional PSRs have modest response times and undergo significant hysteresis. Single crystalline silicon strain gauges on soft elastomer exhibit a linear relationship between strain and relative resistance changes with fast response times.[21] These sensors have been previously utilized to detect motion across various anatomical locations, such as the wrist[22] and fingers.[23] In addition, stretchable metal and single crystalline silicon temperature sensors[12, 24] fabricated on ultrathin substrates have been applied for temperature monitoring on human skin. However, the heterogeneity in geometry and strain profiles of skin across different anatomies necessitate custom designs for specific body locations. Heterogeneous integration of pressure, temperature, and humidity sensing coupled with electro-resistive thermal actuation in site-specific geometrical layouts would thus provide unique opportunities to dramatically advance the state of the art in smart prosthetics and artificial skin.

Here, we report a stretchable prosthetic skin equipped with ultrathin single crystalline silicon nanoribbon (SiNR) strain, pressure and temperature sensor arrays. The SiNR sensor arrays have geometries that are tuned to stretch according to the dynamic mechanical properties of the target skin segment. This design strategy provides the highest levels of spatio-temporal sensitivity and mechanical reliability, thereby dramatically

enhancing the perception capabilities of artificial skin in response to highly variable external environments. Integration of stretchable humidity sensors and heaters further enables the sensation of skin moisture and body temperature regulation, respectively. Corresponding electrical stimuli can then be transmitted from the prosthetic skin to the body to stimulate specific nerves via conformally-contacted ultrathin stretchable nanowire-based electrodes, which are decorated with ceria nanoparticles for inflammation control.

*** The contents of this chapter were published in *Nature Communications*, 2014, *5*, 5747.**

2.2 Experimental section

Quantitative measurement of skin stretchability during various motions: Motion capture was used to measure stretchability of skin during various movements of hand. For motion tracking of the skin, thirty one reflective markers (diameter: 3 mm) were attached on the left hand, spacing at least 1.5 cm apart to avoid ambiguity of the location data. The locations and angles of the twelve motion capture cameras (OptiTrack Prime 41, NaturalPoint, USA) were adjusted to the optimum points through calibration process using a specially designed calibration wand. The subject wearing reflective markers moved his limb in predetermined way, and the motion capture cameras recorded the position changes of the reflective markers. The recorded data was analyzed with motion tracking software (Motionbuilder, Autodesk, USA) to rebuild the motions and extracted three dimensional coordinates of the reflective markers. Assuming that neighboring markers were placed on the same plane, the degree of skin stretching was measured by calculating the change of distance between nearby markers.

Fabrication of SiNR-based devices: A boron doped (resistivity 8.5~11.5 Ω·cm) 142 nm thick silicon-on-insulator (SOI) wafer (prime grade, Soitec) was prepared. To make ohmic contact with metal interconnection, the SOI wafer pieces were highly doped with spin-on-dopant (SOD) (B153 for boron, P509 for phosphorus, Filmtronics, USA; spin-coated at 3,000 r.p.m.

for 30 s, pre-deposited at 220 ˚C for 5 min and drove-in at 975 ˚C for 3 min 30 s). The highly doped silicon nanomembrane (SiNM) was liberated from the substrate by etching of buried oxide using hydrofluoric acid (~49%, J. T. Baker®, USA). A precursor solution of polyimide (PI) (polyamic acid, Sigma Aldrich, USA) was spin-coated (8,000 r.p.m. for 60 s; ~1.0 μm) on a silicon oxide (SiO_2) wafer (test grade, 4science, Republic of Korea). After partially curing the PI at 110 ˚C for 1 min, SiNM were transferred onto the PI layer by polydimethylsiloxane (PDMS) stamp. After curing of the PI layer at 250 ˚C for 1 hour, serpentine photoresist (S1805, Microchem, USA) masks were defined photolithographycally on the SiNM and exposed silicon was etched using reactive ion etching (RIE; SF_6 plasma, 50 s.c.c.m., chamber pressure of 50 mtorr, 100 W RF power for 25 s), forming isolated SiNRs. Thermal evaporation was used for metallization (gold (Au)/chromium (Cr); 70 nm/7 nm thick), and the serpentine metal lines were defined with photolithography and subsequent wet chemical etching. Then, top PI layer was spin-coated and cured just like a bottom PI layer so that the device layer was encapsulated and placed near the neutral mechanical plane. The entire trilayer (PI/device/PI) was patterned by RIE (O_2 plasma, 100 s.c.c.m., chamber pressure of 100 mtorr, 150 W RF power for 10 min), forming mesh-like structure to make it stretchable. The whole device formed on the SiO_2 wafer was picked up with water-soluble tape (3M, USA) by virtue of poor adhesion between bottom PI layer and SiO_2 substrate, and the device on the tape was transferred onto cured PDMS

film (base:curing agent(w/w) = 40:1, cured at 70 ˚C for 3 hours) spin-coated (3000 r.p.m. for 30 s) on the polyvinyl alcohol (PVA) film. Deionized water was used to dissolve the water-soluble tape to release the device and PDMS was spin-coated (3000 r.p.m. for 30 s) on it for encapsulation. For attachment of device on the substrate on demand (human skin for mapping degree of stretchability or PDMS film for making skin prosthesis), the encapsulated device was picked up with PVA film, attached on the target substrate with the device facing down, and the PVA film was removed by DI water.

Fabrication of Au-based devices: A precursor solution of PI was spin-coated on a SiO_2 wafer. The PI layer was fully cured at 250 ˚C for 1 hour. To form separated electrodes for humidity sensors and resistive conduction paths for heaters, Au/Cr (70 nm/7 nm) layers were deposited by using thermal evaporation process. The deposited metal film was patterned through the photolithography. For the encapsulation, another PI layer was spin-coated and cured using the same procedures and conditions. The whole structure (PI/metal/PI) was patterned as a stretchable form, released from the SiO_2 wafer, and then transferred to the polymeric substrate by using the same process as mentioned above.

Characterization of SiNR strain gauges: Resistance change measurement of SiNR strain gauges was carried out for various serpentine designs under various stretching conditions. The resistance change tendency depending on

the direction of the stretching was also analyzed. The automated bending stage was used to stretch the artificial skin containing strain gauge arrays with sufficient accuracy. The resistance of strain gauges under specific stretching conditions were calculated using applied constant current (4 mA) and measured corresponding voltage using source measurement units (SMU; NI PXIe-4143, National Instruments, USA) controlled by custom made LabVIEW based program (National Instruments, USA). Continuous resistance change monitoring of SiNR strain gauges having different serpentine design, and temperature dependency comparison between a single strain gauge and four strain gauges in Wheatstone bridge configuration were performed with the probe station (MSTECH, Republic of Korea) and parameter analyzer (B1500A, Agilent, USA). The current flowing through each strain gauge under cyclic stretching (0~5%) was measured for 15 s while the constant voltage (0.1 V) was applied. The calculated resistance was simply converted into relative resistance change ($\Delta R/R_0$) by setting up the initial resistance (R_0) as the resistance of undeformed strain gauge.

Characterization of SiNR pressure sensors: Resistance change measurements for SiNR pressure sensors were recorded for representative serpentine designs under various applied pressures. A screw having diameter of 0.5 cm was set on the load cell to press the specific region of the pressure sensor array. The load cell measured the applied load, and corresponding pressure could be calculated by dividing the load with the area. The

resistance change induced by the applied pressure was calculated using the applied constant current (4 mA) and the corresponding voltage measured by the SMU.

Characterization of SiNR temperature sensors: To obtain I-V curves of p-n-diode-based SiNR temperature sensors, electrodes connected to the p-type and n-type region were probed by using the probe station. The increasing voltage was applied to the p-type region while the n-type region was grounded, and the corresponding current was measured by the parameter analyzer. The calibration curves were obtained by deducing the corresponding voltages at the specific current (10 nA) from the I-V curves and plotting them with respect to the temperatures measured by IR temperature sensor.

Temperature mapping using SiNR temperature sensors array: There is an inversely linear relationship between temperature and the resistance of SiNR temperature sensor biased for specific constant current flow. Prior to temperature mapping, the calibration process was performed to relate the surface temperature measured by IR camera (i5, FILR, Sweden) and the resistance of SiNR temperature sensor at specific constant current. Using this relationship, regional temperature information could be obtained by monitoring resistance of regionally distributed SiNR temperature sensors at specific current (500 nA or 5 μA). During the measurement, the SiNR temperature sensors were forward biased by the SMUs and the current

was sequentially applied to the dozens of the temperature sensor by virtue of the multiplexer switch. The resistances of each SiNR temperature sensor were converted to the temperature using the calibration results, the deduced temperature from six neighboring SiNR temperature sensors were averaged, and these values over the all sensing area were interpolated by the MATLAB software to obtain the temperature map.

Characterization of humidity sensors: Relative humidity was controlled by introducing mixed streams of dry nitrogen and deionized water vapor in proper ratio into the test chamber. Relative humidity was measured with a commercial humidity temperature meter (CENTER®310) placed inside the test chamber. The capacitance changes of the fabricated humidity sensor were measured using a digital multimeter (NI PXI-4072, National Instruments, USA) controlled by a custom-made LabVIEW program.

Characterization of heaters: The stretchable heater (Au/Cr, 70nm/7nm, 550 Ω) on a PDMS substrate was connected to the power supply. The thermogram was captured by a commercial IR camera (320×240 pixels; P25, FILR, Sweden). A manual bending stage was used to stretch the stretchable heater to apply designated amount of strain.

Impedance characterization of Au, Pt/Au film, and Pt nanowires (NWs)/Au electrode: Thermally evaporated Au electrode, electrically deposited Pt film on Au electrode, and electo-chemically grown PtNWs on Au electrode

were prepared. Impedance of each electrode was measured using electrochemical workstation with the three-electrode system: a platinum, Ag/AgCl and target electrode as a counter, reference and working electrode, respectively. All electrodes were immersed in the conductive PBS solution, therefore they are electrically connected each other. Using alternating current (AC) impedance mode with the frequency range of 1 to 10^6 Hz, impedance characterization was carried out for ~5 min at the room temperature.

2.3. Results and discussion

2.3.1. Artificial skin with multi-modal sensing capability

Figure 2.1 shows an image of artificial skin with integrated electronics laminated on the surface of a prosthetic hand. The artificial skin surface of the prosthesis is highly compliant (inset), and mechanically couples to the curvilinear surface of the prosthesis. A schematic illustration of the stacked layers (Figure 2.1b) highlights the location of the embedded electronics, sensors and actuators, with magnified views shown in Figure 2.1c-f.

The bottom layer contains electroresistive heaters in filamentary patterns bonded to the PDMS (Dow Corning, USA) substrate. These thermal actuators are in fractal-inspired formats[25] (Figure 2.1f) to facilitate uniform heating during stretching and contraction of the skin layer. To monitor tactile and thermal feedback during actuation, we employ strain (Figure 2.1c), pressure (Figure 2.1d, left) and temperature sensor (Figure 2.1d, right) arrays in the middle layer of the stack. These network of sensors have spatially varying geometrical designs, ranging from linear to serpentine shapes (Figure 2.2, denoted as S1-S6 in ascending order of curvatures), depending on the mechanics of the underlying prosthetics. An array of humidity sensors, consisting of coplanar capacitors (Figure 2.1e) in the top encapsulating layer detects capacitance changes at different humidity levels (Figure 2.1e bottom right, inset shows the magnified view)

to capture information about ambient conditions. Each sensor/actuator layer has distinct interconnections to the external data acquisition instrument (Figure 2.1b). Integration of each stacked layer using via-hole structures can further simplify the wiring requirements. Due to this stacked structure configuration, sensor arrays may mechanically interfere with each other. For instance, strain/pressure sensors positioned beneath humidity sensors could exhibit reduced mechanical responses to external deformations because of the additional stiffness. To address this issue, stacked structures with staggered arrangement of sensors provide a possible solution to minimize interferences.

All of the aforementioned devices have ultrathin regions, *i.e.* SiNRs or metal traces that are passivated by polyimide (PI; Figure 2.1c-f, upper right inset). The one exception is the design of the tactile pressure sensors, which contain a cavity to enhance sensitivity in response to mechanical pressure changes. The key material utilized in the fabrication of these tactile sensors is p-type doped single crystalline SiNRs, which have both high piezoresistivity (gauge factor: ~200)[21] and low fracture toughness (~1.0 MPa $m^{1/2}$).[26] To prevent mechanical failures, we employ mechanical strategies, whereby ultrathin (~110 nm) SiNRs are kept in the neutral mechanical plane of the stack[27]. Figure 2.1g shows a scanning electron microscope (SEM) image of a crack-free SiNR transferred on the silicon oxide substrate. Wrinkles are deliberately induced to highlight the ultrathin nature and mechanical flexibility of the SiNR under mechanical deformation (Figure 2.1h). Figure 2.1i shows a cross-sectional transmission

electron microscope (TEM) image of the SiNR located in the neutral mechanical plane (PI/SiNR/PI structure). These designs help to minimize bending induced strains.[27]

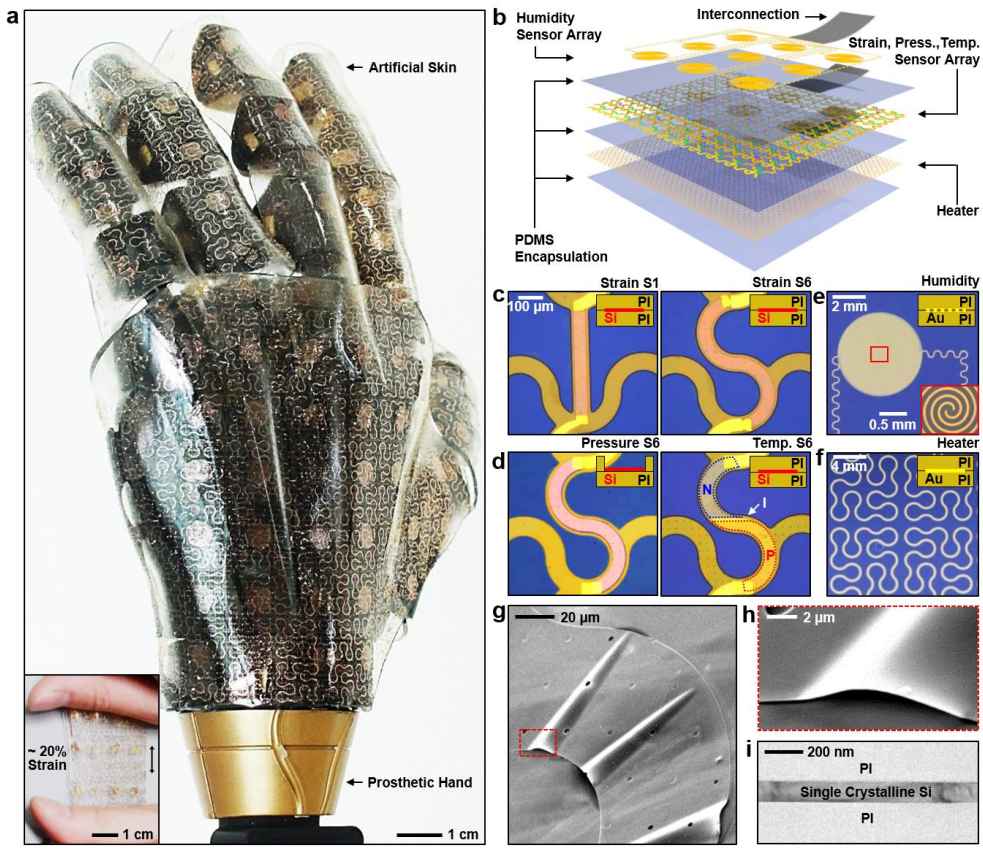

Figure 2.1. Prosthetic skin based on site-specifically designed SiNR electronics. a, Photograph of a representative smart artificial skin with integrated stretchable sensors and actuators covering the entire surface area of a prosthetic hand. The inset shows the artificial skin stretched ~20%. **b,** An exploded view of artificial skin comprised of six stacked layers. Interconnected wires of each layer relay signals to external instruments. **c,** Representative microscopic images of SiNR strain gauge: S1 which has a curvature of 0 mm^{-1} (left); S6 which has a curvature of 10 mm^{-1} (right). S1 and S6 are optimized for the location of minimal stretch (~5%) and large stretch (~30%), respectively. **d,** Representative microscopic images of

SiNR pressure sensor S6 and temperature sensor S6. **e,** Microscopic image of humidity sensor. Bottom right inset shows the magnified view of the central area, showing separate electrodes with identical inter-spiral gap. **f,** Microscopic image of electroresistive heater. **c-f,** The upper right insets of the each figure show that the cross sectional structure of each device. **g,** SEM image of the SiNR transferred on the silicon oxide substrate. The wrinkles are deliberately formed to show the SiNR's high flexibility. **h,** The magnified view of wrinkled SiNR. **i,** A cross-sectional TEM image of the strain gauge, showing that the SiNR encapsulated with PI layers is located at the neutral mechanical plane.

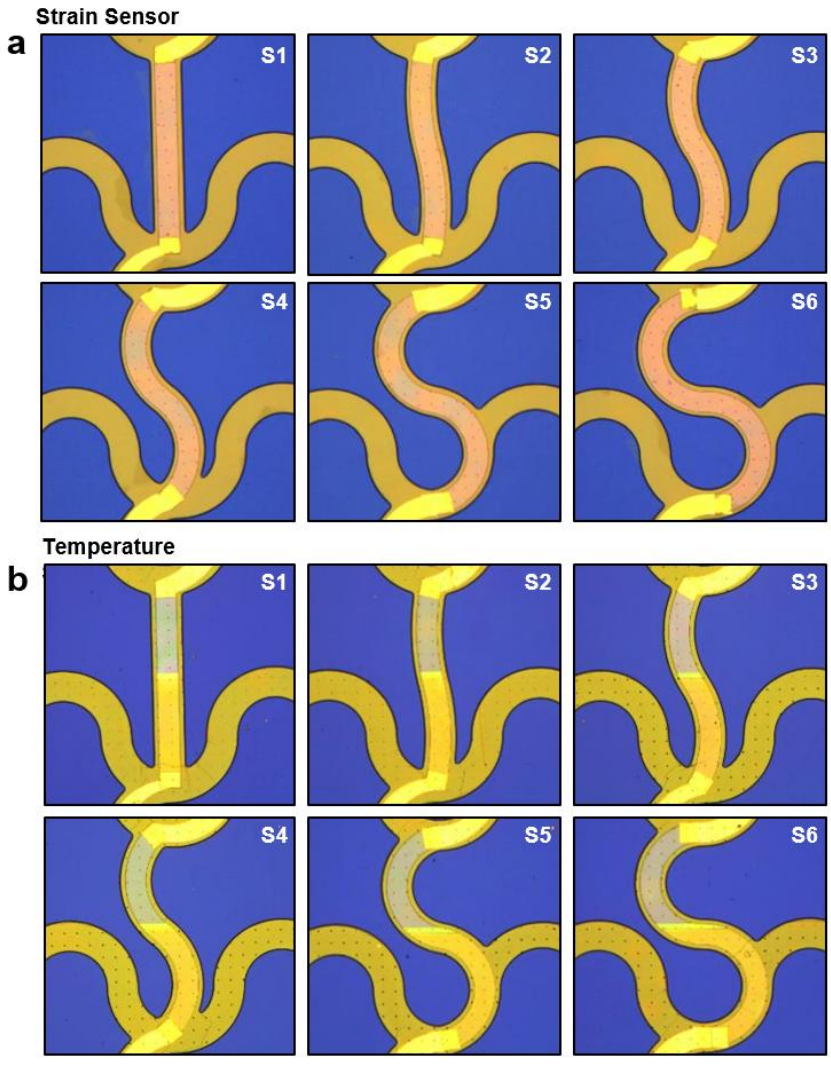

Figure 2.2. Microscope images of the serpentine shaped strain and temperature sensors with various curvatures, κ = 0 (S1), 1.94 (S2), 4.74 (S3), 7.4 (S4), 9.75 (S5), 10 mm^{-1} (S6). a, Linear and serpentine shaped p-type doped SiNRs for strain sensors. **b,** Linear and serpentine shaped SiNRs p-n junction diodes for temperature sensors.

2.3.2. Detection of regional strain of skins in various motions

Skin normally experiences multi-axial forces and undergoes a range of angular and linear motions at different body locations. This heterogeneity in movements and strains of skin suggest the need for location-specific optimization of sensors and actuators in artificial skin and prosthetics. For example, a network of tactile sensors and strain gauges can provide feedback about tensile strains to characterize fatigue or ensuing failure modes in a highly localized manner.

To characterize the mechanical behavior of movements and skin mechanics on the arm and hands, we capture movement and strains from several target points on skin using a motion capture camera system (Figure 2.3a). In total, twelve motion-capture cameras (OptiTrack Prime 41, NaturalPoint, USA) are synchronously used to acquire three-dimensional coordinates of reflective markers affixed to the hand and wrist. Four representative hand movements, including fist clenching as well as vertical (bending) and lateral (tilting) wrist movements are analyzed (Figure 2.3b). Strain distribution is calculated by measuring displacements relative to neighboring reflective markers. During fist clenching, the skin stretches ~5% (Figure 2.3b, upper left), whereas, significantly greater strains (~16%) are induced in response to bending (Figure 2.3b, upper right). Tilting movements induce compression on the wrinkled side of the wrist, while skin experiences stretching on the opposing side of the wrist (Figure 2.3b, bottom).

By gathering these movement data, we map strain profiles near the wrist and hand (Figure 2.3c). For regions where skin hardly stretches, linear SiNR (S1 design) is used to maximize sensitivity. On the other hand, serpentine SiNRs (e.g. S3 or S6 designs) are applied on more stretchy areas, to accommodate for the larger range of strain changes. Furthermore, the curvature SiNRs are optimally designed depending on the stretchability of the underlying anatomy (e.g. low deformation region ~5%: S1 design, medium deformation region ~10%: S3 design, high deformation region ~16%: S6 design, right frames of Figure. 2.3c). These site-specific SiNR sensor arrays are shown in Figure 2.3d. The exploded frames to the right are magnified images of each design. These ultrathin filamentary designs enable conformal integration on human skin with high signal sensitivity and mechanical durability. Detailed step-by-step fabrication procedures are included in Figure 2.4.

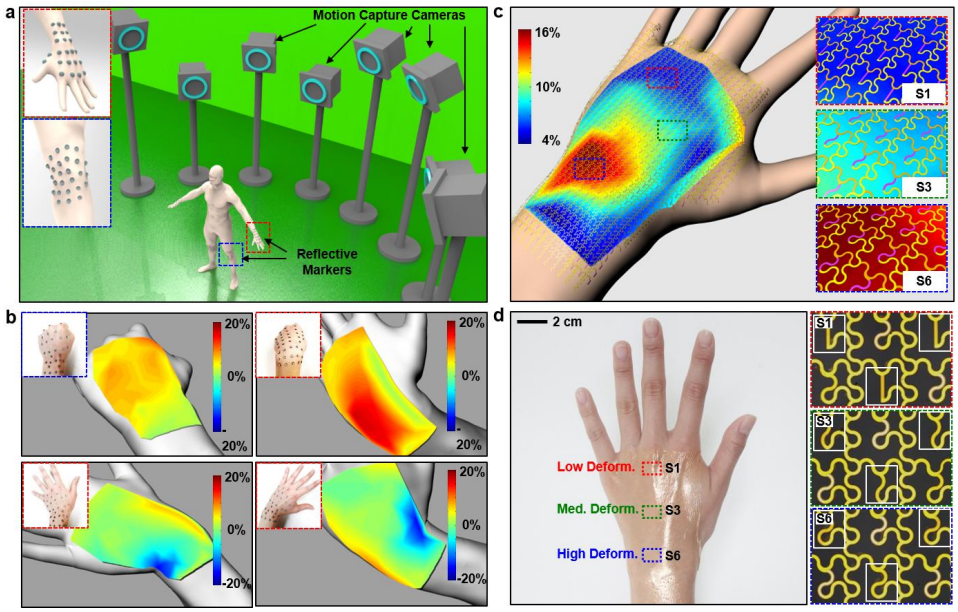

Figure 2.3. Detection of strain distributions of skins in various motions. a, Schematic image of motion capture system. **b**, Regional strain maps of the skin, calculated using positional information acquired by motion capture system for four different motions: clenching fist, front bending, tilting left and right. An upper left inset of each case shows the actual hand with reflective markers. **c,** Map of maximum stretching range for entire area acquired by combining the data from b, and corresponding arrangement of site-specifically designed SiNR strain gauge. The frames on the right show magnified views of each design (S1, S3, and S6 designs; indicated as black box). **d,** Image of the fabricated site-specifically designed SiNR strain gauge arrays conformally attached on the back of hand. The frames on the right show magnified views of each design (indicated as white box). S1, S3, and S6 design for low, medium, and high deformation location, respectively.

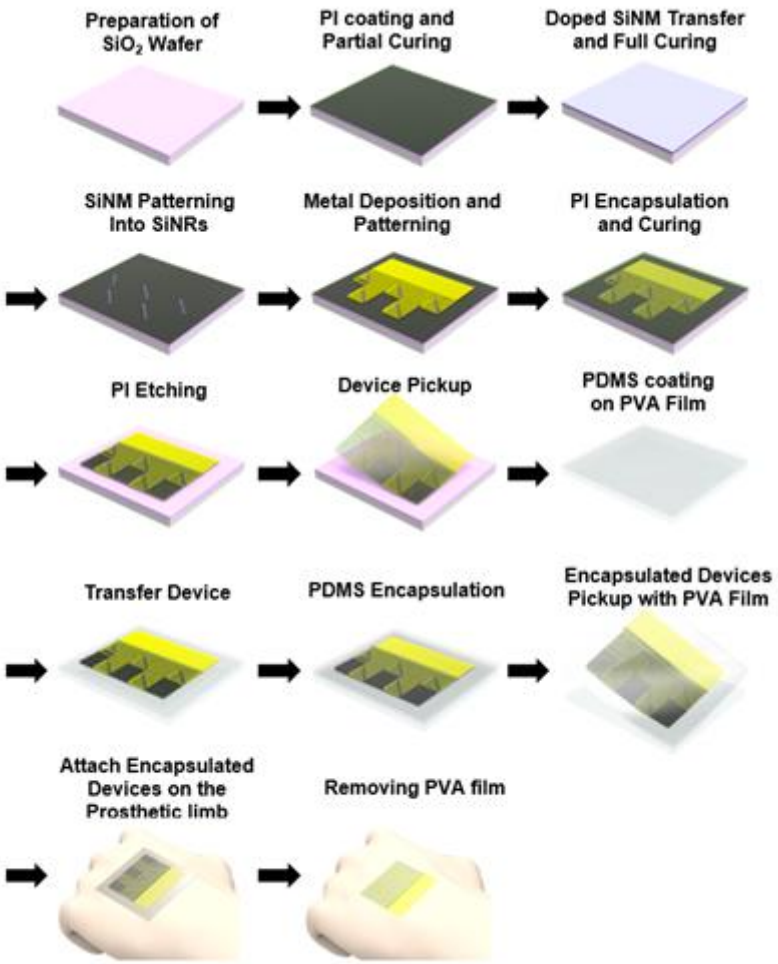

Figure 2.4. Schematic overview of the fabrication process of a SiNR-based sensor array.

2.3.3. SiNR mechanical sensors with site-specific sensitivity

To characterize the effects of strains on different SiNR sensor designs, we examine several serpentine designs (Figure 2.5a) with different curvatures. As applied strains increase, SiNR strain gauges with small curvature experience considerably greater strains compared to those with larger curvatures. The serpentine designs of large curvature help to relieve induced strains more than smaller ones. This effect is captured by measuring relative resistance ($\Delta R/R$) as a function of applied strain (Figure 2.5b). An experimental stretch test setup using a custom-made bending stage is shown in Figure 2.6a.

SiNR sensors of larger curvature can withstand greater applied strains, and thereby have large dynamic range, but exhibit reduced sensitivity (Figure 2.5b). But cyclic stretching tests reveal that sensitivity increases with lower curvatures (Figure 2.7). We examine six unique serpentine designs with curvatures of κ = 0 (S1), 1.94 (S2), 4.74 (S3), 7.4 (S4), 9.75 (S5), and 10 mm^{-1} (S6) for cyclic stretching test. According to this tradeoff effect, SiNR S1 is most appropriate for sites with small range of stretching, whereas SiNR S6 is more suitable for regions experiencing large stretching. The results also indicate that SiNR strain gauges have a linear and fast response time, and no hysteresis irrespective of designs. The SiNR strain gauges are mainly sensitive to the longitudinal stretching (Figure 2.8a and b). Noise in the strain sensors is often caused by shift in external temperature, which affects individual

strain sensor resistance measurements. To reduce effects of noise caused by thermal shifts, a Wheatstone bridge configuration can be applied (Figure 2.8c and d). In the future, it is necessary to incorporate strain gauges in rosette configurations[28] to measure strain distribution in the arbitrary xy coordinate plane to characterize plane strain of prosthetic skin (Figure 2.9).

Site-specific designs for strain gauge arrays that conform to the complex geometry of the human hand (Figure 2.6b) are used to measure its strain distributions. Figure 2.9 shows strain distribution maps (red dotted box regions) in response to four representative hand motions. Signals are collected with a multiplexing measurement unit (Figure 2.6c). For locations where skin deformations are small (*e.g.* back of hand), the S1 designs are used (clenching fist; Figure 2.10a, upper left). Despite small induced strains on the back of hand, the SiNR strain gauge arrays with S1 design successfully map the regional strain distribution. Conversely, SiNR strain gauge arrays with S6 design are used in locations where large skin deformations occur (*e.g.* wrist region), with significant bending (Figure 2.10a, upper right) and tilting (Figure 2.10a, bottom). The SiNR strain gauge arrays measure large induced strains with high fidelity. Even larger induced strains exist near knee joints and can be measured (Figure 2.10b). SiNR strain gauges having large curvatures (*e.g.* S3) endure mechanical deformations in response to cyclic bending of knee joints more than small curvatures (*e.g.* S1).

Figure. 2.11a shows the working principle of a SiNR pressure sensor. By

designing a cavity in the PI passivation layer of SiNRs, the pressure detection sensitivity is enhanced (Figure 2.11a, top versus bottom), as confirmed by FEA. For the FEA, the cross-sections of the SiNR pressure sensors with and without the cavity are modeled using four-node plane-strain elements. The silicon and PI layers are assumed to be bonded perfectly. The pressure boundary conditions (~50 kPa) are applied on the top surface of the PI layer. The cavity-based SiNR pressure sensor shows ~10 times higher sensitivity to applied pressures than the SiNR pressure sensor without the cavity for both S1 and S6 designs (Figure 2.11b). Detailed measurements of sensitivity for S1 and S6 are 0.41% kPa^{-1} (with cavity) versus 0.0315% kPa^{-1} (without cavity) and 0.075% kPa^{-1} (with cavity) versus 0.0073% kPa^{-1} (without cavity), respectively. Serpentine-shaped SiNR pressure sensors (*e.g.* S6) have reduced sensitivity to vertical pressures compared to linear versions (S1). However, the pressure sensitivity of S6 design sensors is comparable to human mechanoreceptors responses, which normally respond to stresses as low as ~87 kPa.[1] Figure 2.11c show pressure response maps from sensor arrays with S6 designs. S6 design sensors are suitable for the relatively more elastic regions where modest tactile sensitivity is required, such as near the wrist.

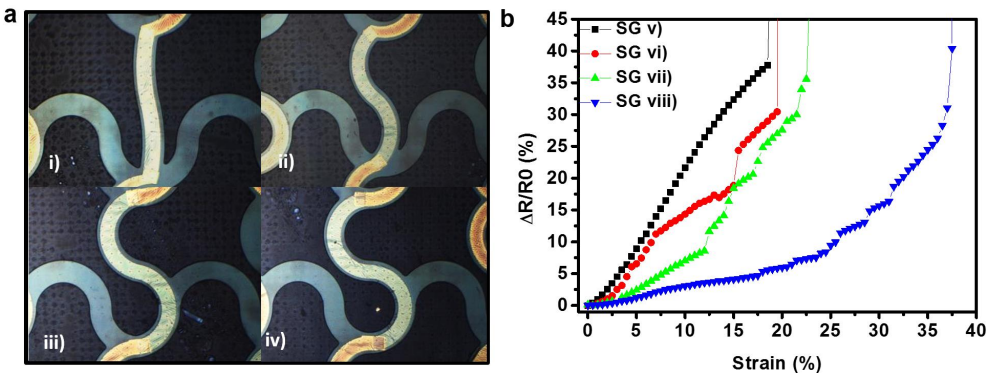

Figure 2.5. SiNR strain gauges of different sensitivities and detection ranges. a, Images of SiNR strain gauges of different curvature. **b,** Resistance changes for different curvatures of SiNR, depending on applied strain.

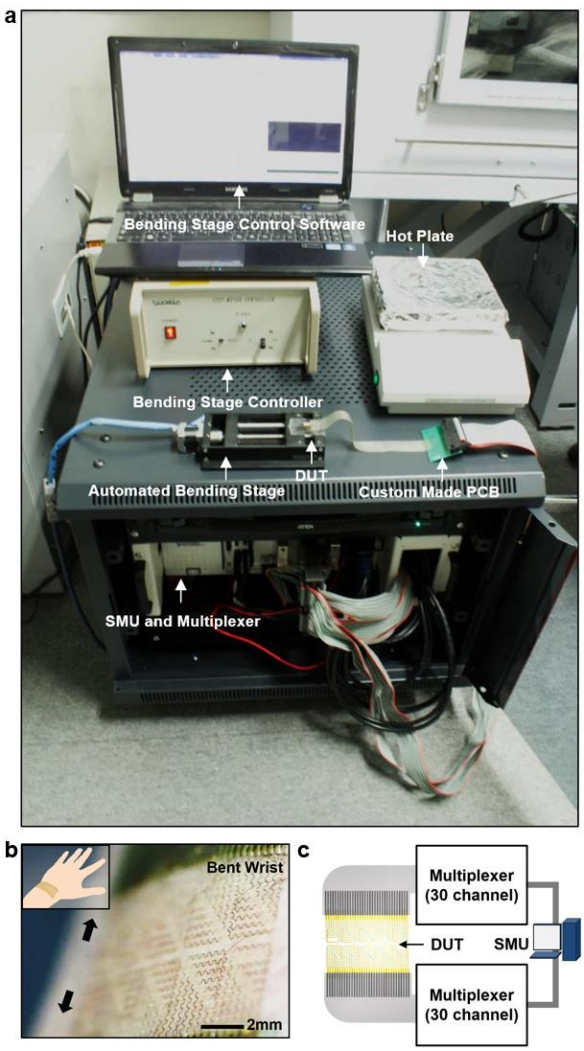

Figure 2.6. Experiment and measurement setup for stretching test. a, Experiment setup to measure the strain and temperature using SiNR-based sensor arrays. **b,** Magnified image of the conformally attached strain gauge arrays on the wrist. Inset shows the corresponding schematic illustration. **c,** Multiplexing schemes for measuring the regional strain distribution with the sensor arrays.

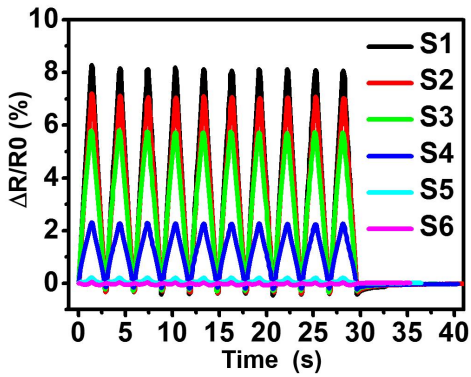

Figure 2.7. Temporal resistance changes of different curvature of SiNR under cyclical stretching.

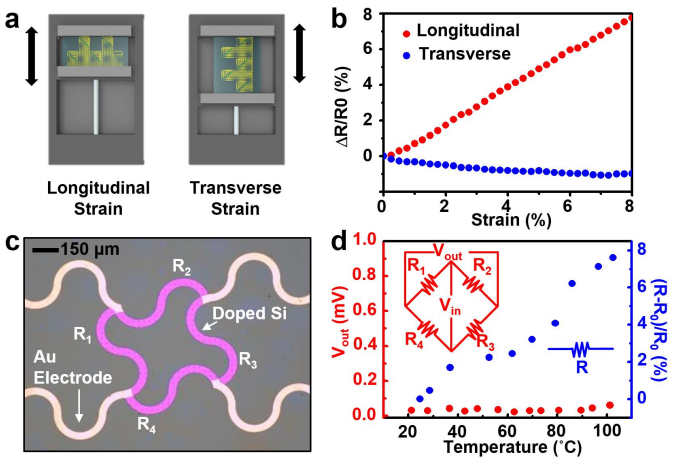

Figure 2.8. Stretching direction dependency and thermal effects on a strain gauge. a, Illustration of experimental setup for the analysis of stretching directional dependency of the SiNR strain gauge. **b,** Percent resistance changes of a SiNR strain gauge against longitudinal (red) and transverse (blue) strain. **c,** Microscope image of SiNR strain gauges in the Wheatstone bridge configuration. **d,** Output voltage changes measured from the Wheatstone bridge (red) and percent resistance change of single-resistor-based strain gauge (blue) as a function of temperature. Schematic diagram of the Wheatstone bridge (red inset) and single-resistor-based strain gauge (blue inset).

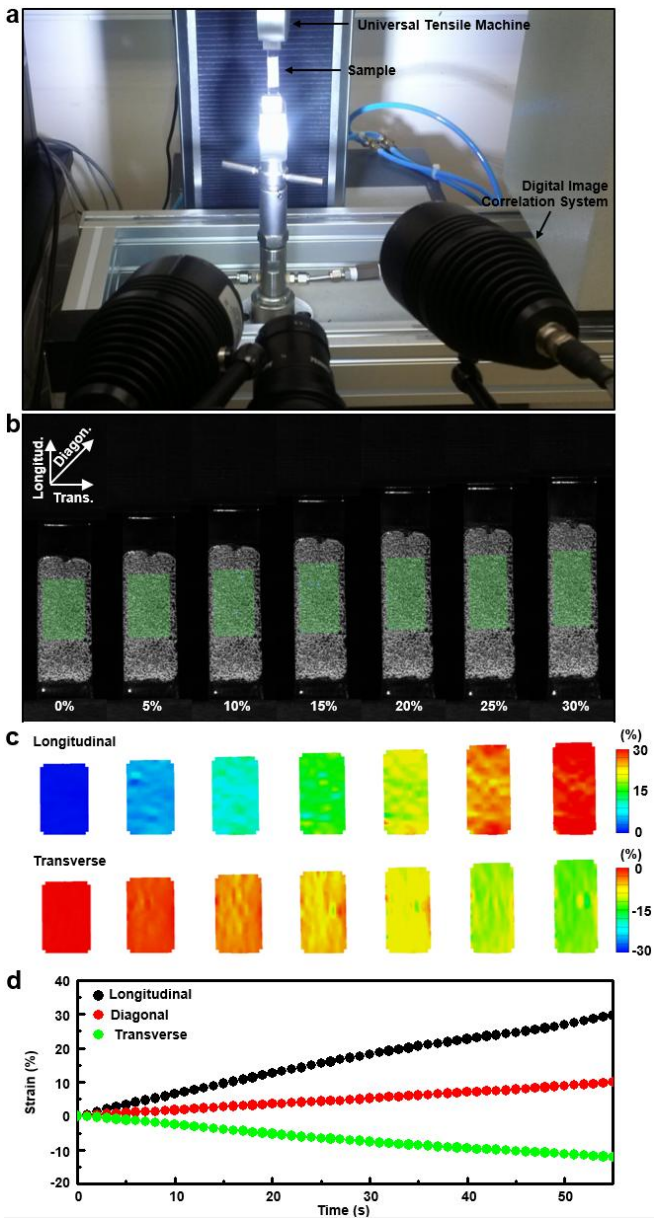

Figure 2.9. 2D strain distribution analysis of uniaxially stretched PDMS. a, Photograph of camera-based experimental setup used for analysis of the 2D strain distribution on uniaxially stretched PDMS. **b,** Serial images of

the stretched PDMS sample (0~30%). The sample is coated with paint in dot patterns to allow position recognition. Green rectangles in the figure indicate the measured region. **c,** Areal strain distributions in the longitudinal (top) and transverse (bottom) directions of the uniaxially stretched PDMS show changes which can be measured with strain gauge rosettes. **d,** Tri-axial changes in strain as a function of time. The stretching rate is 6 mm min^{-1}.

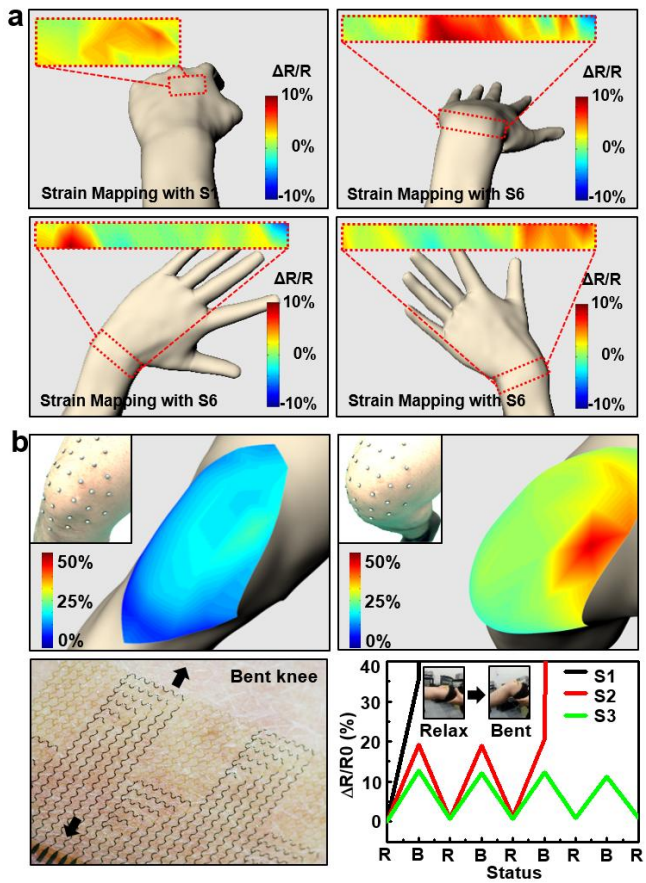

Figure 2.10. Strain measurement on various body parts. a, Regionally mapped percent resistance changes, measured by site-specifically designed strain gauge arrays (S1 for minimal stretch region, S6 for large stretch region). Mapped regions are indicated with red dotted box for four different motions. **b,** Detection of strains at the knee during the bending motion. Regional strain maps of the skin over the knee, calculated using positional information acquired by the motion capture system, in case of minimal bending (top left) and extreme bending (top right). Insets show the image of the knee with reflective markers. Magnified image of the

conformally attached strain gauge arrays on the bent knee (bottom left). Percent resistance changes of strain gauges with different designs (S1, S2, S3) depending on the motion status (repetitive relaxing and bending of the knee). S1 and S2 designs fail during the cyclic bending motion (bottom right).

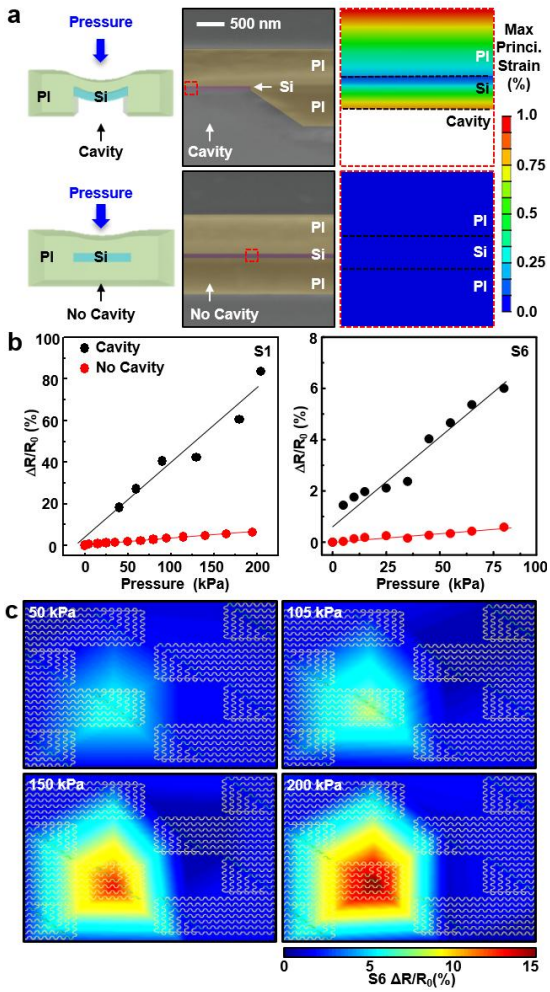

Figure 2.11. SiNR pressure sensors of different sensitivities and effects of a cavity on the sensitivity. a, Schematics show working principle of the SiNR pressure sensor with a cavity (top left) compared to the SiNR pressure sensor without a cavity (bottom left), SEM images of the device cross section with a cavity (top middle) and without one (bottom middle), and FEA results (top right; bottom right). **b,** The resistance changes of a pressure sensor with a cavity (black) and without a cavity (red) with

respect to the applied pressure for different design of the SiNR (S1: graph on the left, S6: graph on the right). **c,** Regionally mapped percent resistance changes measured by pressure sensor array of S6 for gradually increasing pressure.

2.3.4 Resistance changing mechanism of the serpentine SiNR sensors

There are two reasons for resistance change when the SiNR sensors are deformed: change of its dimension and piezoresistivity of the single crystalline silicon. When positive strain is applied to the SiNR sensor, it will be elongated and its resistance will be governed by the equation of $R=\rho L/A$, where ρ is bulk resistivity, L is the length of the sensor, and A is the area of the cross section. However, the mechanical elongation of the SiNR is limited, so the piezoresistivity effect mainly cause SiNR's resistance changes. The piezoresistivity of the SiNR depends on the mobility: $\mu = q\bar{t}/m^*$ where q is the charge per unit charge carrier, $\bar{t}$ is the mean free time between carrier collision events, and m^* is the effective mass of a carrier in the crystal lattice. Both $\bar{t}$ and m^* are dependent on lattice spacing which is changed by mechanical elongation/compression of the SiNR. Therefore, deformed area and degree of deformation have significant effects on the resistance changing of SiNR.

Resistance of SINR can be obtained by $R_0[1+\pi_L\sigma_{xx}+\pi_T(\sigma_{yy}+\sigma_{zz})]$, where R_0, π_L, π_T, σ_{ij} denote the resistance when no strain is applied, longitudinal and transverse piezoresistive coefficients, and tensile stress components in x, y, z directions. The piezoresistive coefficients are strongly dependent on the crystallographic axes. In case of the {100} wafers, the piezoresistive coefficient for p-type silicon shows maximum value in the <110> direction. Therefore, p-type SiNR strain gauge should be aligned along with the <110> direction during fabrication processes.

2.3.5. SiNR temperature sensors and Au based sensor/actuator

To measure temperature, SiNRs are doped twice to form p-n junctions (Figure 2.1d, right). Temperature sensors integrated onboard prosthetic skin should not be affected by mechanical deformations. Figure 2.12 shows I-V curves of distinctively designed temperature sensors (from S1 to S6 designs) at room temperature in response to applied strains. The divergence between each I-V curve under different strains is remarkably reduced as the curvature of sensors is increased (*e.g.* S6). The large curvature sensors allow for stable temperature measurements under a wide range of stretching conditions. I-V curves of S1 and S6 temperature sensors are obtained at different temperatures under 0% and 10% applied strain (Figure 2.13). Figure 2.14a shows calibration curves obtained by extracting voltages at specific current (~10 nA) from I-V curves. The calibration curves for S1 design show the dramatic shifts in response to applied strain, whereas the S6 design exhibits minimal change. Temperature sensors with S6 design are used to minimize the effect of mechanical deformations on the temperature sensing. The temperature sensor design with high curvature enables reliable temperature monitoring under various applied pressures (Figure 2.14b). A temperature distribution map is realized with these sensor arrays with and without local heating (Figure 2.14c). The temperature sensor array data streams are comparable, to those collected with a commercial IR camera as a control. To construct large area temperature sensor arrays, a multiplexing strategy is necessary

to minimize the wiring number. SiNR diode temperature sensors have a significant advantage in their construction owing to their rectifying characteristics.[29] The spatial resolution of the multiplexed temperature sensor array of SiNR diodes is sufficiently high to accurately recognize the thermal profile of a heated object (Figure 2.14d). Further increases in sensitivity can be achieved by incorporating novel nanomaterials/microstructures.[6, 30]

Although there is no specific biological receptor that senses skin exposure to humidity, human skin has the ability to sense changes in humidity with mechanoreceptors and thermo-receptors.[31] To mimic this capability, we fabricate stretchable capacitance-based humidity sensor arrays. Humidity sensing is performed in a test chamber with humidity control. The humidity sensor arrays detect capacitance changes induced by the permittivity change of PI, which absorbs water molecules (Figure 2.15a, left). A calibration curve (Figure 2.15, right) demonstrates this behavior. Spatial differences in humidity are discriminated (Figure 2.15b, left). External disturbances, such as fingertip touch (Figure 2.15b, right), external strains (Figure 2.15c, left), and temperature changes (Figure 2.15c, right) have negligible effects on the humidity sensing.

For prosthetic devices and artificial skin to feel natural, their temperature profile must be controlled to match that of the human body. We thus fabricate stretchable thermal actuator arrays, whose thermal signature is readily controllable. The temperature of heating array can be adjusted by controlling applied voltage and time (Figure 2.16a) Thermal

actuation performance remains intact under stretching conditions (Figure 2.16b, ~0% and ~10%).

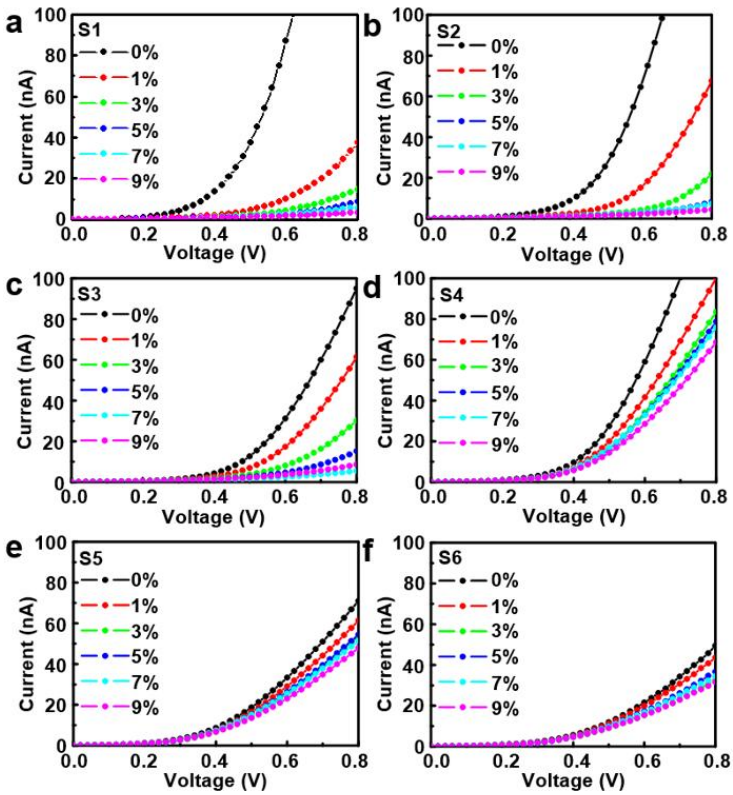

Figure. 2.12. I-V characteristic curves of temperature sensors under applied strains (0%, 1%, 3%, 5%, 7%, 9%) at room temperature with different designs. **a,** S1, **b,** S2, **c,** S3, **d,** S4, **e,** S5, **f,** S6.

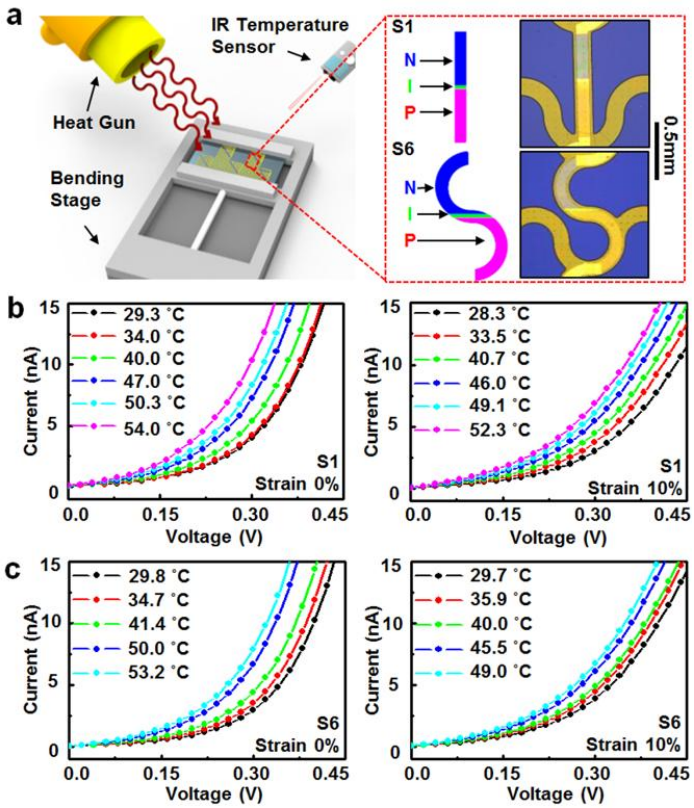

Figure. 2.13. Experimental setup and I-V curves of temperature sensors at different temperatures with various applied strains. **a,** Schematic of experimental setup for SiNR temperature sensor characterization. **b,** I-V curves of the S1 temperature sensor without (left) and with applied strain (10%, right). **c,** I-V curves of the S6 temperature sensor without (left) and with applied strain (10%, right).

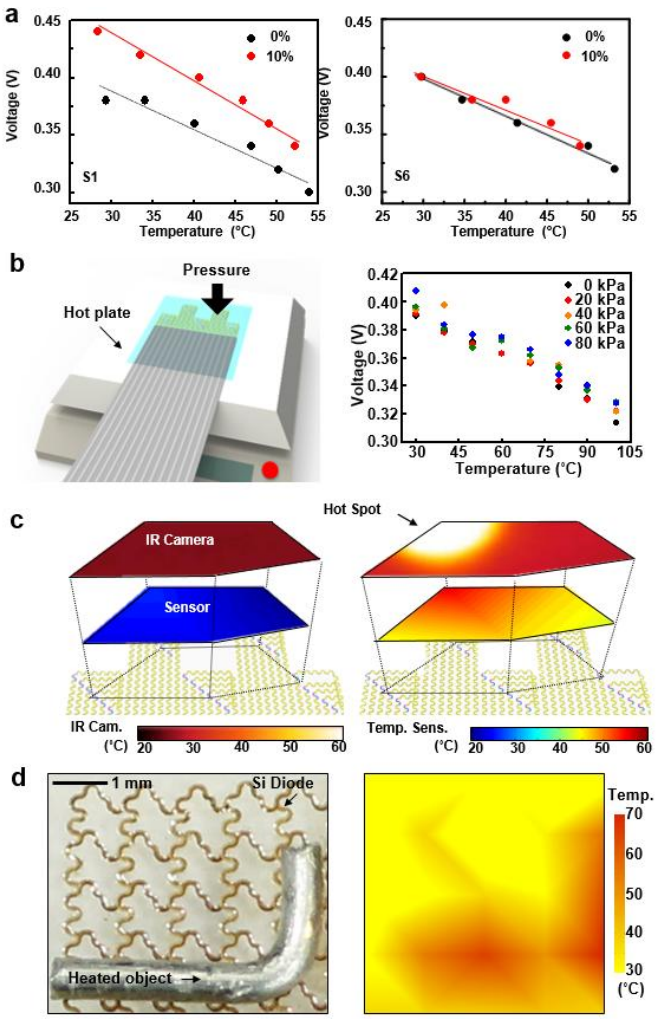

Figure 2.14. SiNR temperature sensor array characterization. a, Calibration curves of SiNR temperature sensors of representative designs (S1: graph on the left, S6: graph on the right) under 10% stretched (red) and unstretched conditions (black). **b,** An illustration of experimental setup for applying pressures to the S6 design temperature sensor array (left). Calibration curves of the temperature sensor under various applied

pressures (right), 0 kPa (black), 20 kPa (red), 40 kPa (orange), 60 kPa (green), and 80 kPa (blue). Calibration curves are obtained by extracting voltages from I-V curves at the specific current (1 μA). **c,** Regionally mapped temperature measured by an IR camera and the SiNR temperature sensor array of S6 for initial condition (left) and partially heated condition (right). **d,** A photograph of SiNRs diode based 5×5 temperature sensor array (left). A temperature map obtained by using the temperature sensor array showing a silhouette of the heated object (right).

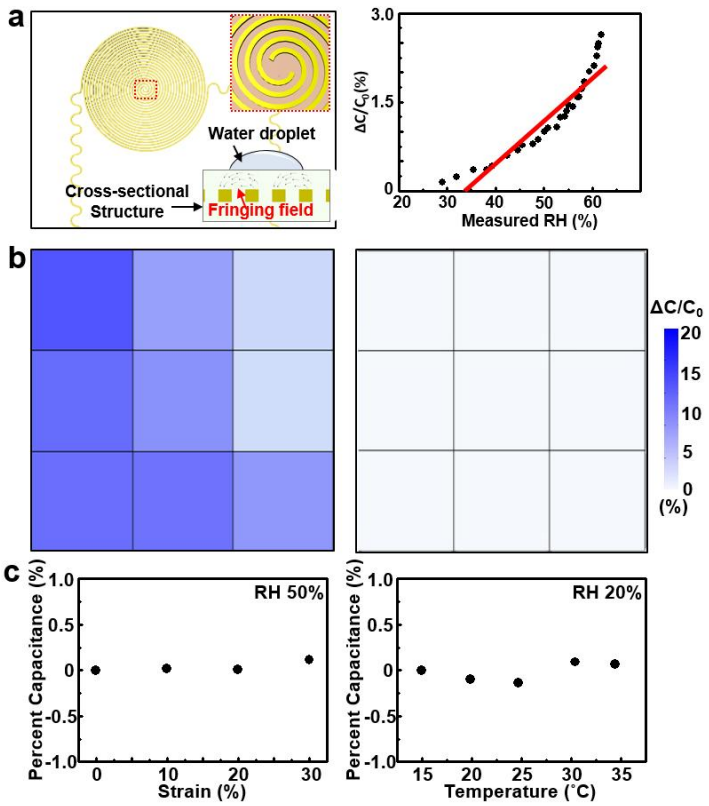

Figure 2.15. Humidity sensor characterization. a, Schematic diagram of humidity sensor (left) and sensing mechanism (inset). A calibration curve of the coplanar humidity sensor (right). **b,** Map of regional capacitance change when water droplets covering the partial area of the coplanar humidity sensor array (left). Responses of the capacitor sensor array the humidity sensor array is touched by a dry finger (right). **c,** Strain (left) and temperature (right) dependency of the humidity sensor, measured at the relative humidity (RH) of 50% and 20%, respectively. The humidity sensor shows negligible signal changes against the external strains and temperature changes.

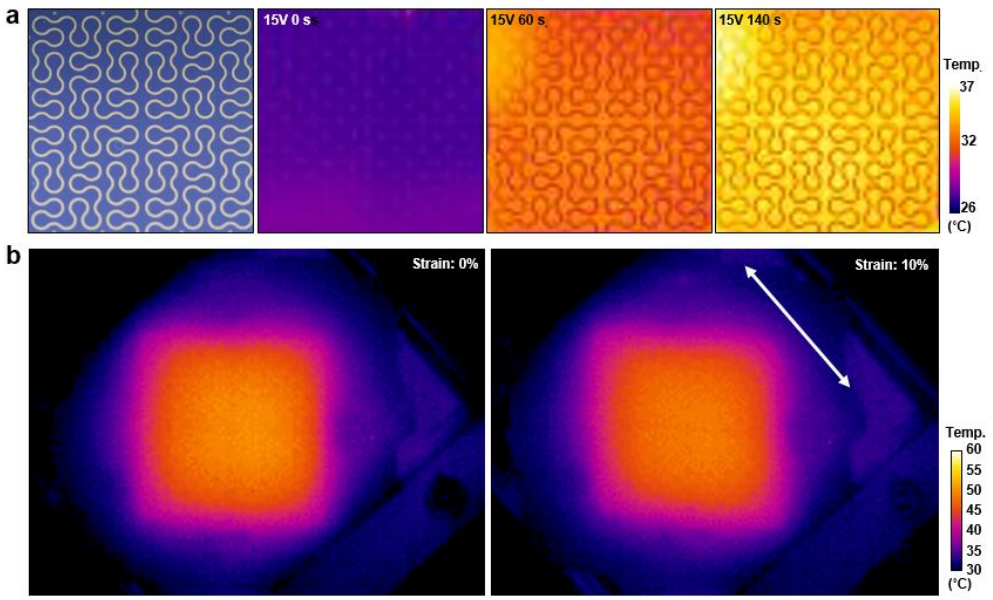

Figure 2.16. Heating capability of the stretchable heater under applied strains. a, An image of fractal-inspired stretchable heater (1st frame) and IR camera images of the heater when the voltage of 15 V is applied for different period of time (2nd~4th frame). **b,** Stretchability of heater. Heater is stretched from ~0% (left) to ~10% (right) with no degradation in heating performance.

2.3.6. Electronic skin responses in various daily life situations

The prosthetic hand and laminated electronic skin could encounter many complex operations such as hand shaking, ball grasping, holding a cup of hot/cold drink, touching dry/wet surfaces, and human to human contact. In the case of hand shaking, spatiotemporal strain can be mapped with SiNR strain gauge arrays. The strain map has high fidelity and captures minor shifts in strain near the index finger and respective joints (Figure 2.17). To investigate the performance of SiNR pressure sensors, we monitor temporal resistance changes in response to grasping of a ball (Figure 2.18). Pressure sensors show rapid and reliable responses to external stimuli. Temperature sensing is another important function of skin prosthesis. Temporal temperature monitoring is successfully done (red) once a hand touches a cup containing hot (Figure 2.19a) and cold (Figure 2.19b) liquid. Control temperature measurements are performed with an IR sensor (blue).

Another application for smart prosthetics is tactile sensing of dampness caused by fluid contact. Humidity sensors in the prosthetic skin provide feedback on the level of humidity and wetness in the representative example of a diaper (Figure 2.20, left and middle). The measured capacitance differences between dry and wet cases are clearly distinguishable (Figure 2.20, right). In addition, thermal actuators can provide the controlled heating to make the sense of touch from a prosthesis close to natural (Figure 2.21, left). The artificial skin with the

stretchable heater is warmed to ~36.5 ˚C (Figure 2.21, middle) to mimic body temperature. The heat transfer to the baby doll is then captured with an IR camera (Figure 2.21, right).

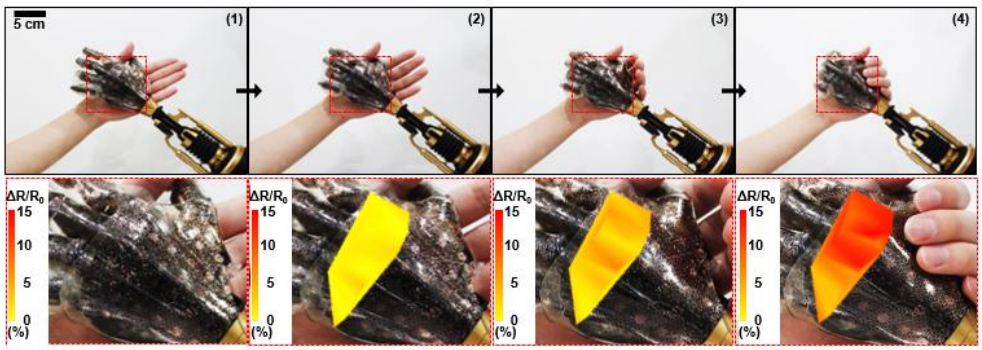

Figure 2.17. Electronic skin measuring strain distribution during handshake. Sequential images of prosthetic hand performing handshake. Spatiotemporal maps of resistance change of SiNR strain gauge arrays are overlapped at the corresponding locations on the back of hand.

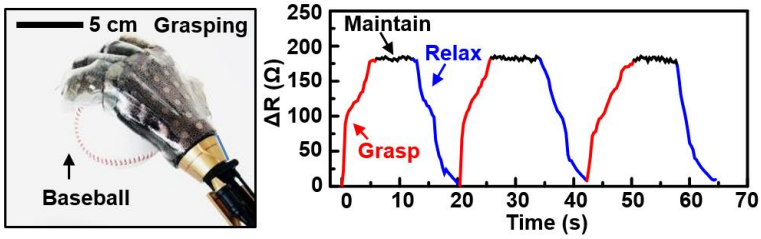

Figure 2.18. Electronic skin measuring pressure while grasping a ball. An image of the prosthetic limb catching a baseball (left) and a plot for the corresponding temporal resistance change of the SiNR pressure sensor, showing dynamics of the prosthetic hand in grasping, maintaining and relaxing motions (right).

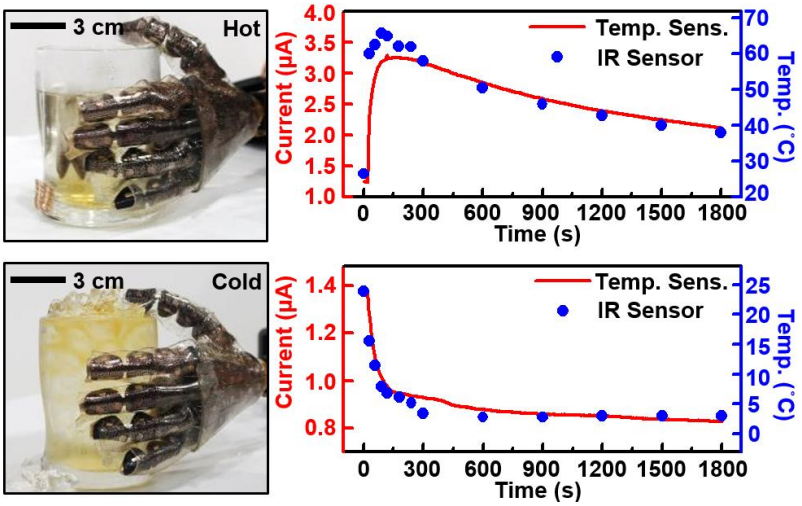

Figure 2.19. Electronic skin measuring temperature while holding a cold/hot cup. Image of the prosthetic limb touching a cup of hot (top left) and iced water (bottom left), and plots for the corresponding temporal current change of the SiNR temperature sensor (PIN diode, red) and actual temperature trace measured by IR sensor (blue) (top right: for the hot cup, bottom right: for the cold cup).

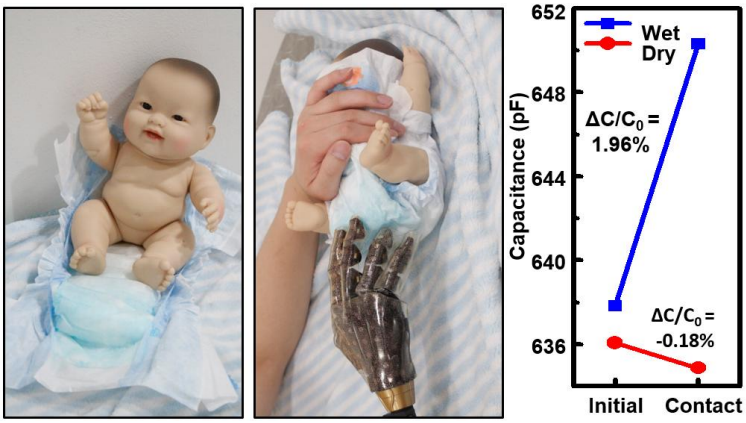

Figure 2.20. Electronic skin measuring humidity while touching a wet/dry diaper. Images of baby doll with the wet diaper (left) and the prosthetic hand touching the wet diaper (middle). Capacitance change of the humidity sensor (right) before/after touching the dry (red)/wet (blue) diaper.

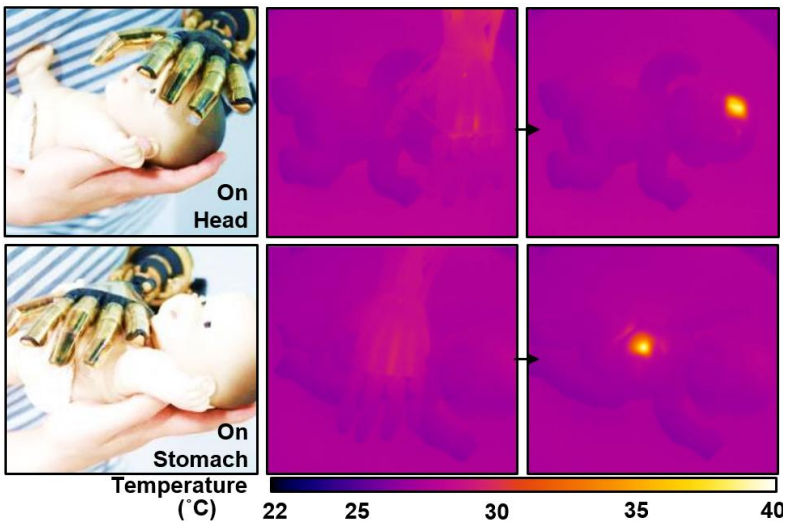

Figure 2.21. Electronic skin conveying warmth to the baby doll. Images of the prosthetic limb caring a baby doll touching head (top left) and stomach (bottom left), IR camera images of heated prosthetic hand to the body temperature by the heater in the artificial skin (top middle, bottom middle). The heat remained high after detaching the prosthetic hand (top right, bottom right).

2.3.7. Relaying sensory signals to peripheral nerves

The ultimate goal of the skin prosthesis is to let amputees feel external stimuli as if they feel through the actual skin. To achieve this goal, sensed signals from various sensors should be processed to stimulate the corresponding peripheral nervous system (Figure 2.22a and b). For effective charge injection to the peripheral nerve fibers, low impedance of interfacing electrode array (MEA) is essential.[32] In addition, there are various mechanical motions of adjacent muscles, which requires easy deformability of interfacing electrodes between electronics and biological tissues such as neurons.[33] Suppression of inflammation, which is often caused by reactive oxygen species (ROS),[34] is also important because severe inflammatory responses can kill nervous cells[35] and damage the peripheral nervous system.

To achieve low impedance, platinum nanowires (PtNWs; Figure 2.23a) are grown on the exposed electrodes in MEA. PtNWs are grown using an electrochemical method with anodic aluminum oxide (AAO) membrane which guides the growth of PtNWs. A solution of ceria nanoparticles is drop-casted on the PtNWs (Figure 2.23b) to suppress the ROS generation which might be toxic at high concentration.[34] The low material impedance of Pt and large surface area of NWs decrease the impedance lower than planar Au electrode (Figure 2.23c). Ceria nanoparticles decorated on PtNWs successfully scavenge ROS (H_2O_2

concentration: 1.64 μM) compared to the control (H_2O_2 concentration: 5 μ M), which prevents ROS-induced inflammations.[36]

Figure 2.23d shows the fabricated stretchable MEA conformally laminated on nerves (blue arrows) in muscle tissues (right). In a Sprague Dawley rat, the sciatic nerve is exposed for the experiment of relaying sensory signals to peripheral nerves. Signals from strain and pressure sensors (black) are obtained and processed as input signals (red), and injected to nerves (Figure 2.24). Input signals are injected through stretchable MEA and flowing current through nerves are measured (blue). The measured current shows similar signal shape with the sensor and input signals (Figure 2.24a and b), indicating successful signal injection through nanomaterials-decorated
stretchable MEA interfaces.

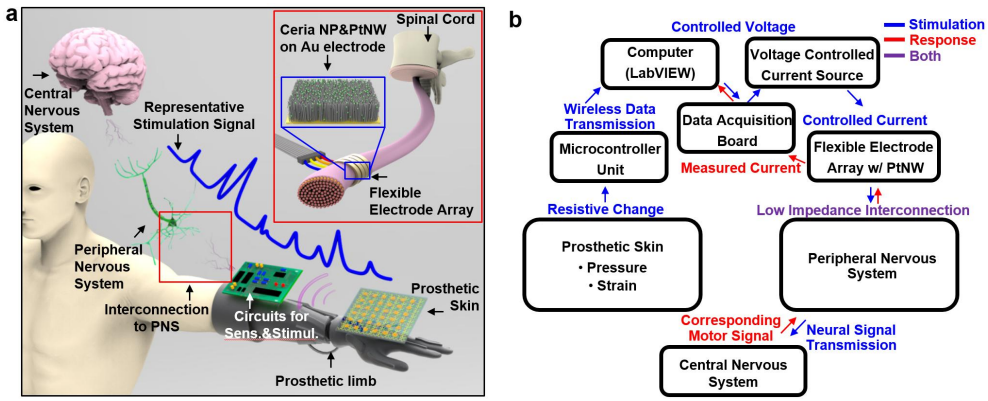

Figure 2.22. Conceptual illustration of experimental setup and data flows for relaying sensor signals to peripheral nerves. **a,** Schematic of necessary components for constructing neural interface to deliver sensed information to the nervous system. **b,** Detailed flow charts describing concept of the bidirectional feedback. Blue, red arrows and purple descriptions correspond to the case of stimulation, response to the stimulation, and both, respectively.

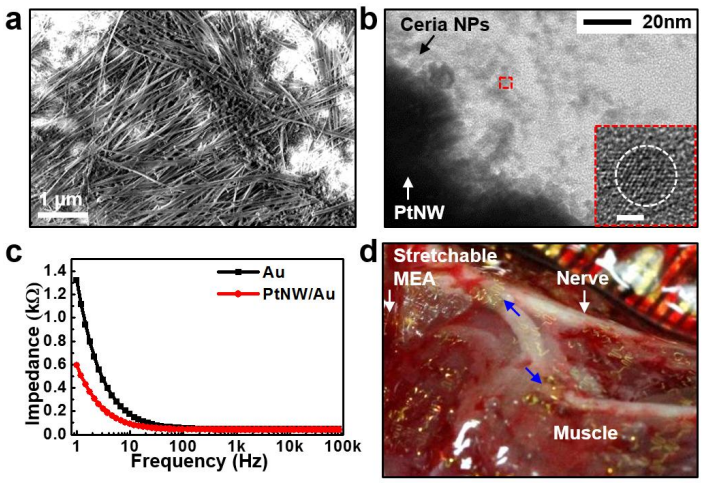

Figure 2.23. Modifications applied on the stretchable electrode array and its electrical characteristics. **a,** SEM image of PtNWs. **b,** TEM image of ceria nanoparticles decorated on a PtNW. **c,** Impedance of Au, PtNWs/Au electrodes with respect to frequency of applied signal. **d,** MEA on peripheral nerves in muscle tissues of a rat model.

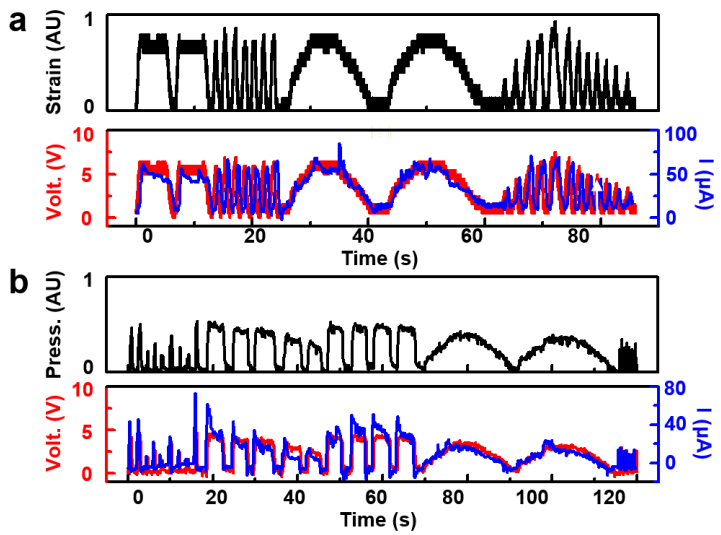

Figure 2.24. Demonstration of conveying sensor signals to peripheral nerves. a, Measured signals from a strain gauge embedded in the prosthetic skin (black), simultaneously applied electrical stimulation to the nerves according to the sensed signals (red) and delivered signals through the nerves (blue). **b,** Similar data sets as those shown in a, but obtained by using a pressure sensor in the prosthetic skin.

2.4 Conclusion

Site-specifically designed SiNR mechanical and temperature sensor arrays integrated with stretchable humidity sensors and thermal actuators enable high sensitivity, wide detection ranges, and mechanical durability for prosthetic systems. Motion capture videography provides a map of deformations of human skin in response to complex motions, thus forming the basis of site-specific geometries and designs for SiNR-based systems. Ultrathin layouts in neutral mechanical plane configurations further enhance durability and reduce risks of mechanical fractures. The MEA decorated with PtNWs and ceria nanoparticles highlight the unique capability to merge these abiotic systems with the human body. As a result, sensing and actuation capabilities are enabled over a wide range of sensory inputs, in the presence of skin deformations, thus providing enhanced function and high performance in the emerging field of smart prosthetics.

References

1. Dahiya, R. S., Valle, M. Robotic tactile sensing Ch. 3. Springer Science+Business Media, Dordrecht (2013).
2. Ma, Q. F. Labeled lines meet and talk: population coding of somatic sensations. *J Clin. Invest.* **120**, 3773-3778 (2010).
3. Dahiya, R. S., Valle, M. Robotic tactile sensing Ch. 1. Springer Science+Business Media, Dordrecht (2013).
4. Jacobsen, S. C., Knutti, D. F., Johnson, R. T., Sears, H. H. Development of the utah artificial arm. *IEEE Trans. Biomed. Eng.* **29**, 249-269 (1982).
5. Raspopovic, S., Capogrosso, M., Petrini, F. M., Bonizzato, M., Rigosa, J., Di Pino, G., Carpaneto, J., Controzzi, M., Boretius, T., Fernandez, E., Granata, G., Oddo, C. M., Citi, L., Ciancio, A. L., Cipriani, C., Carrozza, M. C., Jensen, W., Guglielmelli, E., Stieglitz, T., Rossini, P. M., Micera, S. Restoring natural sensory feedback in real-time bidirectional hand prostheses. *Sci. Transl. Med.* **6**, 222ra19 (2014).
6. Graz, I., Krause, M., Bauer-Gogonea, S., Bauer, S., Lacour, S. P., Ploss, B., Zirkl, M., Stadlober, B., Wagner, S. Flexible active-matrix cells with selectively poled bifunctional polymer-ceramic nanocomposite for pressure and temperature sensing skin. *J. Appl. Phys.* **106**, 034503 (2009).
7. Mannsfeld, S. C. B., Tee, B. C. K., Stoltenberg, R. M., Chen, C. V. H. H., Barman, S., Muir, B. V. O., Sokolov, A. N., Reese, C., Bao, Z. N. Highly sensitive flexible pressure sensors with

microstructured rubber dielectric layers. *Nat. Mater.* **9**, 859-864 (2010).

8. Lipomi, D. J., Vosgueritchian, M., Tee, B. C. K., Hellstrom, S. L., Lee, J. A., Fox, C. H., Bao, Z. N. Skin-like pressure and strain sensors based on transparent elastic films of carbon nanotubes. *Nat. Nanotech.* **6**, 788-792 (2011).
9. Pang, C., Lee, G. Y., Kim, T. I., Kim, S. M., Kim, H. N., Ahn, S. H., Suh, K. Y. A flexible and highly sensitive strain-gauge sensor using reversible interlocking of nanofibres. *Nat. Mater.* **11**, 795-801 (2012).
10. Persano, L., Dagdeviren, C., Su, Y. W., Zhang, Y. H., Girardo, S., Pisignano, D., Huang, Y. G., Rogers, J. A. High performance piezoelectric devices based on aligned arrays of nanofibers of poly(vinylidenefluoride-co-trifluoroethylene). *Nat. Commun.* **4**, 1633 (2013).
11. Vandeparre, H., Watson, D., Lacour, S. P. Extremely robust and conformable capacitive pressure sensors based on flexible polyurethane foams and stretchable metallization. *Appl. Phys. Lett.* **103**, 204103 (2013).
12. Kim, D. H., Lu, N. S., Ma, R., Kim, Y. S., Kim, R. H., Wang, S. D., Wu, J., Won, S. M., Tao, H., Islam, A., Yu, K. J., Kim, T. I., Chowdhury, R., Ying, M., Xu, L. Z., Li, M., Chung, H. J., Keum, H., Mccormick, M., Liu, P., Zhang, Y. W., Omenetto, F. G., Huang, Y. G., Coleman, T., Rogers, J. A. Epidermal electronics. *Science* **333**, 838-843 (2011).

13. Lu, N. S., Lu, C., Yang, S. X., Rogers, J. Highly sensitive skin-mountable strain gauges based entirely on elastomers. *Adv. Funct. Mater.* **22**, 4044-4050 (2012).

14. Jung, S., Kim, J. H., Kim, J., Choi, S., Lee, J., Park, I., Hyeon, T., Kim, D. H. Reverse-micelle-induced porous pressure-sensitive rubber for wearable human-machine interfaces. *Adv. Mater.* **26**, 4825-4830 (2014).

15. Someya, T., Kato, Y., Sekitani, T., Iba, S., Noguchi, Y., Murase, Y., Kawaguchi, H., Sakurai, T. Conformable, flexible, large-area networks of pressure and thermal sensors with organic transistor active matrixes. *Proc. Natl. Acad. Sci. USA* **102**, 12321-12325 (2005).

16. Sekitani, T., Yokota, T., Zschieschang, U., Klauk, H., Bauer, S., Takeuchi, K., Takamiya, M., Sakurai, T., Someya, T. Organic nonvolatile memory transistors for flexible sensor arrays. *Science* **326**, 1516-1519 (2009).

17. Sekitani, T., Zschieschang, U., Klauk, H., Someya, T. Flexible organic transistors and circuits with extreme bending stability. *Nat. Mater.* **9**, 1015-1022 (2010).

18. Kaltenbrunner, M., Sekitani, T., Reeder, J., Yokota, T., Kuribara, K., Tokuhara, T., Drack, M., Schwodiauer, R., Graz, I., Bauer-Gogonea, S., Bauer, S., Someya, T. An ultra-lightweight design for imperceptible plastic electronics. *Nature* **499**, 458-463 (2013).

19. Takei, K., Takahashi, T., Ho, J. C., Ko, H., Gillies, A. G., Leu, P. W., Fearing, R. S., Javey, A. Nanowire active-matrix circuitry

for low-voltage macroscale artificial skin. *Nat. Mater.* **9**, 821-826 (2010).

20. Wang, C., Hwang, D., Yu, Z. B., Takei, K., Park, J., Chen, T., Ma, B. W., Javey, A. User-interactive electronic skin for instantaneous pressure visualization. *Nat. Mater.* **12**, 899-904 (2013).

21. Yang, S. X., Lu, N. S. Gauge factor and stretchability of silicon-on-polymer strain gauges. *Sensors* **13**, 8577-8594 (2013).

22. Son, D., Lee, J., Qiao, S., Ghaffari, R., Kim, J., Lee, J. E., Song, C., Kim, S. J., Lee, D. J., Jun, S. W., Yang, S., Park, M., Shin, J., Do, K., Lee, M., Kang, K., Hwang, C. S., Lu, N. S., Hyeon, T., Kim, D. H. Multifunctional wearable devices for diagnosis and therapy of movement disorders. *Nat. Nanotech.* **9**, 397-404 (2014).

23. Ying, M., Bonifas, A. P., Lu, N. S., Su, Y. W., Li, R., Cheng, H. Y., Ameen, A., Huang, Y. G., Rogers, J. A. Silicon nanomembranes for fingertip electronics. *Nanotechnology* **23**, (2012).

24. Webb, R. C., Bonifas, A. P., Behnaz, A., Zhang, Y. H., Yu, K. J., Cheng, H. Y., Shi, M. X., Bian, Z. G., Liu, Z. J., Kim, Y. S., Yeo, W. H., Park, J. S., Song, J. Z., Li, Y. H., Huang, Y. G., Gorbach, A. M., Rogers, J. A. Ultrathin conformal devices for precise and continuous thermal characterization of human skin. *Nat. Mater.* **12**, 1078-1078 (2013).

25. Fan, J. A., Yeo, W. H., Su, Y. W., Hattori, Y., Lee, W., Jung, S. Y., Zhang, Y. H., Liu, Z. J., Cheng, H. Y., Falgout, L., Bajema, M., Coleman, T., Gregoire, D., Larsen, R. J., Huang, Y.

G., Rogers, J. A. Fractal design concepts for stretchable electronics. *Nat. Commun.* **5**, 3266 (2014).

26. Li, X. P., Kasai, T., Nakao, S., Tanaka, H., Ando, T., Shikida, M., Sato, K. Measurement for fracture toughness of single crystal silicon film with tensile test. *Sensor Actuat. A-Phys.* **119**, 229-235 (2005).

27. Suo, Z. G. Mechanics of stretchable electronics and soft machines. *MRS Bull.* **37**, 218-225 (2012).

28. Kim, D. H., Ghaffari, R., Lu, N. S., Wang, S. D., Lee, S. P., Keum, H., D'angelo, R., Klinker, L., Su, Y. W., Lu, C. F., Kim, Y. S., Ameen, A., Li, Y. H., Zhang, Y. H., De Graff, B., Hsu, Y. Y., Liu, Z. J., Ruskin, J., Xu, L. Z., Lu, C., Omenetto, F. G., Huang, Y. G., Mansour, M., Slepian, M. J., Rogers, J. A. Electronic sensor and actuator webs for large-area complex geometry cardiac mapping and therapy. *Proc. Natl. Acad. Sci. USA* **109**, 19910-19915 (2012).

29. Han, I. Y., Kim, S. J. Diode temperature sensor array for measuring micro-scale surface temperatures with high resolution. *Sensor Actuat. A-Phys.* **141**, 52-58 (2008).

30. Tien, N. T., Jeon, S., Kim, D. I., Trung, T. Q., Jang, M., Hwang, B. U., Byun, K. E., Bae, J., Lee, E., Tok, J. B. H., Bao, Z. N., Lee, N. E., Park, J. J. A Flexible bimodal sensor array for simultaneous sensing of pressure and temperature. *Adv. Mater.* **26**, 796-804 (2014).

31. Ackerley, R., Olausson, H., Wessberg, J., Mcglone, F. Wetness perception across body sites. *Neurosci. Lett.* **522**, 73-77 (2012).

32. Spira, M. E., Hai, A. Multi-electrode array technologies for neuroscience and cardiology. *Nat. Nanotech.* **8**, 83-94 (2013).

33. Viventi, J., Kim, D. H., Vigeland, L., Frechette, E. S., Blanco, J. A., Kim, Y. S., Avrin, A. E., Tiruvadi, V. R., Hwang, S. W., Vanleer, A. C., Wulsin, D. F., Davis, K., Gelber, C. E., Palmer, L., Van Der Spiegel, J., Wu, J., Xiao, J. L., Huang, Y. G., Contreras, D., Rogers, J. A., Litt, B. Flexible, foldable, actively multiplexed, high-density electrode array for mapping brain activity in vivo. *Nat. Neurosci.* **14**, 1599-1605 (2011).

34. Grill, W. M., Norman, S. E., Bellamkonda, R. V. Implanted neural interfaces: biochallenges and engineered solutions. *Annu. Rev. Biomed. Eng.* **11**, 1-24 (2009).

35. Zhong, Y. H., Bellamkonda, R. V. Biomaterials for the central nervous system. *J. R. Soc. Interface* **5**, 957-975 (2008).

36. Kim, C. K., Kim, T., Choi, I. Y., Soh, M., Kim, D., Kim, Y. J., Jang, H., Yang, H. S., Kim, J. Y., Park, H. K., Park, S. P., Park, S., Yu, T., Yoon, B. W., Lee, S. H., Hyeon, T. Ceria nanoparticles that can protect against ischemic stroke. *Angew. Chem. Int. Edit.* **51**, 11039-11043 (2012).

Chapter 3. Skin mountable multiplexed silicon nonvolatile memory for storing physiological information

3.1 Introduction

Flash memory based on single-crystal silicon (Si) has become the dominant nonvolatile data storage device owing to its high performance and compatibility with complementary metal–oxide–semiconductor (CMOS) processes.[1-3] In flash memory, information is converted into a charge level and then stored in floating gates (FGs).[4] Therefore, the FGs determine the performance of the flash memory. However, FGs based on conventional conducting thin films face challenges such as difficulties in modulation of charge trap density and charge losses via locally distributed defects.[4-6]

Various studies have investigated new materials to replace those used in conventional FGs in order to achieve increased charge storage efficiency.[7-10] As a viable alternative, gold nanoparticle (AuNP) FGs have been proposed.[11-16] AuNP FGs afford many advantages such as controllability of charge trap density, superb chemical stability, high work function, and, most importantly, efficient charge confinement.[17] However, nanoscale experimental observation of charge confinement in closely packed AuNPs FGs has not been reported yet. Such characterization

capability is useful for understanding different aspects of charge confinement in various types of AuNPs FGs (*e.g.*, different size or density of AuNPs), enabling further optimization to improve memory performances. In addition, most of previous nanocrystal-based memory devices have focused on a single memory cell instead of a multiplexed memory array in which each cell is individually addressable.[11, 12]

At the same time, rapid developments in wearable electronics have led to an urgent demand for deformable electronic devices such as sensors,[18-24]circuits,[25-27] displays,[28-30] and memories.[11, 12, 31-34] Most deformable memory devices reported so far, however, are just flexible. These kinds of memory devices are not compatible with wearable applications that require complicated modes of mechanical deformations such as stretching.[35, 36] Although previously reported stretchable flash memory[37] showed some advances, the isolated memory cells rather than interconnected ones, relatively unstable data storage owing to intrinsic hysteresis of carbon nanotubes, and metal thin film FGs that lead to incomplete charge confinement have impeded its use in practical applications. Reliability of the fabricated devices under ambient conditions and process compatibility with conventional CMOS fabrication processes are additional important factors. Considering these, the stretchable memory based on single-crystal silicon nanomembranes (SiNMs) is a good candidate for the wearable electronic device applications.[34, 38] Although many previous studies have investigated stretchable Si electronics such as diodes,[35, 36] transistors,[39] sensors and actuators,[34, 38, 40] and logic circuits,[41]

the deformable charge trap FG memory (CTFM) based on single-crystal Si has not yet been reported. The integration of Si CTFMs with other sensors and electronics in one wearable platform is another important unmet goal. To realize a large memory window and capacity with high cell-to-cell uniformity, an efficient large-area fabrication process for the uniform and high-density assembly of AuNPs for FGs in CTFMs on a Si electronics platform is an additional key requirement.

To address these critical issues, in this study, we developed wearable SiNM CTFMs with AuNP FGs assembled by the Langmuir-Blodgett (LB) method. We experimentally confirmed particle-level charge confinement without charge delocalization in closely packed AuNPs. This affords long retention time of memory devices. FGs assembled by the LB method have a large memory window and high cell-to-cell uniformity. The CTFM array is multiplexed by Si electronics for addressing and data storage in individual cells. The high stability and reliability of SiNM electronics under ambient conditions enables the realization of an ultrathin, high-density, and high-performance wearable CTFM array for practical applications. As a potential application of wearable electronics, this study focuses on monitoring heart rates. By interfacing with wearable Si amplifiers and electrodes on-board, the heart rates after exercise stress tests as extracted from monitored electrocardiogram (ECG) signals are processed and stored in CTFMs. The stored data can be retrieved later for the diagnosis of cardiac dysfunctions.

*** The contents of this chapter were published in *Science Advances*, 2016, *2*, e1501101.**

3.2. Experimental section

Fabrication of FG cell: The fabrication of the FG cell begins with the dry oxidation process of a Si wafer to grow a 5-nm-thick SiO_2 tunneling oxide (T_{ox}) layer. The AuNP FG assembled by the LB method is then coated on T_{ox}. An Al_2O_3 blocking oxide (B_{ox}) layer (7 nm) is deposited on the AuNPs FG using the PEALD process (150 °C, 50 cycles). For comparing retention characteristics, Au film (26 nm) FG and 3-layer AuNP (~26 nm) FG are utilized. Generally, the thermal deposition of Au film whose thickness is below 10 nm is difficult to achieve. Au deposition less than 10 nm normally leads to formation of islands, which is difficult to represent Au film characteristics.[11] Therefore, we used thicker Au film (~26 nm). For valid comparison, similar thickness of assembled AuNPs (3-layer AuNPs) is used.

Charge confinement characterization in FG cell: Nanoscale/microscale charge injections and measurements on the FG cell are conducted using AFM (XE7, Park Systems, Korea) with EFM. The AFM lithography program (XEL, Park Systems, Korea, for data shown in Figure 3.1b and c) or manual manipulation (for data shown in Fig. 3D) are used to pattern and generate a potential difference between an AFM tip and the bottom electrode for nanoscale/microscale patterned charge injection to the FG cell using the contact mode of the AFM. The AFM topography and EFM images are simultaneously retrieved by applying AC bias to a Pt/Cr

coated tip (tip radius: <25 nm; Budget Sensors Multi75E). Sinusoidal AC bias with a frequency of 14.6 kHz and peak-to-peak amplitude of 1 V are applied for acquiring topological data and EFM images using the non-contact mode of the AFM. The coupled topography with EFM data can be observed by adjusting the frequencies of AC bias and non-contact resonant. It is obtained by coupling the van der Waals force and electric force between the AFM tip and the surface of the FG cell, and it shows superior spatial resolution in illustrating a charge-containing area. The decoupled topography can also be obtained by fine-tuning the frequencies of the tip vibration and AC bias.

Fabrication of CTFM array: The fabrication begins with doping of p-type silicon-on-insulator (top silicon, 340 nm, Soitec) wafer with ion implantation (R_P: 50 nm, dose: 1×10^{16} ions/cm^2, phosphorus) to define n-type source and drain regions. After the doping process, top SiNM is transferred onto PI film (2 μm) coated on a SiO_2 wafer. Using reactive ion etching (RIE, SF_6 plasma) with photolithography, the active regions of the SiNM are isolated. The Al_2O_3 T_{ox} layer is deposited on the SiNM by PEALD process (250 °C, 50 cycles). After the deposition of AuNPs using LB method on whole area of the T_{ox}, the AuNPs are patterned with photolithography and wet etching to be confined on the channel area of the SiNM. The Al_2O_3 B_{ox} layer is subsequently deposited by the PEALD process (150 °C, 350 cycles). The Al_2O_3 layers (T_{ox} and B_{ox}) are patterned by photolithography and wet-etched using diluted hydrogen

fluoride solution (2%). To form the word lines, deposition of the metal film using thermal evaporation (Au/Cr, 100 nm/7 nm), photolithography and wet-etching processes are conducted in sequence. To electrically isolate between the word lines and bit lines, SU-8 2 (MicroChem, USA, 1 μm) is coated. The SU-8 layer is then photolithographically patterned to form vertical interconnect accesses (VIAs). The bit lines are deposited by thermal evaporation (Au/Cr, 150 nm/7 nm), patterned with photolithography and subsequent wet etch, contacting the source/drain regions through the VIAs. After the top PI layer (1 μm) is coated and annealed, the whole structure (PI/device/SU-8 2/PI) is patterned and etched by RIE (O_2 plasma). As a final step, the whole device is detached from the SiO_2 wafer and transferred onto a polydimethylsiloxane (PDMS) substrate.

Characterization of CTFM: The electrical characteristics of a CTFM are measured using a parameter analyser (B1500A, Agilent, USA). A high-voltage semiconductor pulse generator unit (HV-SPGU, Agilent, USA) is used to apply PGM/ERS pulses (-40 to 40 V) to the CTFM for a certain period of time (1 μs to 1 s). Source measure units (SMUs; Agilent, USA) are used to apply the drain-source voltage (V_{DS}) and gate-source voltage (V_{GS}) to the CTFM and to measure the drain current (I_d). All measured transfer characteristics of the CTFM are obtained using V_{DS}= 0.1 V. The threshold voltage is defined as the corresponding V_{GS} that induces I_d = 100 nA.

FEA of CTFM array and pseudo-CMOS inverter: FEA is used to analyse the strain distribution of a CTFM array and pseudo-CMOS inverter during stretching. The CTFM array and pseudo-CMOS inverter are modelled using four-node composite shell elements. The devices are placed on 1-mm-thick PDMS substrates that are modelled with eight-node solid elements. We assume perfect bonding (no slip condition) between devices and PDMS substrates. To simulate stretching, the stretching boundary conditions are applied on the bottom surface of the substrate. The linear elasticity represents the behaviour of the materials of the CTFM array and pseudo-CMOS inverters.

Fabrication of pseudo-CMOS inverter: As previously described in CTFM fabrication methods, the active regions of the doped SiNM transferred onto the PI layer (thickness: 1 μm) are isolated using RIE (SF_6 plasma) with photolithography. A 60-nm-thick SiO_2 gate dielectric layer is deposited by using plasma-enhanced chemical vapour deposition (PECVD) at 300 °C. The subsequent deposition and patterning of a metal layer is conducted using thermal evaporation (Au/Cr, 100 nm/7 nm), photolithography, and wet etching to form the gate, source, and drain interconnections. The top PI layer (thickness: 1 μm) is coated and annealed. The entire trilayer (PI/device/PI) is patterned and etched by RIE (O_2 plasma). The fabricated pseudo-CMOS inverter is then transferred onto a PDMS substrate, as described previously.

3.3. Results and discussion

3.3.1. Nanoscale charge confinement at AuNP FG and its experimental validation

An AuNP-based FG cell (insulator-FG-insulator-semiconductor structure) is fabricated to verify the nanoscale charge confinement. A conductive atomic force microscopy (AFM) tip with applied potential of 7 V contacts the top insulation layer (B_{ox}) of the FG cell and injects charges following predetermined patterns (Figure 3.1a). The potential difference between the AFM tip and the bottom Si substrate facilitates the trapping of electrons in the AuNP FG (Figure 3.1a, red dotted box). A series of AFM writings finishes the patterned charge injection.

The nanoscale charge confinement in an FG is characterized by the modified AFM measurement. The local electric force produced by confined charges is measured by topographical AFM coupled with electric force microscopy (EFM) data to observe the confined charge pattern (Figure 3.1b). The coupled image (EFM and AFM) clearly shows nanoscale charge confinement (minimum line width: 70 nm) without lateral charge transport (Figure 3.1c, left). The topographic image decoupled from EFM data (Figure 3.1c, right) shows the actual roughness. The efficient particle-level charge confinement of the AuNP FG leads to CTFMs with long retention time and large charge storage capacity, which is particularly important in next-generation nanoscale nonvolatile memory devices.[6]

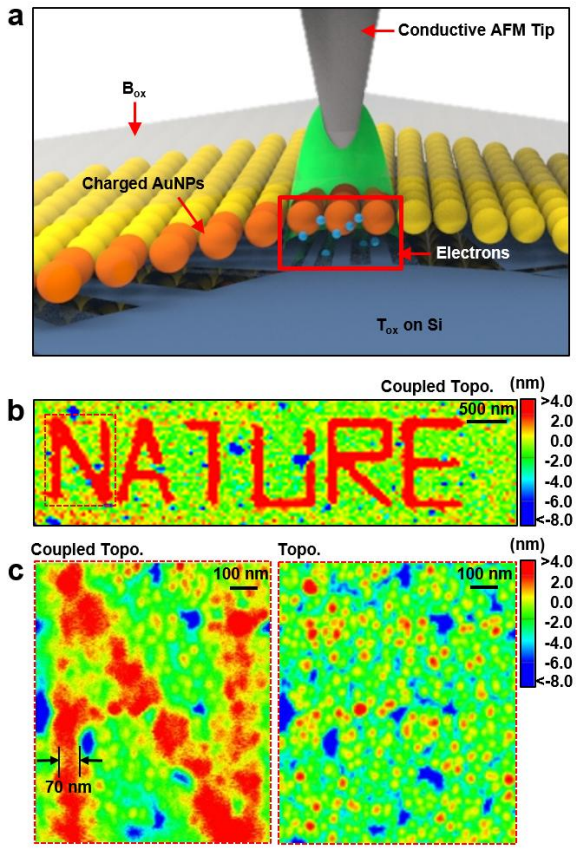

Figure 3.1. Characterization of nanoscale charge confinement at AuNP FG. **a,** Schematic showing process of charge injection to AuNP FG using a conductive AFM tip. **b,** Representative topographic AFM image coupled with EFM data showing nanoscale charge confinement capability of AuNPs. **c,** Magnified coupled topographical image of character "N," showing particle-level charge confinement within sub-100-nm width (left) and the corresponding topographical image decoupled with EFM data right).

3.3.2. Integration of CTFM and Si electronics as wearable system

Figure 3.2a and b shows a 22 × 22 CTFM array and its magnified view showing eight CTFMs, respectively. All CTFMs in the array are based on Si transistors and are fully multiplexed; individually accessed; and readily programmed, erased, and read by the off-chip control. The LB method can be used for the large-area fabrication of a closely packed AuNP FG which guarantees highly uniform CTFM performance. The AuNP FG is located between the T_{ox} and B_{ox} (Figure 3.2c).

Figure 3.3a shows the schematic of the demonstration system and its exploded view showing layered structure. Figure 3.3b shows a fabricated demonstration system composed of wearable CTFM array, stretchable electrodes, and voltage amplifiers. The amplifier comprises Si pseudo-CMOS inverters.[42] ECG signals are measured through stretchable electrodes and then amplified by the co-located stretchable amplifiers. Subsequently, the heart rate is extracted from the amplified ECG signals and stored in the CTFMs. The CTFM's ultrathin structure (~5 μm) and serpentine interconnects enable its conformal lamination on the skin under various mechanical deformations including poking and compressing (Figure 3.3c). The detailed fabrication is described in the Figure 3.4. The single-crystal nature of Si provides high performance in a multiplexed array.

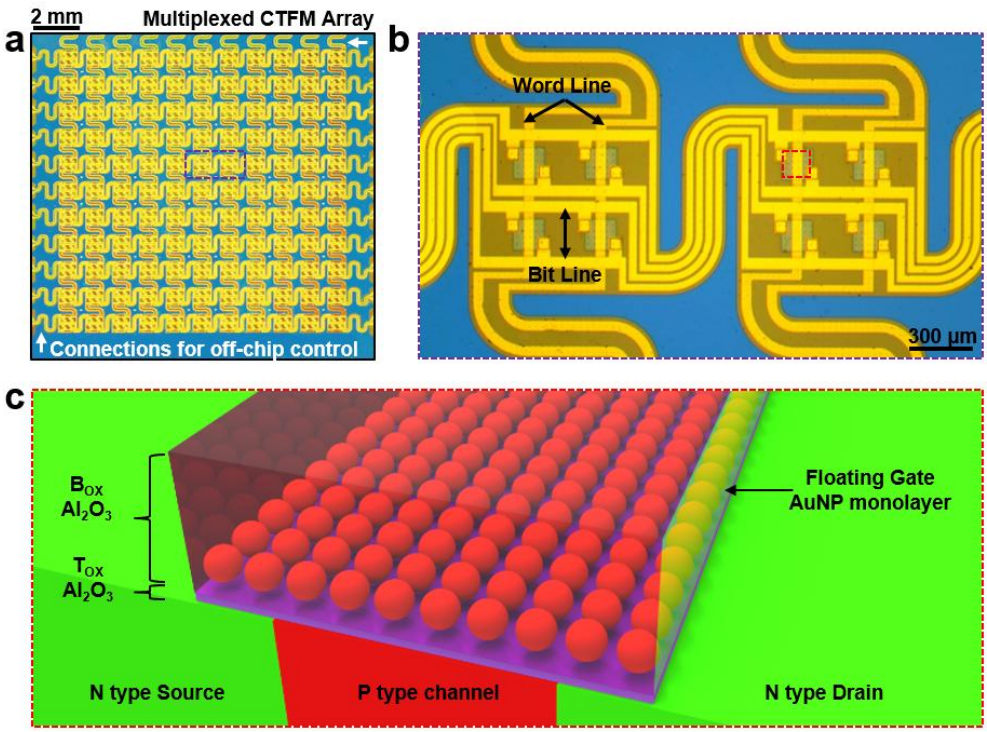

Figure 3.2. Fabricated wearable memory array and its structure. a, Photograph of a 22 × 22 wearable multiplexed CTFM array. **b,** The magnified image shows eight memory pixels interconnected with word lines and bit lines. **c,** Magnified schematic of the channel area of a single CTFM.

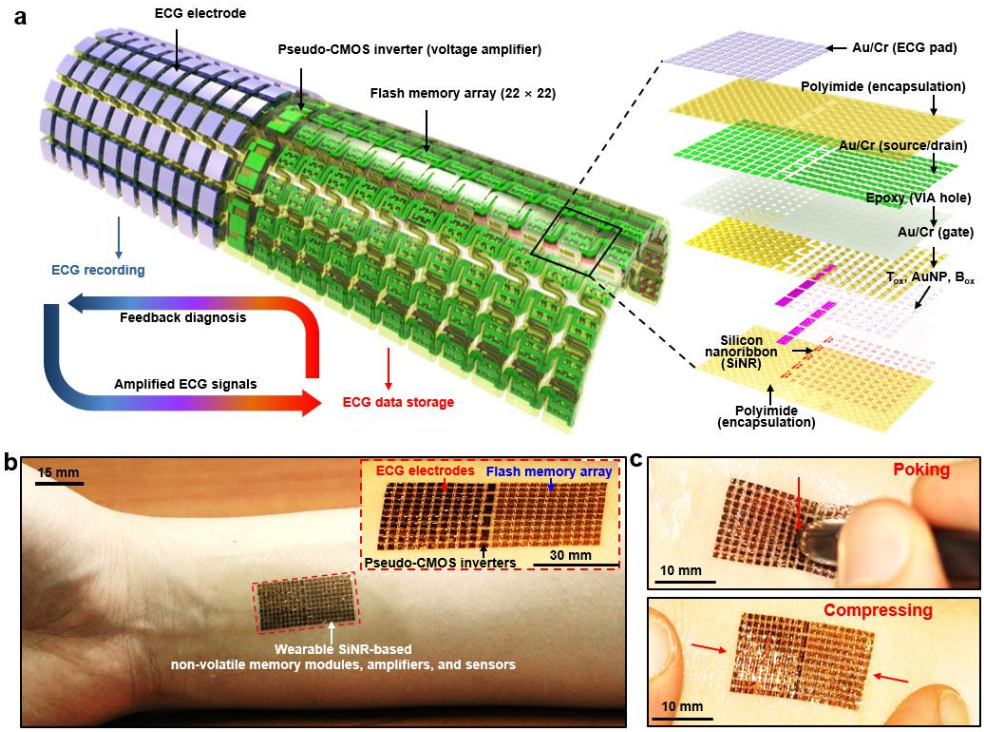

Figure 3.3. Demonstration system composed of ECG electrodes, amplifiers, and memory array. a, Schematic of the demonstration system and its exploded view showing layered structures. **b,** Fabricated demonstration system applied on human skin. **c,** Magnified view showing that the demonstration system in various deformed modes such as poking and compressing.

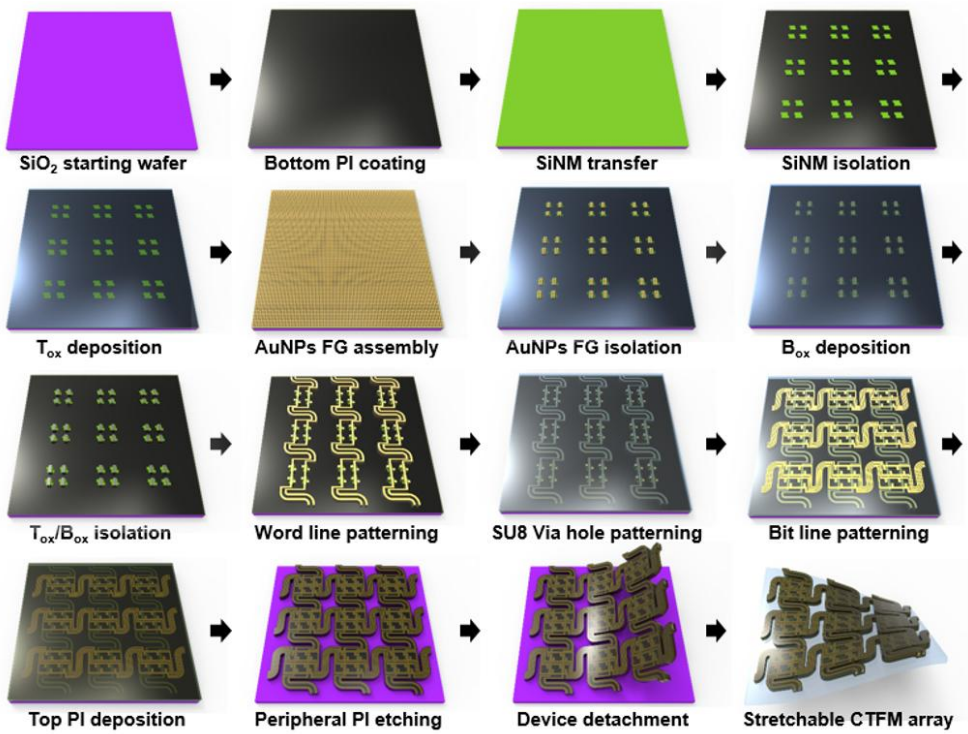

Figure 3.4. Fabrication process of CTFM array. Schematic images showing the fabrication process of the stretchable CTFM array.

3.3.3. Uniformity of large-area AuNP monolayer assembled by LB method

Figure 3.5a shows a transmission electron microscopy (TEM) image and magnified views (insets) of the highly uniform and closely packed AuNP monolayer assembled by the LB method. Each AuNP is electrically isolated (minimum spacing: 2 nm) by oleylamine capping ligands, as shown in the inset. This isolated structure prevents trapped charges from leaking out. The TEM images confirm the high uniformity (in terms of the particle size, shape, spacing, and distribution) of AuNPs. To validate the macroscale uniformity, 22 × 22 doped SiNMs where T_{ox} is deposited are formed on the polyimide (PI) substrate (Figure 3.5b, left; T_{ox}/SiNM/PI vertical structure, inset), and an AuNP monolayer are assembled on it by the LB method (Figure 3.5b, right; AuNPs/T_{ox}/SiNM/PI vertical structure, inset). The AFM images (Figure 3.5c) are collected from the region indicated by red box in the right frame of Figure 3.5b). The high macroscale uniformity of the AuNPs facilitates highly uniform cell-to-cell performance in CTFMs.

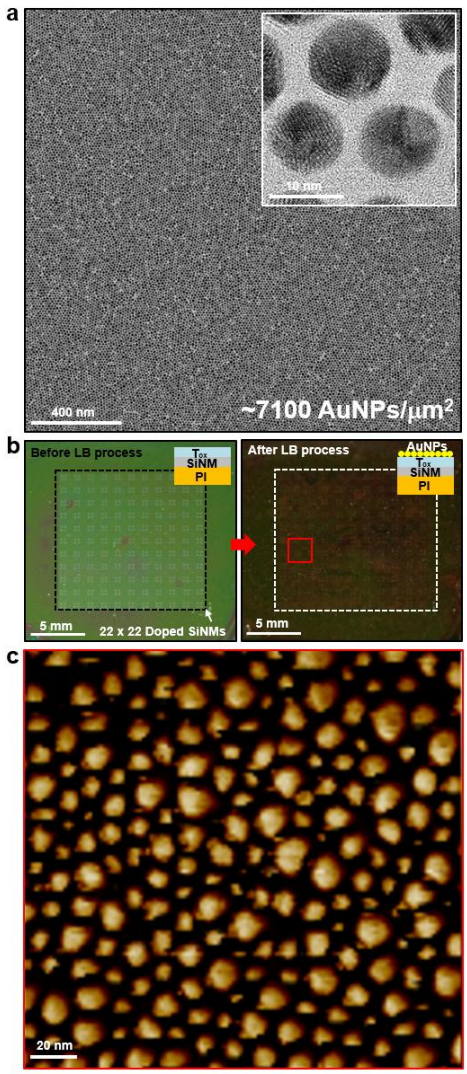

Figure 3.5. AuNPs assembled using LB method. a, TEM images of AuNPs assembled by the LB method. The insets show magnified TEM images. **b,** Photographs of before (left) and after (right) LB assembly of AuNPs on T_{ox}. **c,** AFM image of AuNPs assembled by the LB method at the region indicated with red box in b.

3.3.4. Material characterization of CTFM

To achieve large data storage capacity, multiple CTFM arrays can be stacked (Figure 3.6a, cross-sectional TEM image of three stacked layers) in a manner similar to that in multichip packaging techniques. The magnified view of the red-boxed region in Figure 3.6a shows the layer information of a single device and uniformly integrated AuNPs (Figure 3.6b). Spherical morphology of AuNPs is well maintained even after the fabrication. High-temperature processes are avoided to prevent the aggregation of AuNPs (Figure 3.7).

A scanning TEM (STEM) image and quantitative material analysis results are obtained by energy-dispersive X-ray spectroscopy analysis (EDS; Figure 3.6c). The EDS profile shows the material composition and thickness of each layer along the scanned line (yellow arrow). A thin layer of AlO_x/SiO_x (T_{ox}) formed by plasma-enhanced atomic layer deposition (PEALD) and assembled AuNPs is identified. The EDS results obtained by two-dimensional scanning provides the spatial distribution of specific elements, including Au, Al, and Si, in the cross section of the CTFM (Figure 3.8).

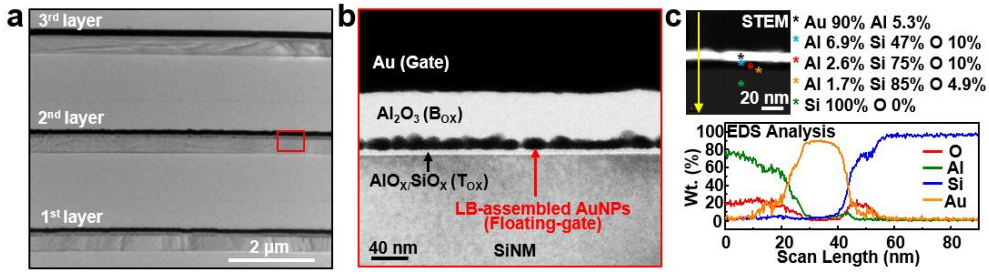

Figure 3.6. Material characterization. **a,** TEM image of the three-layer stacked CTFM. **b,** detailed cross-sectional structure of the CTFM and uniform AuNP FG embedded in dielectrics. **c,** STEM image showing cross-sectional structure of the CTFM (top left), quantitative EDS analysis results obtained at the spots marked in the STEM image with colored asterisks (top right), and EDS analysis results obtained along the yellow arrow shown in the STEM image (bottom).

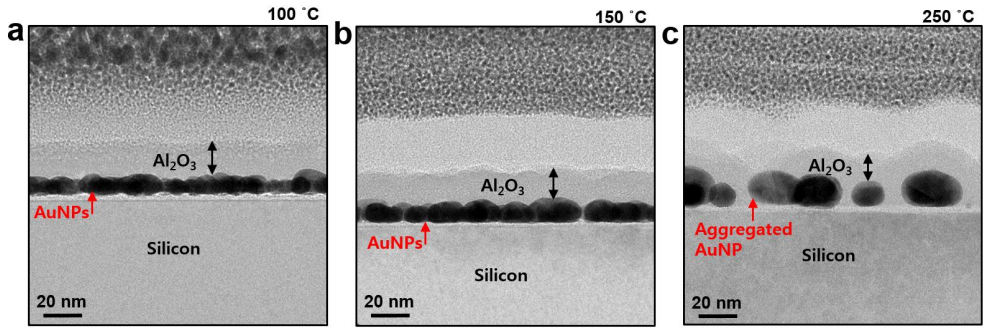

Figure 3.7. TEM images of AuNP FG assembled by LB method after the B_{ox} deposition using PEALD process. a-c, TEM images of AuNP FG assembled by LB method after the B_{ox} deposition using PEALD process under **a,** 100 °C, **b,** 150 °C, and **c,** 250 °C.

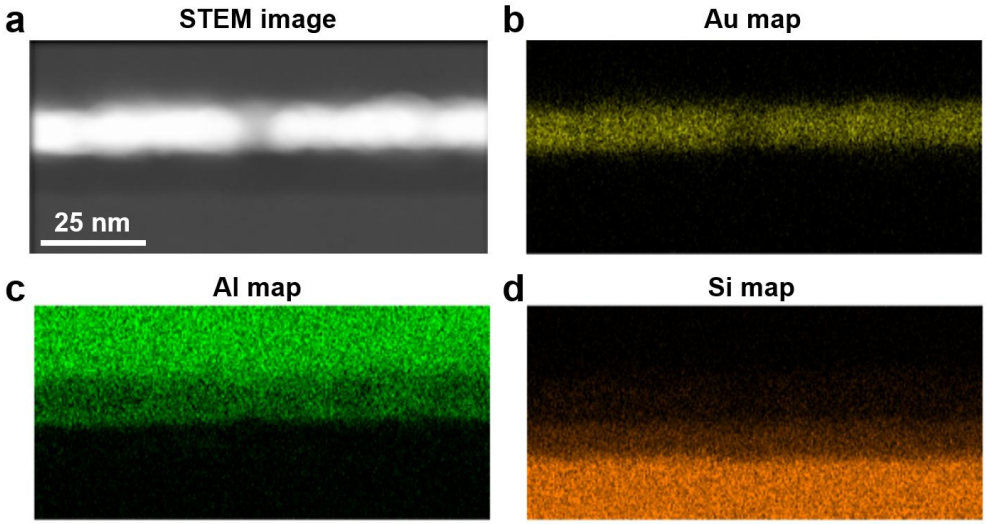

Figure 3.8. TEM-EDS 2D analysis of AuNPs embedded in a FG cell. a, Cross-sectional scanning TEM (STEM) image of a FG cell containing a AuNP FG. **b-c,** EDS analysis images obtained by two-dimensional scanning. Yellow, green, and orange colors represent different materials of **b,** Au, **c,** Al, and **d,** Si, respectively.

3.3.5. Electrical characterization of AuNP FG

Schematic diagrams showing the band structures of the memory capacitor (metal-insulator-FG-insulator-semiconductor structure) under flat-band and positive/negative bias conditions are illustrated in Figure 3.9. The positive/negative bias corresponds to the program/erase (PGM/ERS) operation. Electrons are trapped in the AuNP FG by tunneling through the T_{ox} during PGM operation (Figure 3.9b, left), whereas trapped electrons can be removed by tunneling back to the Si during ERS operation (Figure 3.9b, right). The tunneling mechanism follows Fowler-Nordheim (F-N) tunneling.[4] In case of the CTFM composed of Si, SiO_2 T_{ox}, and poly Si FG, the tunneling current density is given by

$$J = \alpha E_{inj}^2 exp\left(-\frac{\beta}{E_{inj}}\right) \qquad \alpha = \frac{q^3}{8\pi h \emptyset_b}\frac{m}{m^*}, \quad \beta = 4\sqrt{2m^*}\frac{\emptyset_b^{3/2}}{3\hbar q}$$

where h, $\emptyset_b$, q, m, m^*, $\hbar$, and E_{inj} denote Planck's constant, energy barrier at the injecting surface, charge of a single electron, mass of a free electron, effective mass of an electron, h over 2π, and applied electric field, respectively. The tunneling current density is exponentially dependent on the applied electric field, E_{inj}. This relationship can be indirectly verified by applying different PGM/ERS voltages and comparing the threshold voltage shifts.

To verify the spatially differentiated/patterned charge confinement in the AuNP FG assembled by the LB method, different amounts of charges are injected at different regions in the FG cell through an AFM

tip utilized as a top electrode (Figure 3.10). EFM images of the FG cell show that the different amounts of charges are well confined in specific areas of the AuNP FG (Figure 3.10b). Their spatial charge distribution is well maintained even after 24 h and 72 h from the moment of initial charge injection by virtue of the minimal lateral spreading of the trapped charges in the AuNP based FG cell.

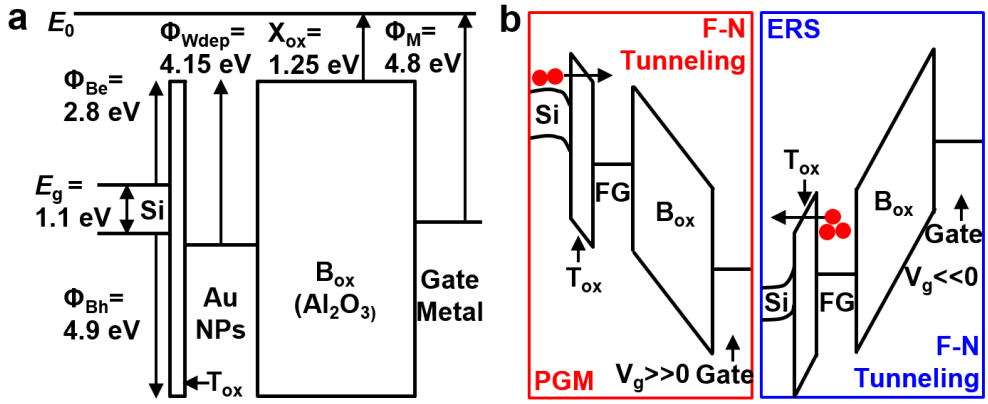

Figure 3.9. Energy band diagrams of CTFM under three representative bias conditions. a, flat-band condition. **b,** PGM and ERS operation.

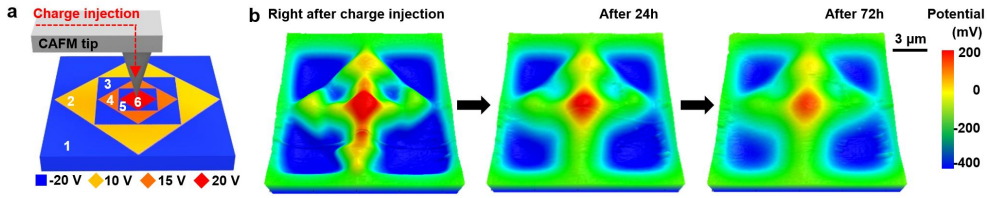

Figure 3.10. 2D multi-level charge injection and retention property. a, Schematic of experimental setup for two-dimensional injection of different amount of charges into the AuNP FG assembled by the LB method. **b,** EFM image of the FG cell containing different amount of charges at different locations by two-dimensional injection of charges.

3.3.6. Electrical and mechanical characterization of wearable CTFM

The electrical characteristics of the stretchable CTFM array are evaluated by addressing multiplexed memory pixels individually. Figure 3.11a shows the transfer characteristics of a CTFM under multilevel cell (MLC) operations. As the applied bias in PGM/ERS increases, the threshold voltage (V_{th}; indicated by dashed lines in Figure 3.11a) shifts right/left, respectively. The biasing time of the PGM/ERS also affects the V_{th} shift (Figure 3.11b-d). The ERS requires larger applied voltage and/or longer biasing time than the PGM for the same amount of V_{th} shift. This is because the work function of AuNPs is larger than the electron affinity of Si, which requires larger band bending to remove electrons from the FG than to inject them to the FG (Figure 3.9). Figure 3.12a shows stable charge retention at each voltage level up to 10^3 s. Two states are chosen to observe longer retention (10^5 s; Figure 3.12b). Further studies on development of the defect-free T_{ox} that can be formed using low temperature processes would improve the retention time for long term data storage. The charge storage of the CTFM is reliable even after up to 10^4 PGM/ERS cycles (Figure 3.13).

Figure 3.14a shows a schematic diagram of the NOR-type CTFM array configuration. The electrical disturbances between selected (S; red dashed box) and peripheral (P; blue dashed box) memory pixels are investigated. When the memory pixel S is at programmed state, co-applied inhibition biases on the word line minimize the disturbances on the

memory pixel S during the PGM/ERS operation of the peripheral memory pixels (Figure 3.14b). Without the inhibition voltages, selected memory pixel (S) might be vulnerable to the disturbance induced by PGM/ERS operation of the peripheral memory pixel (P) (Figure 3.14c) The reliable operation of the CTFM array is confirmed by the cumulative probability data of the sampled pixels (Figure 3.14d). A slight V_{th} distribution may exist owing to the difference in interconnection resistance between memory pixels close and far from the voltage source.

The mechanical reliability of CTFMs is confirmed through cyclic stretching tests (Figure 3.15a and b, top frames). The finite element analysis (FEA) of the induced strain distribution shows that memory pixels (red dashed boxes) under ~20% stretching have negligible strains (~0.2%; *cf.*, fracture strain of Si: ~1%,[43] Al_2O_3: ~1%[44] (Figure 3.15a and b, bottom frames). Serpentine interconnections accommodate most of the applied strain. The PGM/ERS of CTFMs is conducted under various applied strains (Figure 3.15c) and after repetitive stretching up to 1,200 cycles (Figure 3.15d; ~20% strain). In both cases, the performance degradation is negligible. Considering that the allowed strain of the human epidermis is ~20%,[35] the current level of mechanical reliability is suitable for many wearable applications.

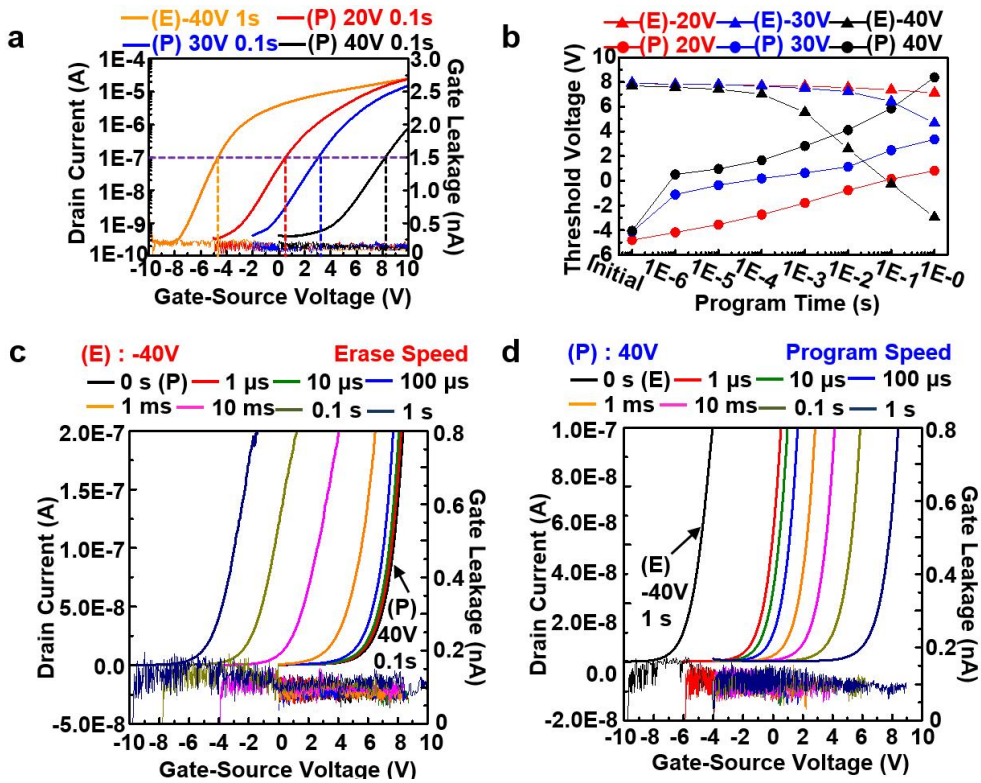

Figure 3.11. Transfer characteristics of the CTFM. a, Transfer characteristics of a CTFM pixel after PGM/ERS operation with different voltages, showing four states. **b,** PGM/ERS speed characteristics of the CTFM pixel with different operation voltages. **c,** Drain current of a CTFM pixel as a function of gate-source voltage with different pulse widths and fixed ERS voltages (-40 V). **d,** Drain current of the CTFM pixel as a function of gate-source voltage with different pulse widths and fixed PGM voltages (40 V).

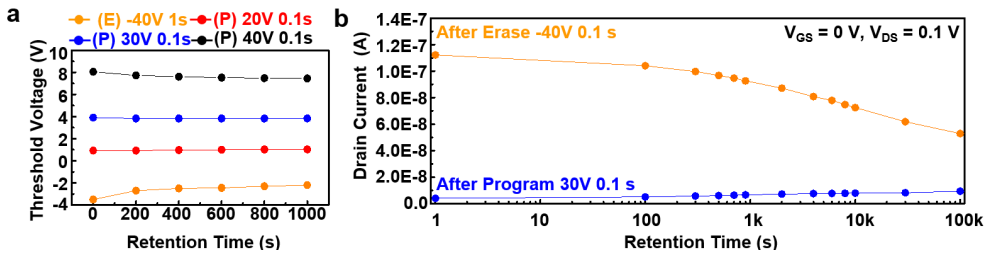

Figure 3.12. Retention property of the CTFM. a, Retention characteristics of the CTFM pixel for each possible state. **b,** Retention characteristics of programmed state (30V, 0.1s) and erased state (-40V, 0.1s). Drain current levels of each state are read at V_{GS} = 0 V and V_{DS} = 0.1 V.

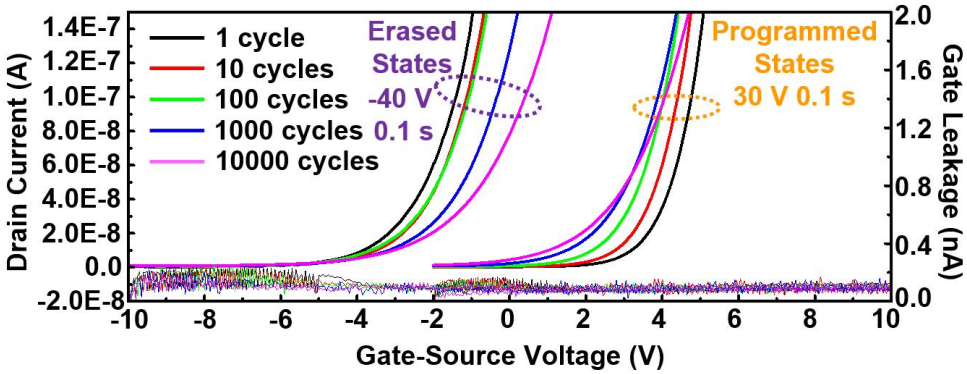

Figure 3.13. Changes in the transfer curves of a CTFM pixel after repetitive PGM and ERS cycles. PGM, 30 V; ERS, -40 V; pulse duration of 0.1 s.

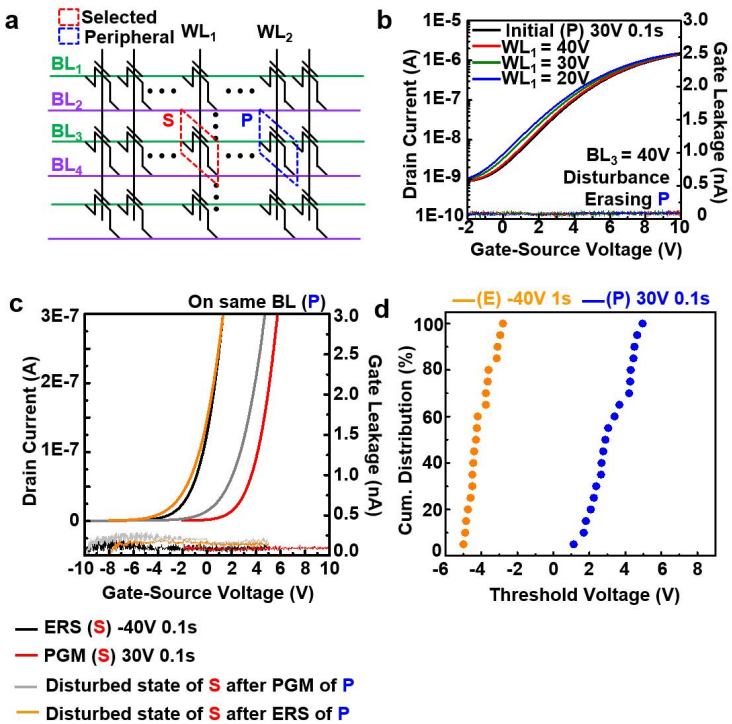

Figure 3.14. Electrical characteristics of CTFM array. a, Schematic of the CTFM array in NOR configuration. Dashed box indicates a selected memory pixel (red) and a manipulated peripheral pixel (blue) for a disturbance test verifying the degree of influence on the electrical state of the selected pixel, induced by manipulation of the peripheral pixels. **b,** Transfer curves measured from the programmed memory pixel (S) of initial condition and inhibited condition in which the ERS bias on BL_3 for manipulating the peripheral CTFM pixel (P) and different inhibition biases on WL_1 are applied simultaneously. **c,** Changes in transfer curves of the selected pixel after programming or erasing peripheral memory pixel (P) without inhibition voltage. **d,** Cumulative probability data of the selected state obtained from 20 memory pixels.

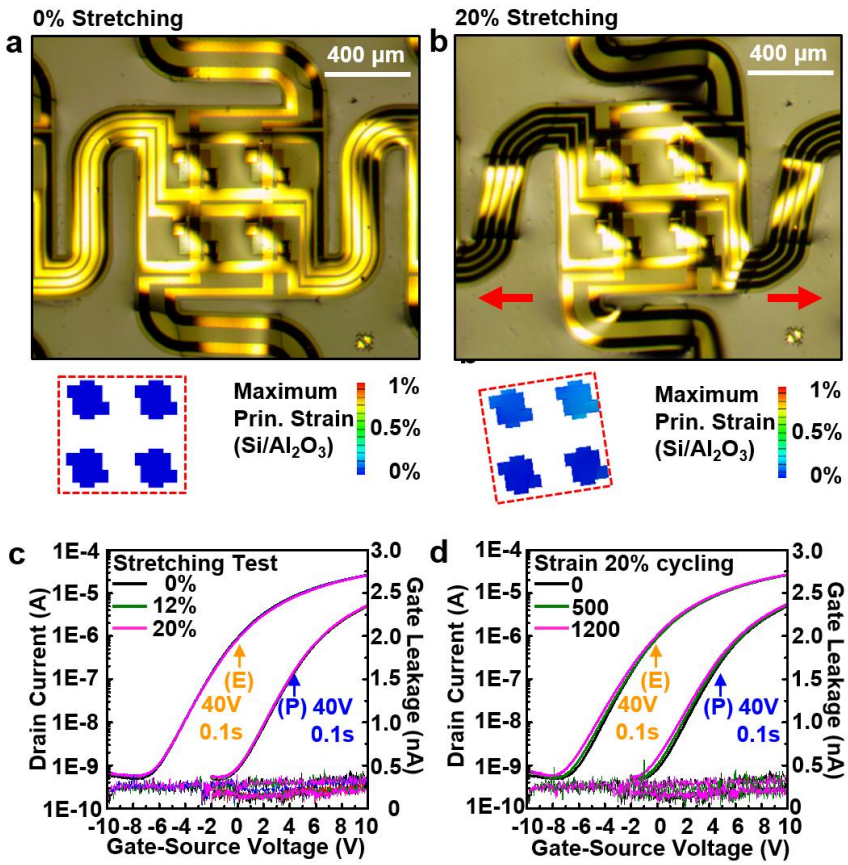

Figure 3.15. Effects of mechanical deformation on the performance of the CTFM. a-b, Photograph of **a,** not stretched and **b,** stretched (20%) CTFM array and corresponding FEA results. **c-d,** Transfer curves of the CTFM pixel after conducting PGM/ERS operation under **c,** various applied strains and **d,** various stretched cycles of 20% strain.

3.3.7. Electrical and mechanical characterization of wearable Si amplifier

To acquire the heart rate, a pseudo-CMOS inverter composed of four n-type MOS (nMOS) transistors (Figure 3.16a) is used to amplify ECG signals. The amplifier's output voltage (V_{OUT}) with respect to the input voltage (V_{IN}) under various bias conditions (V_{SS}, V_{DD}) is plotted in Figure 3.16b and c (solid and dashed line for experiment and simulation, respectively). The simulations are based on data of a single transistor (Figure 3.17a and b). The design parameters of the pseudo-CMOS inverter and its characteristics such as the noise margins are shown in Figure 3.18 and Table 3.1. The amplifier gain increases with V_{SS} (Figure 3.19a). The maximum amplification gain is ~200 (inset) at V_{IN} of 3.17 V (V_M) and V_{SS} of 12 V. Figure 3.19b shows the input sinusoidal signal (40 mV_{p-p}) and filtered output signal (~4 V_{p-p}) amplified by the wearable Si pseudo-CMOS inverter. The lower effective gain (~100) than the maximum is caused by the deviation of the input signal from V_M. The decreased deviation of the input voltage from V_M results in higher effective gain (Figure 3.19c). The pseudo-CMOS inverter amplifies the ECG signal (<4.5 mV_{p-p}) with effective gain of 100 or higher. The frequency response shows that high effective gain is maintained owing to the relatively low frequency of ECG signals (<5 Hz; Figure 3.19d).

To verify the mechanical reliability, the amplifier is electrically characterized under stretched conditions (Figure 3.20a and b, top frames). The FEA shows that ~20% applied strain induces negligible strain of

<0.2% in active regions (red dashed box; Figure 3.20a and b, bottom frames). The voltage transfer curves of the pseudo-CMOS inverter are obtained under various strains (0%–20%), in which negligible changes are observed (Figure 3.20c). Stretching tests up to 500 cycles are performed and only minimal shifts in the voltage transfer curve are observed (Figure 3.20d).

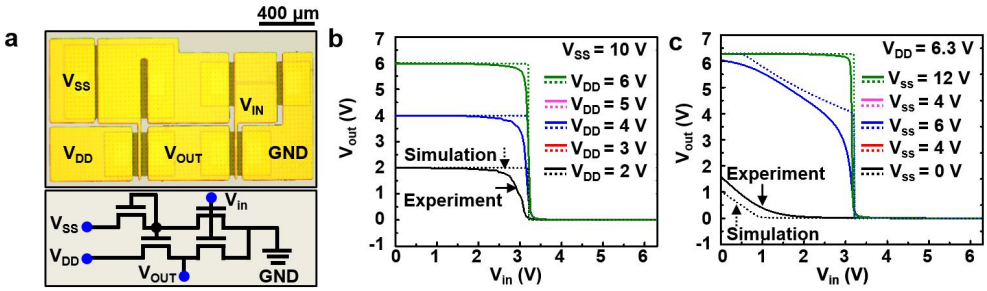

Figure 3.16. Electrical characteristics of the pseudo-CMOS inverter. a, Microscopic image of the pseudo-CMOS inverter (top) and schematic circuit diagram (bottom). **b-c,** Voltage transfer characteristic curves of the pseudo-CMOS inverter (dashed line: simulation results; solid line: experimental results) depending on **b,** various values of V_{DD} when V_{SS} is fixed to 10 V and **c,** various values of V_{SS} when V_{DD} is fixed to 6.3V.

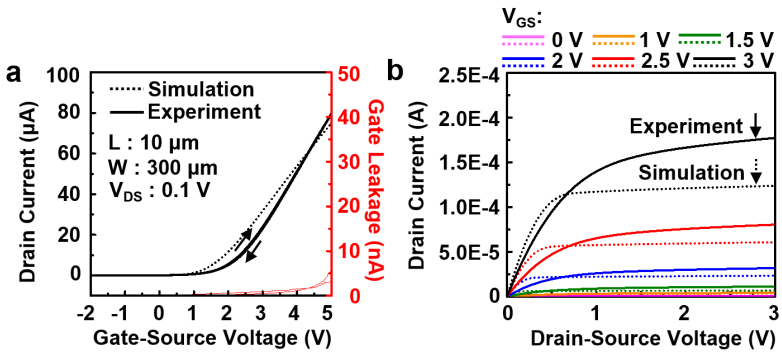

Figure 3.17. Electrical characteristics of the single transistor. a, Transfer curve of a transistor which forms a pseudo-CMOS inverter (solid line) and the simulation result (dashed line). **b,** Measured I_d-V_d curves of the transistor and the simulation results (dashed line).

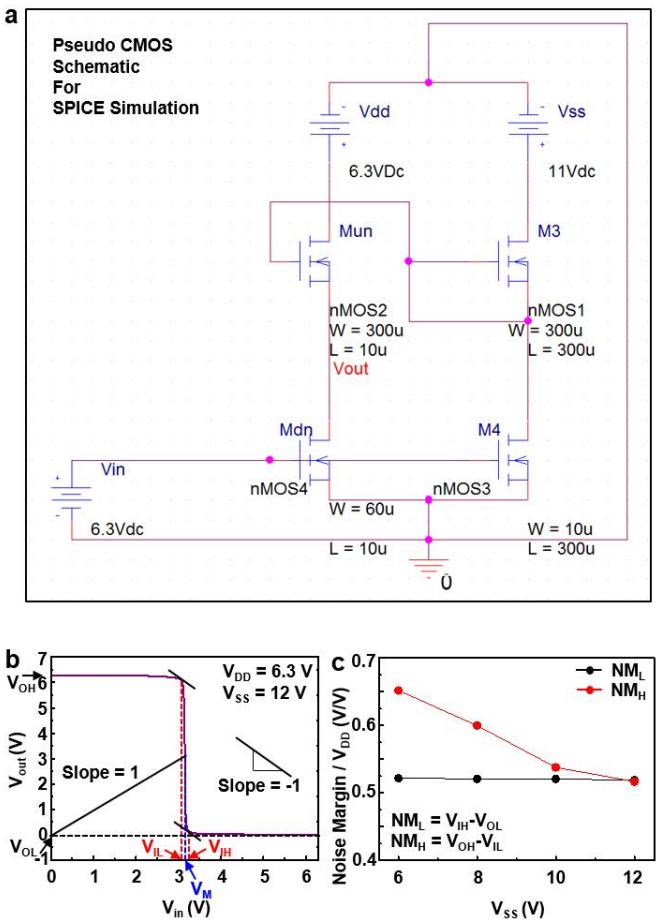

Figure 3.18. PSpice simulation and experimental results of the pseudo-CMOS inverter. a, PSpice schematic showing a circuit diagram of pseudo-CMOS inverter and its design parameters utilized for simulations. **b,** Characteristic curve of the pseudo-CMOS inverter. Several parameters (V_{OH} = voltage output high; V_{OL} = voltage output low; V_{IL} = voltage input low; V_{IH} = voltage input high; V_M = voltage midpoint) are indicated on the plot. **c,** Noise margins (NM_L = noise margin low; NM_H = noise margin high) of the pseudo-CMOS inverter as a function of V_{SS}.

Table 3.1. Noise margins of pseudo-CMOS inverter. Important voltages for calculating noise margins and the calculated noise margins according to V_{SS} when V_{DD} is fixed to 6.3 V.

V_{SS}	V_{IL}	V_{IH}	V_{OL}	V_{OH}	NM_L	NM_H	V_M
6	1.94	3.29	0.00	6.05	3.29	4.11	2.90
8	2.50	3.28	0.00	6.28	3.28	3.78	3.13
10	2.90	3.28	0.00	6.29	3.28	3.39	3.16
12	3.03	3.27	0.00	6.29	3.27	3.26	3.15

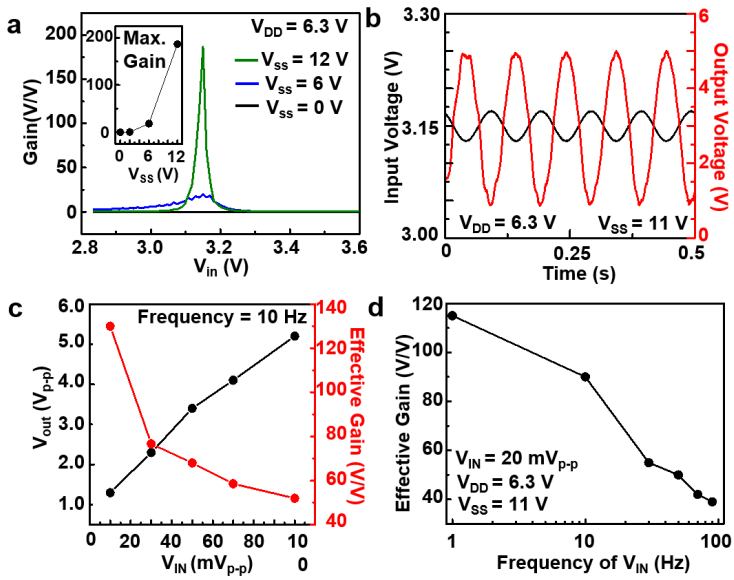

Figure 3.19. Maximum and effective gain of the pseudo-CMOS inverter. a, Signal gain of the inverter measured with respect to the input voltage (V_{IN}) with under various biasing conditions (V_{SS} when V_{DD} is fixed to 6.3 V). The inset shows the maximum gain with respect to V_{SS}. **b,** Sinusoidal input signal (black, 40 mV_{p-p}, 10 Hz) and output signal (red) amplified by the pseudo-CMOS inverter. **c,** Effective gain of the pseudo-CMOS inverter as a function of the amplitude of the sinusoidal input signal (10 Hz). **d,** Frequency response of the effective gain of the pseudo-CMOS inverter when the input signal is sinusoidal and its amplitude is 20 mV_{p-p}.

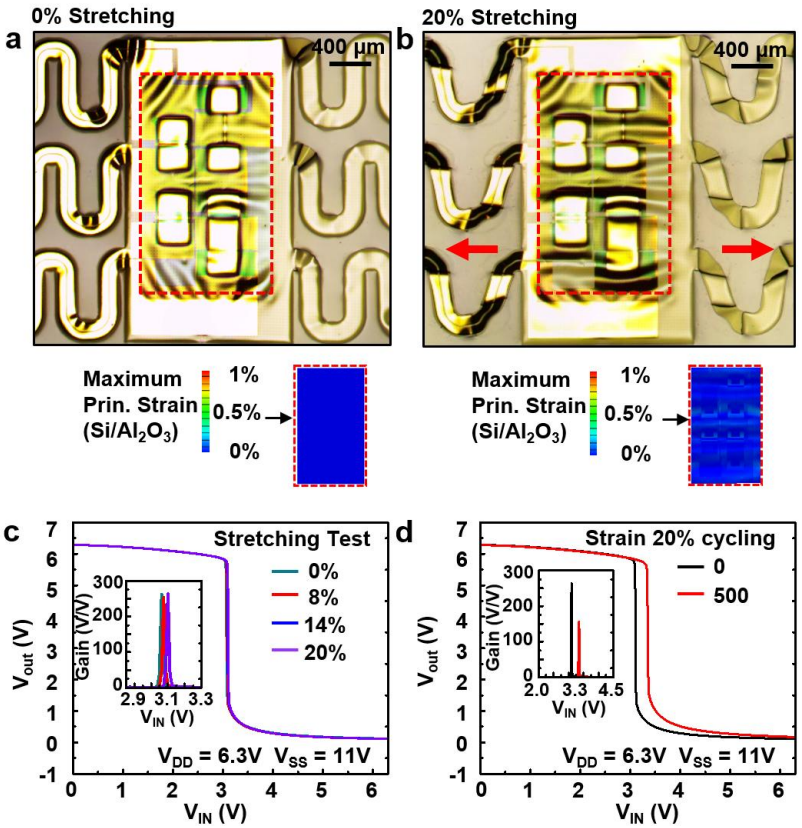

Figure 3.20. Stretching test of the pseudo-CMOS inverter and FEA results. **a-b,** Photographs of **a,** not stretched (0%) and **b,** stretched (20%) pseudo-CMOS inverter and corresponding FEA results showing distribution of maximum principle strain on the active region (red dotted box) of the pseudo-CMOS inverter **c-d,** Voltage transfer characteristics and corresponding gain (inset) of a pseudo-CMOS inverter measured under **c,** various strains and **d,** various stretched cycles of 20% strain.

3.3.8. Monitoring electrocardiograms using amplifiers and storage of heart rates in memory array

It is important to monitor the heart rate recovery to diagnose abnormal cardiovascular parasympathetic functions, as recovery is determined by the reactivated parasympathetic control that usually occurs within 30 s after the end of exercise.[45] In this regard, we demonstrate the storage of the heart rate recovery data recorded and amplified using wearable electrodes and amplifiers, respectively, for 200 s after exercise.

A Schematic of the sequential procedures comprising ECG signal acquisition, on-site amplification, heart rate measurement, and data storage/retrieval to/from the CTFM array is depicted in Figure 3.21a. The heart rate and elapsed time data are converted into 8-bit binary data and stored in the CTFM array (Figure 3.21b). The amplified ECG signals measured by wearable electrodes and commercial electrodes are shown in Figure 3.22a and b, respectively. There is no significant difference between these two. Although it is difficult to distinguish P, Q, and S features from the amplified ECG signals, the heart rate can be reliably extracted by detecting the relatively evident R peaks. For better signal quality, additional noise reduction filters and circuits can be integrated in the future work. The heart rate recovery of a volunteer is monitored using wearable electrodes and amplifiers (Figure 3.22c). Immediately after the exercise, the heart rate increased from 72 to 162 beats per minute (BPM) and then continuously decreased to 96 BPM (Figure 3.22c).

PGM/ERS biases are applied to the selected row of the CTFM array to store the heart rate recovery data shown in Figure 22c. The stored data in the CTFM array can be read easily after data storage; Figure 3.23a shows the data storage map. White boxes indicate erased memory pixels storing the binary number "0" and black boxes indicate programmed memory pixels storing the binary number "1". After 6 h, the stored data are read again, and the retrieved data is found to be exactly the same; this indicates the good retention property of the CTFM array (Figure 3.23b). The stored data contains the heart rate and elapsed time encoded in binary numbers; this data can be converted to decimal numbers to enable medical personnel to check the wearer's heart rate recovery history.

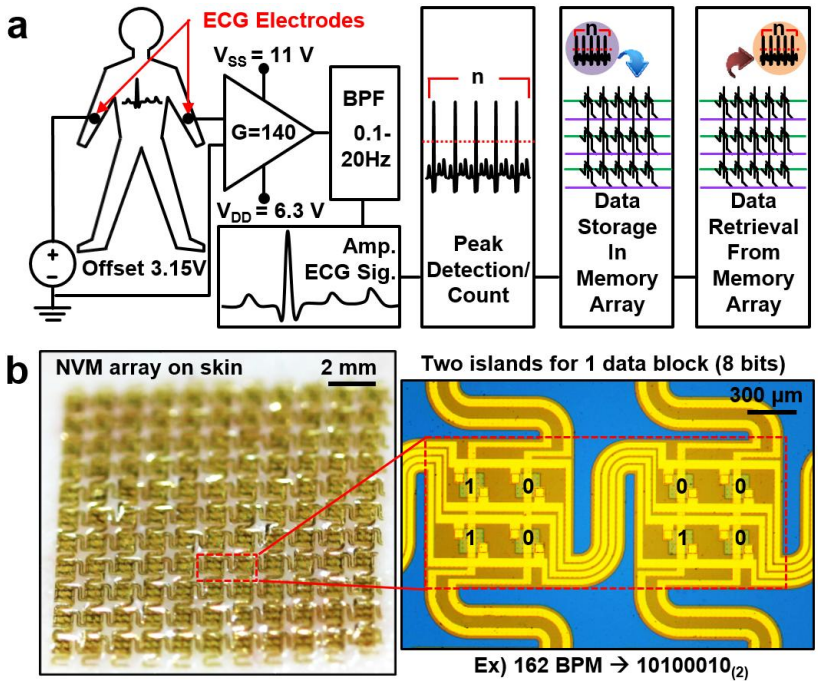

Figure 3.21. Demonstration procedures and data storage scheme. a, Diagram of overall demonstration process: ECG measurement, amplification, heart rate detection, and data storage and retrieval. **b,** Photograph of the wearable CTFM laminated on the skin (left) and enlarged view showing the scheme of data storage in the CTFM array (right).

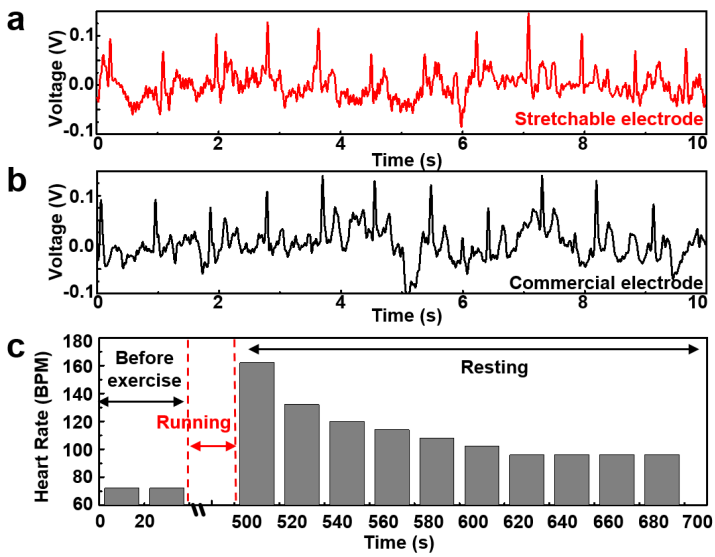

Figure 3.22. ECG signals measured using stretchable electrodes and commercial one, and heart beat data measured during exercise stress test. **a-b,** ECG signal acquired using **a,** fabricated stretchable electrodes and **b,** commercial electrodes. **c,** Measured temporal change of the resting heart rate before exercise and after exercise.

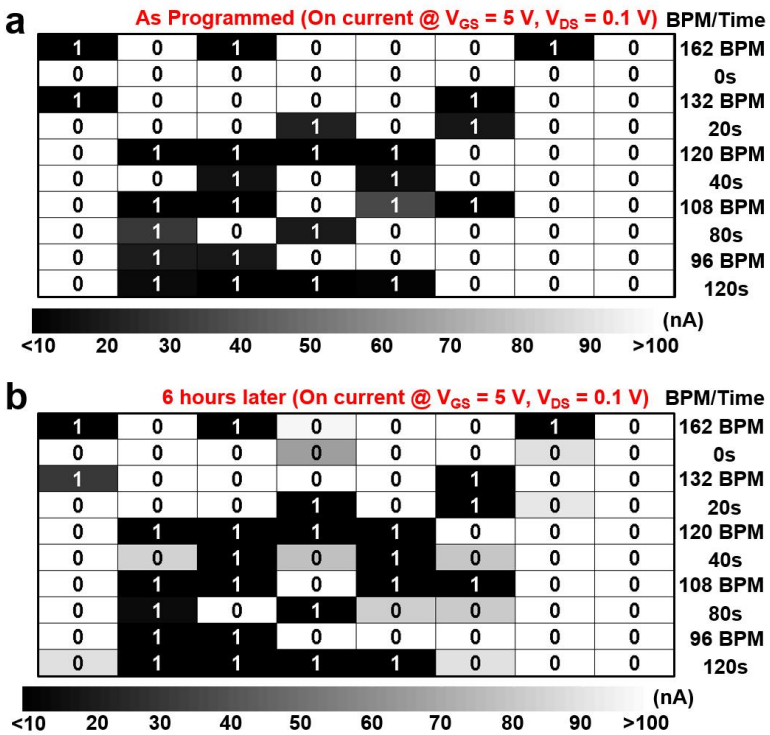

Figure 3.23. Storage of heartrate data to the CTFM memory array. a-b, Heart rate recovery data and corresponding elapsed time data retrieved from the CTFM array: **a,** immediately after data storage and **b,** 6 h after data storage.

3.4. Conclusion

Future wearable systems that pursue mobile healthcare monitoring and data analysis based on high performance bioelectronics should monolithically integrate various stretchable electronic components, such as sensors, amplifiers, and memory modules. However, there have been limited studies for system-level demonstrations using high performance stretchable non-volatile memory and related electronic devices.

In this work, we demonstrated reliable data storage of heart rates, which are obtained from ECG signals amplified by co-located stretchable Si amplifiers, to the wearable nanocrystal memory. The stretchable, high-density, and ultrathin memory array with the enhanced charge storage capability has great potential for various wearable electronics applications. Appropriate materials and design strategies using SiNM electronics as well as uniformly assembled AuNPs enable the realization of a wearable high-performance nonvolatile memory array. In particular, the large-area uniform assembly of AuNPs forms an efficient FG, which enhances the data storage capacity, retention property, and performance uniformity in the memory array. To validate superior charge confinement capability of AuNPs, the modified AFM technique which visualizes confined charges with nanoscale resolution has been newly developed.

The advances of characterization and fabrication technologies reported in this paper will be an important stepping stone that paves the way to a fully integrated wearable system composed of the stretchable nanocrystal

FG memory and other stretchable Si electronics toward mobile and personalized health-monitoring.

References

1. Bez, R., Camerlenghi, E., Modelli, A., Visconti, A. Introduction to flash memory. *Proc. IEEE* **91**, 489-502 (2003).
2. Chen, F., Koufaty, D. A., Zhang, X. Understanding intrinsic characteristics and system implications of flash memory based solid state drives. *Sigmetrics Perform. Eval. Rev.* **37**, 181-192 (2009).
3. Yoon, J. H., Kim, K. M., Song, S. J., Seok, J. Y., Yoon, K. J., Kwon, D. E., Park, T. H., Kwon, Y. J., Shao, X., Hwang, C. S. $Pt/Ta_2O_5/HfO_{2-x}/Ti$ resistive switching memory competing with multilevel NAND flash. *Adv. Mater.* **27**, 3811-3816 (2015).
4. Blauwe, J. D. Nanocrystal nonvolatile memory devices. *IEEE Trans. Nanotechnol.* **1**, 72-77 (2002).
5. Tu, C. H., Chang, T. C., Liu, P. T., Liu, H. C., Weng, C. F., Shy, J. H., Tseng, B. H., Tseng, T. Y., Sze, S. M., Chang, C. Y. A fabrication of germanium nanocrystal embedded in silicon-oxygen-nitride layer. *Electrochem. Solid-state Lett.* **9**, G358-G360 (2006).
6. Lee, J. S. Recent progress in gold nanoparticle-based non-volatile memory devices. *Gold Bull.* **43**, 189-199 (2010).
7. Wang, S., Pu, J., Chan, D. S. H., Cho, B. J., Loh, K. P. Wide memory window in graphene oxide charge storage nodes. *Appl. Phys. Lett.* **96**, 143109 (2010).
8. Zhou, Y., Han, S. T., Yan, Y., Huang, L. B., Zhou, L., Huang, J., Roy, V. a. L. Solution processed molecular floating gate for flexible flash memories. *Sci. Rep.* **3**, 3093 (2013).

9. Han, S. T., Zhou, Y., Wang, C. D., He, L. F., Zhang, W. J., Roy, V. a. L. Layer-by-layer-assembled reduced graphene oxide/gold nanoparticle hybrid double-floating-gate structure for low-voltage flexible flash memory. *Adv. Mater.* **25**, 872-877 (2013).

10. Kim, C., Song, J. M., Lee, J. S., Lee, M. J. All-solution-processed nonvolatile flexible nano-floating gate memory devices. *Nanotechnology* **25**, 014016 (2014).

11. Han, S. T., Zhou, Y., Xu, Z. X., Huang, L. B., Yang, X. B., Roy, V. a. L. Microcontact printing of ultrahigh density gold nanoparticle monolayer for flexible flash memories. *Adv. Mater.* **24**, 3556-3561 (2012).

12. Kim, S. J., Lee, J. S. Flexible organic transistor memory devices. *Nano Lett.* **10**, 2884-2890 (2010).

13. Lee, J. S., Cho, J., Lee, C., Kim, I., Park, J., Kim, Y. M., Shin, H., Lee, J., Caruso, F. Layer-by-layer assembled charge-trap memory devices with adjustable electronic properties. *Nat. Nanotech.* **2**, 790-795 (2007).

14. Liu, Z. T., Lee, C., Narayanan, V., Pei, G., Kan, E. C. Metal nanocrystal memories - Part I: Device design and fabrication. *IEEE Trans. Electron Devices* **49**, 1606-1613 (2002).

15. Liu, Z. T., Lee, C., Narayanan, V., Pei, G., Kan, E. C. Metal nanocrystal memories - Part II: Electrical characteristics. *IEEE Trans. Electron Devices* **49**, 1614-1622 (2002).

16. Lee, C., Gorur-Seetharam, A., Kan, E. C. Operational and reliability comparison of discrete-storage nonvolatile memories:

advantages of single- and double-layer metal nanocrystals, *IEEE Int. Electron Devices Meet.*, 22.6.1-22.6.4 (2003).

17. Talapin, D. V., Lee, J. S., Kovalenko, M. V., Shevchenko, E. V. Prospects of colloidal nanocrystals for electronic and optoelectronic applications. *Chem. Rev.* **110**, 389-458 (2010).

18. Lim, S., Son, D., Kim, J., Lee, Y. B., Song, J. K., Choi, S., Lee, D. J., Kim, J. H., Lee, M., Hyeon, T., Kim, D. H. Transparent and stretchable interactive human machine interface based on patterned graphene heterostructures. *Adv. Funct. Mater.* **25**, 375-383 (2015).

19. Takei, K., Takahashi, T., Ho, J. C., Ko, H., Gillies, A. G., Leu, P. W., Fearing, R. S., Javey, A. Nanowire active-matrix circuitry for low-voltage macroscale artificial skin. *Nat. Mater.* **9**, 821-826 (2010).

20. Park, J., Lee, Y., Hong, J., Ha, M., Jung, Y. D., Lim, H., Kim, S. Y., Ko, H. Giant tunneling piezoresistance of composite elastomers with interlocked microdome arrays for ultrasensitive and multimodal electronic skins. *ACS Nano* **8**, 4689-4697 (2014).

21. Park, J., Lee, Y., Hong, J., Lee, Y., Ha, M., Jung, Y., Lim, H., Kim, S. Y., Ko, H. Tactile-direction-sensitive and stretchable electronic skins based on human-skin-inspired interlocked microstructures. *ACS Nano* **8**, 12020-12029 (2014).

22. Lipomi, D. J., Vosgueritchian, M., Tee, B. C. K., Hellstrom, S. L., Lee, J. A., Fox, C. H., Bao, Z. N. Skin-like pressure and strain sensors based on transparent elastic films of carbon nanotubes. *Nat. Nanotech.* **6**, 788-792 (2011).

23. Tee, B. C. K., Wang, C., Allen, R., Bao, Z. N. An electrically and mechanically self-healing composite with pressure- and flexion-sensitive properties for electronic skin applications. *Nat. Nanotech.* **7**, 825-832 (2012).

24. Schwartz, G., Tee, B. C. K., Mei, J. G., Appleton, A. L., Kim, D. H., Wang, H. L., Bao, Z. N. Flexible polymer transistors with high pressure sensitivity for application in electronic skin and health monitoring. *Nat. Commun.* **4**, 1859 (2013).

25. Sekitani, T., Zschieschang, U., Klauk, H., Someya, T. Flexible organic transistors and circuits with extreme bending stability. *Nat. Mater.* **9**, 1015-1022 (2010).

26. Kaltenbrunner, M., Sekitani, T., Reeder, J., Yokota, T., Kuribara, K., Tokuhara, T., Drack, M., Schwodiauer, R., Graz, I., Bauer-Gogonea, S., Bauer, S., Someya, T. An ultra-lightweight design for imperceptible plastic electronics. *Nature* **499**, 458-463 (2013).

27. Wang, C., Hwang, D., Yu, Z. B., Takei, K., Park, J., Chen, T., Ma, B. W., Javey, A. User-interactive electronic skin for instantaneous pressure visualization. *Nat. Mater.* **12**, 899-904 (2013).

28. Park, S. I., Xiong, Y. J., Kim, R. H., Elvikis, P., Meitl, M., Kim, D. H., Wu, J., Yoon, J., Yu, C. J., Liu, Z. J., Huang, Y. G., Hwang, K., Ferreira, P., Li, X. L., Choquette, K., Rogers, J. A. Printed assemblies of inorganic light-emitting diodes for deformable and semitransparent displays. *Science* **325**, 977-981 (2009).

29. White, M. S., Kaltenbrunner, M., Glowacki, E. D., Gutnichenko, K., Kettlgruber, G., Graz, I., Aazou, S., Ulbricht, C., Egbe, D. a. M., Miron, M. C., Major, Z., Scharber, M. C., Sekitani, T., Someya, T., Bauer, S., Sariciftci, N. S. Ultrathin, highly flexible and stretchable PLEDs. *Nat. Photon.* **7**, 811-816 (2013).

30. Choi, M. K., Yang, J., Kang, K., Kim, D. C., Choi, C., Park, C., Kim, S. J., Chae, S. I., Kim, T. H., Kim, J. H., Hyeon, T., Kim, D. H. Wearable red-green-blue quantum dot light-emitting diode array using high-resolution intaglio transfer printing. *Nat. Commun.* **6**, 7149 (2015).

31. Kim, S., Jeong, H. Y., Kim, S. K., Choi, S. Y., Lee, K. J. Flexible memristive memory array on plastic substrates. *Nano Lett.* **11**, 5438-5442 (2011).

32. Ji, Y., Cho, B., Song, S., Kim, T. W., Choe, M., Kahng, Y. H., Lee, T. Stable switching characteristics of organic nonvolatile memory on a bent flexible substrate. *Adv. Mater.* **22**, 3071-3075 (2010).

33. Ji, Y., Zeigler, D. F., Lee, D. S., Choi, H., Jen, A. K. Y., Ko, H. C., Kim, T. W. Flexible and twistable non-volatile memory cell array with all-organic one diode-one resistor architecture. *Nat. Commun.* **4**, 2707 (2013).

34. Son, D., Lee, J., Qiao, S., Ghaffari, R., Kim, J., Lee, J. E., Song, C., Kim, S. J., Lee, D. J., Jun, S. W., Yang, S., Park, M., Shin, J., Do, K., Lee, M., Kang, K., Hwang, C. S., Lu, N. S., Hyeon, T., Kim, D. H. Multifunctional wearable devices for diagnosis and therapy of movement disorders. *Nat. Nanotech.* **9**, 397-404 (2014).

35. Kim, D. H., Lu, N. S., Ma, R., Kim, Y. S., Kim, R. H., Wang, S. D., Wu, J., Won, S. M., Tao, H., Islam, A., Yu, K. J., Kim, T. I., Chowdhury, R., Ying, M., Xu, L. Z., Li, M., Chung, H. J., Keum, H., Mccormick, M., Liu, P., Zhang, Y. W., Omenetto, F. G., Huang, Y. G., Coleman, T., Rogers, J. A. Epidermal electronics. *Science* **333**, 838-843 (2011).

36. Webb, R. C., Bonifas, A. P., Behnaz, A., Zhang, Y. H., Yu, K. J., Cheng, H. Y., Shi, M. X., Bian, Z. G., Liu, Z. J., Kim, Y. S., Yeo, W. H., Park, J. S., Song, J. Z., Li, Y. H., Huang, Y. G., Gorbach, A. M., Rogers, J. A. Ultrathin conformal devices for precise and continuous thermal characterization of human skin. *Nat. Mater.* **12**, 938-944 (2013).

37. Son, D., Koo, J. H., Song, J. K., Kim, J., Lee, M., Shim, H. J., Park, M., Lee, M., Kim, J. H., Kim, D. H. Stretchable carbon nanotube charge-trap floating-gate memory and logic devices for wearable electronics. *ACS Nano* **9**, 5585-5593 (2015).

38. Kim, J., Lee, M., Shim, H. J., Ghaffari, R., Cho, H. R., Son, D., Jung, Y. H., Soh, M., Choi, C., Jung, S., Chu, K., Jeon, D., Lee, S. T., Kim, J. H., Choi, S. H., Hyeon, T., Kim, D. H. Stretchable silicon nanoribbon electronics for skin prosthesis. *Nat. Commun.*, 5747 (2014).

39. Khang, D. Y., Jiang, H. Q., Huang, Y., Rogers, J. A. A stretchable form of single-crystal silicon for high-performance electronics on rubber substrates. *Science* **311**, 208-212 (2006).

40. Xu, L. Z., Gutbrod, S. R., Bonifas, A. P., Su, Y. W., Sulkin, M. S., Lu, N. S., Chung, H. J., Jang, K. I., Liu, Z. J., Ying, M., Lu, C., Webb, R. C., Kim, J. S., Laughner, J. I., Cheng, H. Y.,

Liu, Y. H., Ameen, A., Jeong, J. W., Kim, G. T., Huang, Y. G., Efimov, I. R., Rogers, J. A. 3D multifunctional integumentary membranes for spatiotemporal cardiac measurements and stimulation across the entire epicardium. *Nat. Commun.* **5**, 3329 (2014).

41. Kim, D. H., Ahn, J. H., Choi, W. M., Kim, H. S., Kim, T. H., Song, J. Z., Huang, Y. G. Y., Liu, Z. J., Lu, C., Rogers, J. A. Stretchable and foldable silicon integrated circuits. *Science* **320**, 507-511 (2008).

42. Huang, T. C., Fukuda, K., Lo, C. M., Yeh, Y. H., Sekitani, T., Someya, T., Cheng, K. T. Pseudo-CMOS: A design style for low-cost and robust flexible electronics. *IEEE Trans. Electron Devices* **58**, 141-150 (2011).

43. Park, S. I., Ahn, J. H., Feng, X., Wang, S. D., Huang, Y. G., Rogers, J. A. Theoretical and experimental studies of bending of inorganic electronic materials on plastic substrates. *Adv. Funct. Mater.* **18**, 2673-2684 (2008).

44. Chae, S. H., Yu, W. J., Bae, J. J., Duong, D. L., Perello, D., Jeong, H. Y., Ta, Q. H., Ly, T. H., Vu, Q. A., Yun, M., Duan, X. F., Lee, Y. H. Transferred wrinkled Al_2O_3 for highly stretchable and transparent graphene-carbon nanotube transistors. *Nat. Mater.* **12**, 403-409 (2013).

45. Buchheit, M., Laursen, P. B., Ahmaidi, S. Parasympathetic reactivation after repeated sprint exercise. *Am. J. Physiol. Heart Circ. Physiol*. **293**, H133-H141 (2007).

Chapter 4. Skin mountable quantum dot light emitting diode display for indicating measured data

4.1 Introduction

A market demand for flexible and foldable displays[1, 2] has been rapidly growing, particularly for their application to future consumer electronics. For example, deformable displays[3, 4] can be integrated with recently spotlighted wearable electronics[5-7] as an information input/output port to/from the electronics. Meanwhile, the research scope of the wearable electronics has been expanded to the field of extremely thin skin-like electronics.[8-15] Accordingly, a "skin-like" display has become a critical component in the next-generation wearable electronics. The integrated skin-like display is expected to visually present a variety of information obtained from the electronics and provide a convenient user interface (UI) with minimal discomfort.

In pursuit of skin-like displays, many kinds of thin and/or micro-size light-emitting diodes (LEDs), including inorganic micro-LEDs (iLEDs),[1, 2] polymer LEDs (PLEDs),[3, 16, 17] and organic LEDs (OLEDs),[4, 18] have been developed on deformable substrates. However, practical challenges toward an ideal wearable display still remain, such as high

operating voltages, relatively thick form factors of final devices, and unsatisfactory stability and performances. In contrast to the above LED types, quantum dot (QD) LEDs offer unique and attractive characteristics that make them particularly suitable for next-generation wearable electronics and optoelectronics.[19, 20] Such characteristics include narrow bandwidths that enable high color purity,[21-23] wide bandgap tunability,[24, 25] high electroluminescence (EL) brightness at low operating voltages,[26] high photo/air stability,[27] high resolution patternability,[28-30] and easy processability for the device integration.[31, 32] Despite these advantages, a skin-like smart display that leverages QLEDs and its system-level integration with wearable sensors and electronics have not yet been reported.

We herein propose a skin-like red, green, and blue (RGB) QLED display that utilizes a passive matrix technology to address individual pixels. The ultra-thin thickness (~5.5 μm) of the skin-like QLED display enables its conformal contact with the skin, thereby reducing discomfort and preventing its failure under mechanical deformations. The core/shell QD structure is optimized to improve EL characteristics (*e.g.,* brightness up to 44,719 cd m^{-2} at 9 V, which is the highest record among wearable LEDs reported to date) by suppressing the nonradiative recombination of QDs. Owing to this high performance of the individual pixels, the display based on an array of QLEDs provides satisfactory brightness during its sequential scanning operation with a minimal temperature increase. In addition, various patterns, including those comprised of letters, numbers,

symbols, and animations, are successfully visualized on the skin-mounted QLED display. Furthermore, the combination of the skin-like QLED display with flexible driving circuits and wearable sensors results in a fully integrated smart skin-like QLED display with a touch UI.

4.2. Experimental section

Synthesis of QDs: A series of green light-emitting CdSe/ZnS core/shell QDs with alloyed interfaces were synthesized by reacting metal–oleate complexes, trioctylphosphine sulfide (TOPS), and trioctylphosphine selenide (TOPSe). For preparation of metal–oleate complexes, 0.2 mmol of CdO, 3.5 mmol of $Zn(OAc)_2$, 4.0 mL of OA, and 15.0 mL of 1-ODE were mixed and then heated under vacuum for 2 h at 120 °C. The mixture was heated to 300 °C under Ar atmosphere. Then, 0.2 mmol of TOPSe (2 M) was rapidly injected, followed by the injection of 3.5 mmol of TOPS (2 M) to form ZnS shells on the cores. The reaction mixture was maintained at 300 °C for 3 min, 5 min, and 12 min to respectively acquire C/S, C/S^{+}, and C/S^{++} QDs. To obtain QDs with the thickest shells (C/S^{+++}), 1 mmol of $Zn(oleate)_2$and 1 mL of 1-octanthiol were additionally injected into the reaction mixture containing C/S^{++} QDs. The mixture was then further heated at 300 °C for 2 min. Blue- and red-emitting QDs were synthesized by controlling the core sizes and compositions using similar methods. The products were purified by repeated centrifugation with precipitation/redispersion processes to remove unreacted reagents.

Synthesis of ZnO NPs: The ZnO NPs in butanol were synthesized in the laboratory. First, 1.23 g of $Zn(OAc)_2•2H_2O$ in 55 ml of methanol was prepared. Then, 0.48 g of KOH in 25 ml methanol was slowly injected to the prepared solution for 2 h at 60 °C. After the addition, the solution

kept at 60 °C for another 2 h. Finally, the solution was purified by repeating the precipitation and dispersion of the ZnO NP solution. The precipitation was performed by centrifugation using the solution of 10 ml ZnO NP solution, 20 ml hexane, and 5 ml isopropyl alcohol. After redispersing the ZnO NPs in 2 ml butanol, the ZnO NP solution was filtered through a 200-nm porous polytetrafluoroethylene (PTFE) filter before use.

QLED Display Fabrication: The skin-like QLED display was fabricated on a 2.5 cm×2.5-cm slide glass substrate. First, the substrate surface was coated with a fluorinated polymer layer (Teflon AF, Chemours). Then, a 1.2-μm-thick Parylene C layer was deposited on the surface (Parylene Coater, Obang Technology, Korea). An epoxy (SU8-2, MicroChem) layer was coated on the Parylene C layer as a planarization and additional encapsulation layer. A Cr/Au (7 nm/70 nm, interconnecting electrodes) layer was deposited by thermal evaporation process with a patterned metal shadow mask. In this study, the metal shadow masks were utilized to pattern interconnecting electrodes, anodes and cathodes. Next, an epoxy layer was coated and lithographically patterned to create vertical interconnect access (VIA) holes before deposition of 140-nm-thick ITO anodes by using a sputtering process (30 W, 45 min, 5 mTorr, 300 °C).

The CTLs and QD layer of the QLEDs were sequentially spin-coated and baked on the ITO anodes. First, the ITO anode surface was treated with ultraviolet ozone for 1 min before spin-coating of

PEDOT:PSS at 2,000 rpm for 30 s. The PEDOT:PSS layer was annealed at 150 °C for 15 min in the ambient atmosphere. It was annealed again at 150 °C for 15 min in a glove box to remove the residual solvent. Then, TFB (0.5 wt%) in *m*-xylene was spin-coated at 2,000 rpm for 30 s and annealed at 180 °C for 30 min in the glove box. After annealing, the QD layer was spin-coated at 2,000 rpm for 30 s and again annealed at 150 °C for 30 min. Finally, ZnO NPs in butanol were spin-coated and annealed in the same condition. All procedures after PEDOT:PSS annealing were processed in the glove box.

After coating processes of the CTLs and QDs, a 40-nm-thick Li:Al layer was deposited to form cathodes. A 20-nm-thick Au layer was subsequently deposited on Li:Al cathodes to prevent its oxidation, which could occur during the etching process of the encapsulation layers. After deposition of the cathodes, the double layer encapsulation (Parylene C/epoxy), which was the same as the bottom encapsulation layer, was deposited/coated on the device. To expose the electrode pads for interconnection with external driving circuits, the top encapsulation layers deposited on the electrode pads were etched using the reactive ion etching (RIE) process (O_2, 150 W, 0.1 Torr, 4 min). Heat-seal connectors (Elform, USA) were attached to the electrode pads by applying sufficient pressure and heat. These connectors electrically connected the QLED displays and external driving circuits. The whole display could be readily detached from the glass substrate on account of the poor adhesion between the fluorinated polymer layer and the bottom encapsulation layer of the QLED

display. Before the detachment, an additional supporting layer could be coated on the top encapsulation layer for facilitating easy handling of the ultra-thin QLED display. Specific patterns/images/information could be visualized against the wearer's skin after attaching the freestanding QLED display to the skin after inverting the QLED display.

Turn-on Voltage Decision and Statistical Analysis: We define the turn-on voltage as the necessary voltage inducing the current density of 2 mA cm^{-2}, which corresponds to the brightness of 10 cd m^{-2}. For the 24×24 QLED array used in Figures 3c-d, the average turn-on voltage is 2.64 V, while the median value and standard deviation are 2.8 V and 0.53 V, respectively.

4.3 Results and discussion

4.3.1. Device overview

Figure 4.1a shows an exploded view of the skin-like QLED display. The QLED display consists of indium tin oxide (ITO) anodes (Figure 4.1a, v), lithium-doped aluminum (Li:Al)/gold (Au) cathodes (Figure 4.1a, iii), and charge transport layers (CTLs) with a QD layer (Figure 4.1a, iv). The CTLs and QD layer, which are composed of a hole injection layer (HIL), hole transport layer (HTL), QDs, and an electron transport layer (ETL) (Figure 4.1a, bottom-left inset), are sandwiched between the anodes and cathodes.

All materials for the anode, cathode, CTLs, and QD layer were carefully selected with consideration of their energy band alignment for efficient transport of electrons and holes (Figure 4.1a, top-right inset). The ITO anodes were designed to form separate islands to prevent their mechanical failure under deformation. Chromium (Cr)/Au electrodes (Figure 4.1a, vii) connect these island-shape ITO anodes through vertical interconnect access (VIA) holes of the epoxy insulation layer (Figure 4.1a, vi). The whole device is encapsulated with Parylene C (Figure 4.1a, ii and ix)/epoxy (Figure 4.1a, i and viii) double layers (top and bottom encapsulation).

Figure 4.1b presents a photograph of the skin-like 16×16 green QLED display visualizing the letters "QLED 16×16" on the deformed

skin. The display can visualize other complicated images as well, such as the symbols of Superman™, Avengers™, and Batman™ (Figure 4.1b, insets). The cross-sectional transmission electron microscopy (TEM) images depict the layered structure composed of the anode (~140 nm), HIL (~50 nm), HTL (~35 nm), QD layer (~35 nm), ETL (~30 nm), and cathode (~50 nm) (Figure 4.2). Quantitative material analysis was performed using energy-dispersive X-ray spectroscopy (EDS) to provide the layered spatial distributions of key elements (Figure 4.2).

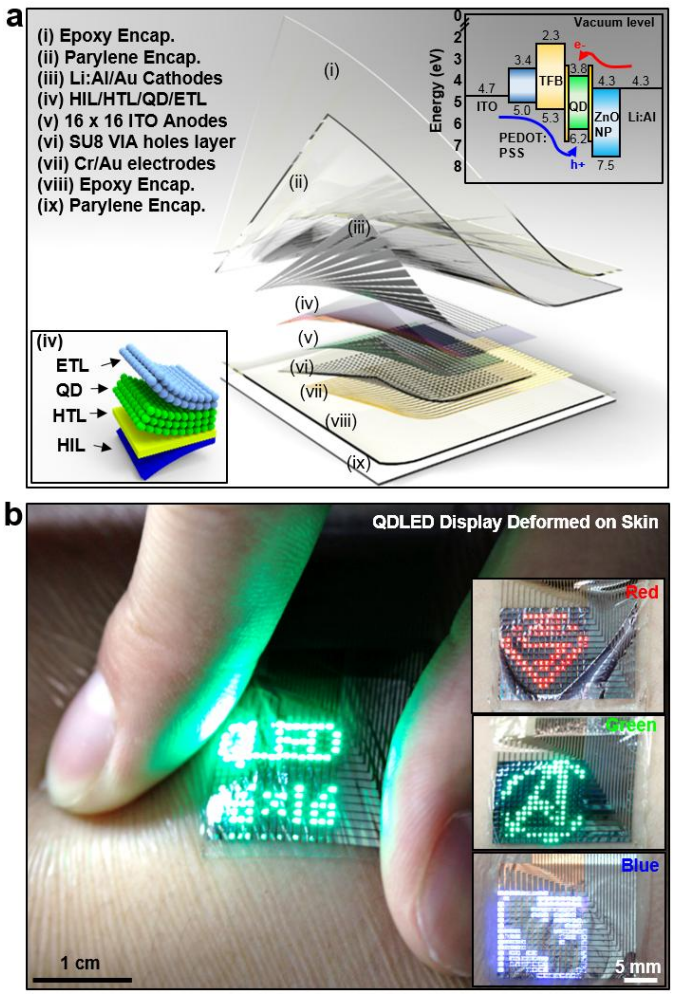

Figure 4.1. Overview of the skin-like QLED display. a, Exploded view of the skin-like QLED display showing layer information, schematic illustration of the CTLs and QD layer (bottom-left inset), and the energy band diagram of the QLED (right-top inset). **b,** Photograph of the skin-like QLED display (displaying "QLED 16×16") on the deformed skin. The insets show photographs of the RGB display on skin.

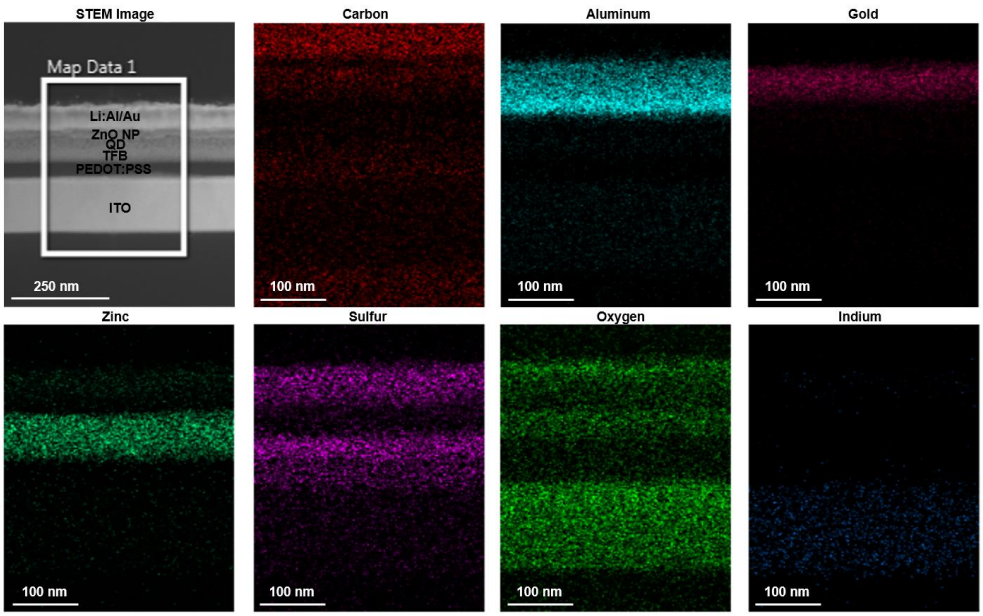

Figure 4.2. EDS analysis results. Two-dimensional EDS mapping images for the cross-section of the QLED display.

4.3.2. QD optimization

To achieve the high brightness and low operating voltage of the QLED display, the structure of QDs was optimized. In particular, we prepared QDs of controlled shell thicknesses with the same core. The TEM images (Figures 4.3a-d) show that the QD size increases as the shell grows. Their average diameters are 5.6, 7.2, 9.0, and 10.5 nm for the samples denoted as C/S, C/S^{+}, C/S^{++}, and C/S^{+++}, respectively. The EDS line scan analysis (Figure 4.3e) of C/S QD confirms the successful growth of the additional zinc sulfide (ZnS) shell on the core (Figure 4.3f). All samples have high quantum yields (QY) of ~80%, except for the QD with the thinnest shell thickness (Figure 4.4a). The photoluminescence (PL) maxima of the QDs are slightly blue-shifted as the shell grows (Figure 4.4b), which implies atomic interdiffusion at the core–shell interface. This alloyed core–shell interface is advantageous for the effective charge carrier injection.[33]

Time-resolved PL (TRPL) spectra were measured for QDs assembled in the device (*i.e.* ITO/HIL/HTL/QDs/ETL/Li:Al) to study the effects of the shell thickness on the carrier dynamics. The exciton carrier lifetime of the QDs in the device increases with the growing shell thickness (Figure 4.4d), demonstrating that the thick shells suppress non-radiative recombination, such as the Auger recombination or defect transition.[34-36]

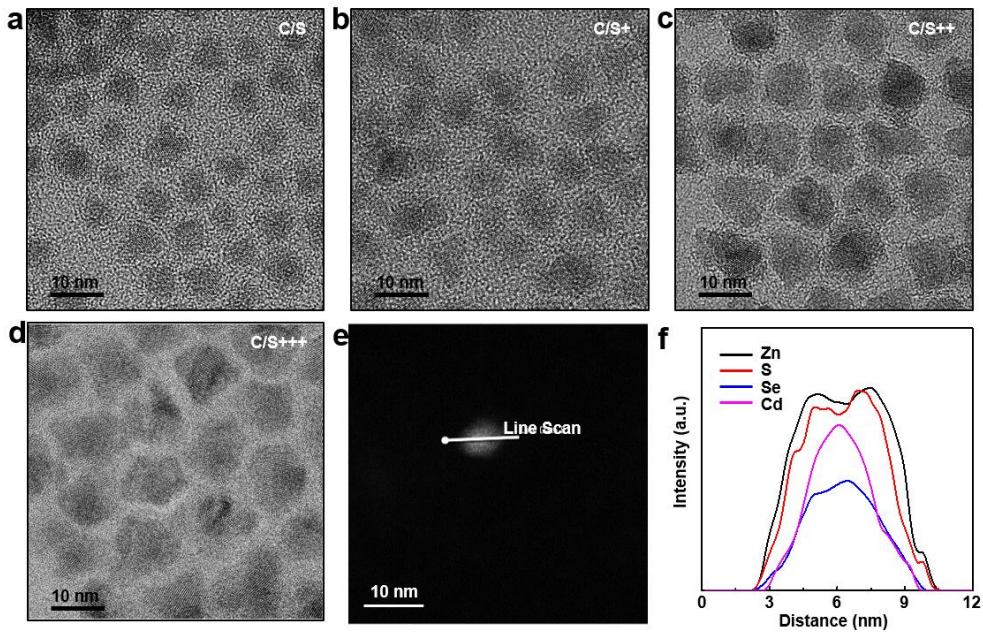

Figure 4.3. Optimization of QDs. a-d, TEM images showing the QDs of different shell thicknesses: **a,** 5.6 (C/S), **b,** 7.2 (C/S^{+}), **c,** 9.0 (C/S^{++}), and **d,** 10.5 nm (C/S^{+++}). **e,** TEM image showing a C/S QD and the scan line. **f,** EDS line scan analysis of the C/S QD showing the elemental distribution of Cd (magenta), Zn (black), Se (blue), and S (red).

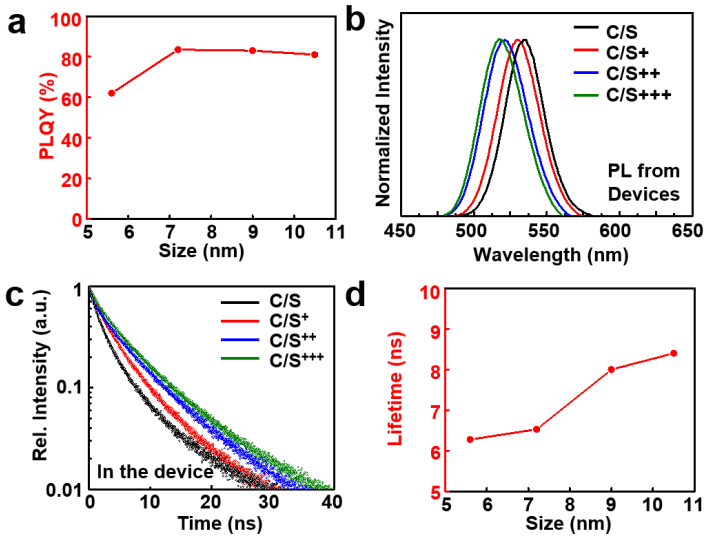

Figure 4.4. Comparison between the characteristics of QDs with different shell thickness. a, QY of QD samples. **b,** PL spectra of C/S, C/S^{+}, C/S^{++}, and C/S^{+++} QDs with controlled shell thicknesses. The data were obtained from the QD film in the QLED devices. **c,** TRPL spectra of the QDs assembled in the device structure. **d,** Average carrier lifetime of the QDs.

4.3.3. EL performance of the QDs

The optimization of the QD structure greatly enhanced the performance of the QLEDs (Table 4.1). In particular, the QLEDs based on C/S^{++} QDs exhibit a remarkable brightness of 44,719 Cd m^{-2} at an applied voltage of 9 V, which is the highest brightness among all types of wearable LEDs reported so far. The QLEDs based on QDs with relatively thick shells (*i.e.* C/S^{++} and C/S^{+++} QDs) show a higher brightness than those based on thin shells (*i.e.* C/S and C/S^{+} QDs), which can be attributed to suppression of the non-radiative recombination. On the other hand, the current density decreases with increasing shell thickness on account of the inefficient charge carrier injection through the thick shells. In the case of luminous efficiency, the QLEDs using C/S^{+++} QDs show the best performance (Figure 4.5a). However, they exhibit low brightness at the low applied voltage range, which is not suitable for wearable and/or mobile electronics. Thus, we employed C/S^{++} QDs as an optimum in the following applications. The current techniques of QD optimization can be extended to all of RGB QDs for realization of a full color display. The optical spectra of RGB QDs are provided in Figure 4.5b and Commission International de l'Éclairage coordinates of each QLED (Figure 4.5c) show true RGB emissions.

Table 4.1. EL performances of the QLEDs. Summary of EL performance of the QLEDs based on structurally modified QDs.

QDs	Max. Brightness (@ 9V) [Cd m^{-2}]	EL @ 5V		EL @ 6V	
		J [mA cm^{-2}]	Brightness [Cd m^{-2}]	J [mA cm^{-2}]	Brightness [Cd m^{-2}]
C/S	5437	422.9	950	636.9	1698
C/S^{+}	9504	268.3	475	443.8	1356
C/S^{++}	44719	140.9	4157	302.2	10784
C/S^{+++}	41653	30.3	848	119.4	5596

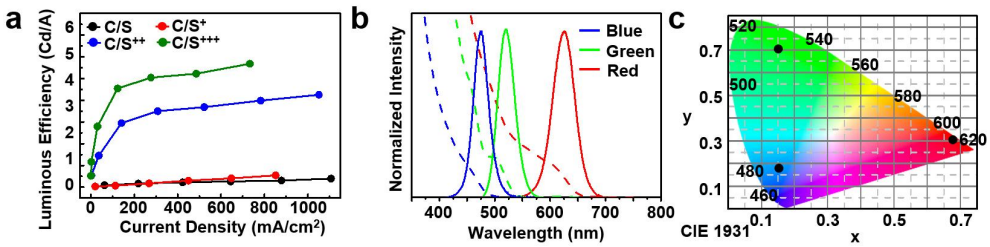

Figure 4.5. Efficiency, PL spectra, and, CIE 1931 x-y chromaticity diagram. a, Luminous efficiency of the QLEDs using QDs with different shell thicknesses. **b,** Absorption (dashed lines) and PL spectra (solid lines) of the red, green (C/S^{++}), and blue QDs used in this study. **c,** CIE 1931 x–y chromaticity diagram of the RGB QLED.

4.3.4. Ultra-thin QLED display

Figure 4.6 presents a schematic diagram of the passively driven QLED display using a common cathode configuration. The external circuit sequentially controls one row (cathode) and all columns (anode) for each cycle (Figure 4.7). The 16×16 passively driven QLED display effectively visualizes information without flickering. This is because the refresh rate is higher than the critical flicker fusion threshold (~60 Hz) when the scan speed of 1 ms/line is used.

It is important to suppress the temperature increase of the display when applying the skin-like display to wearable electronics. We measured the temperature increase by applying square-wave voltages of different duty cycles to the 3×3 QLED array (Figure 4.8). It can be inferred that the temperature of the 16×16 QLED display (corresponding duty cycle: 6.25%) remains below 28.5 °C at the 6~8 peak-to-peak voltage (V_{pp}). Two dimensional maps of the QLED surface temperature under various bias conditions are provided in Figure 4.9. The luminescence of the passively driven display is lower than that of the actively driven display at the same operation voltages (Figure 4.10). However, the superior EL properties of the optimized QDs enable the passively driven QLED display to have a sufficient brightness of 674 cd m^{-2} at 6 V_{pp} (*cf.* maximum brightness of iPhone 7: 625 cd m^{-2}).

The encapsulation composed of a Parylene C/epoxy bilayer provides a good waterproof property to the skin-like QLED display

(Figure 4.11a). The ultra-thin thickness prevents its mechanical failure under harsh mechanical conditions, such as rolling (Figure 4.11b) and repeated bendings up to 1,000 cycles (Figure 4.11c for 8×8 QLED display and Figure 4.11d for 16×16 QLED display). Therefore, it can reliably visualize various types of information against the wearer's skin using both 8×8 and 16×16 skin-like QLED display (Figure 4.12). The brightness can be readily controlled by varying the applied voltages (Figure 4.13).

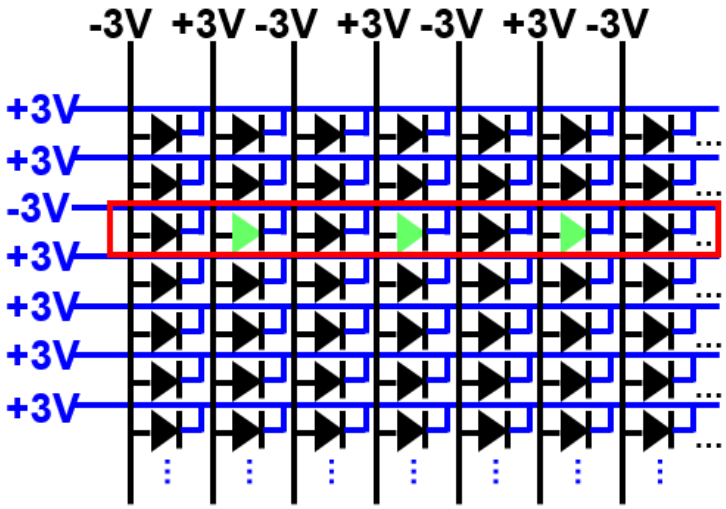

Figure 4.6. Schematic of passively driven QLED matrix. Schematic design of the common cathode QLED passive matrix and its operation scheme.

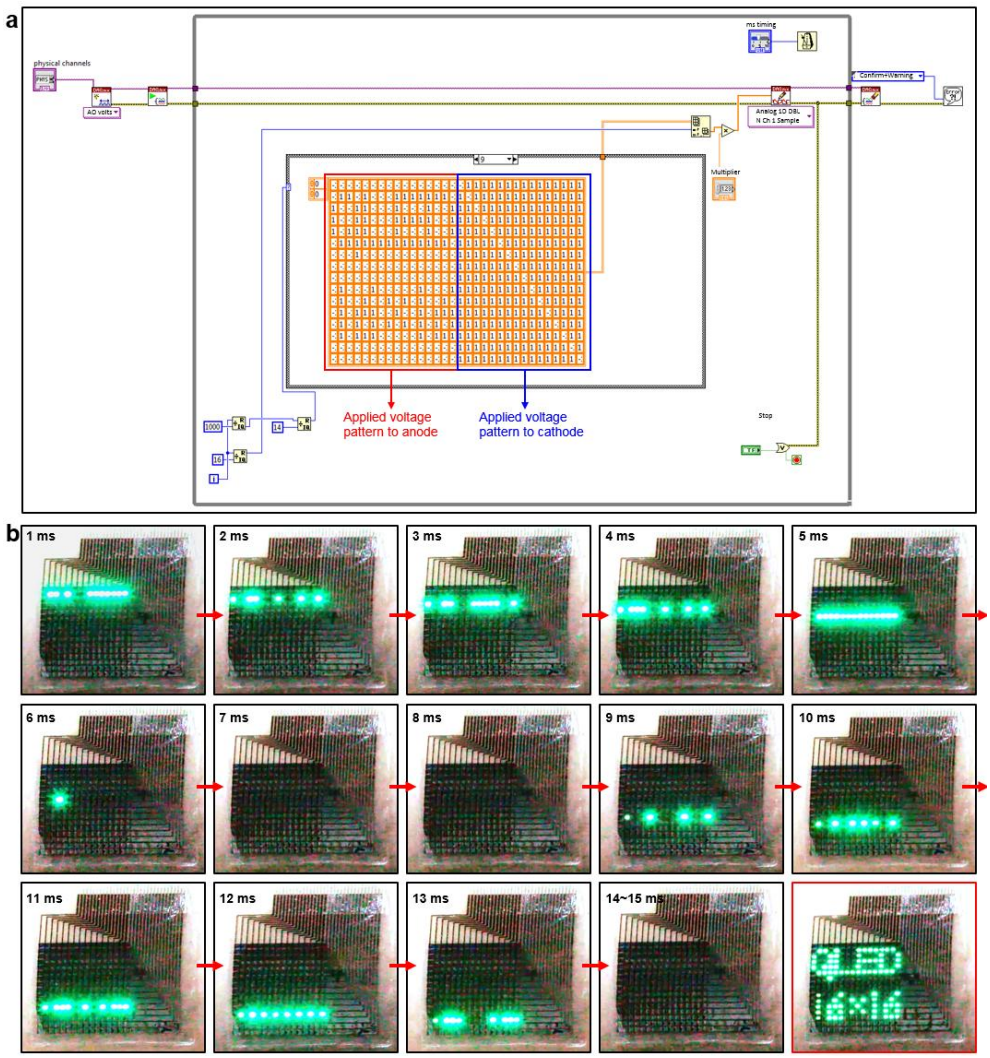

Figure 4.7. Control scheme of the 16×16 QLED display. a, Block diagrams of LabVIEW-based software for visualizing "QLED 16×16" on the skin-like QLED display. **b,** Sequential photographs showing the line-by-line operation of the skin-like QLED and the complete image obtained when the scan speed is 1 ms/line (red box).

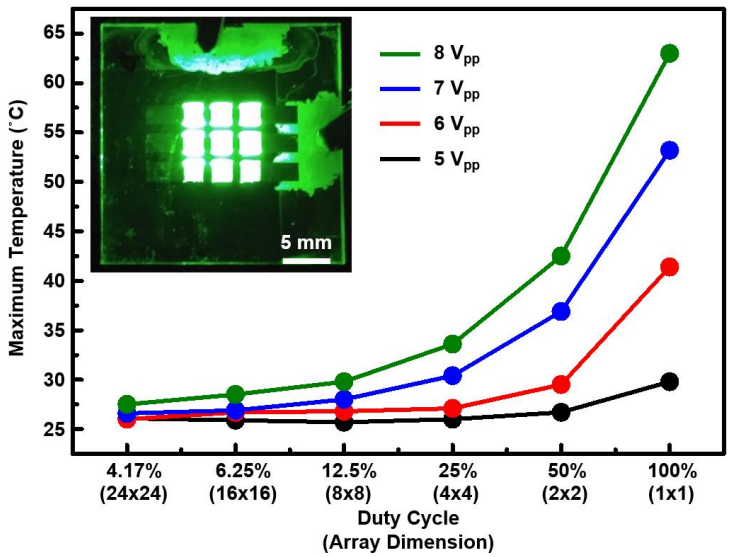

Figure 4.8. Temperature increase during QLED operation. Maximum temperature of the QLED display depending on the amplitude and duty cycle of the applied voltage. The 3×3 QLED array is used for this analysis (inset).

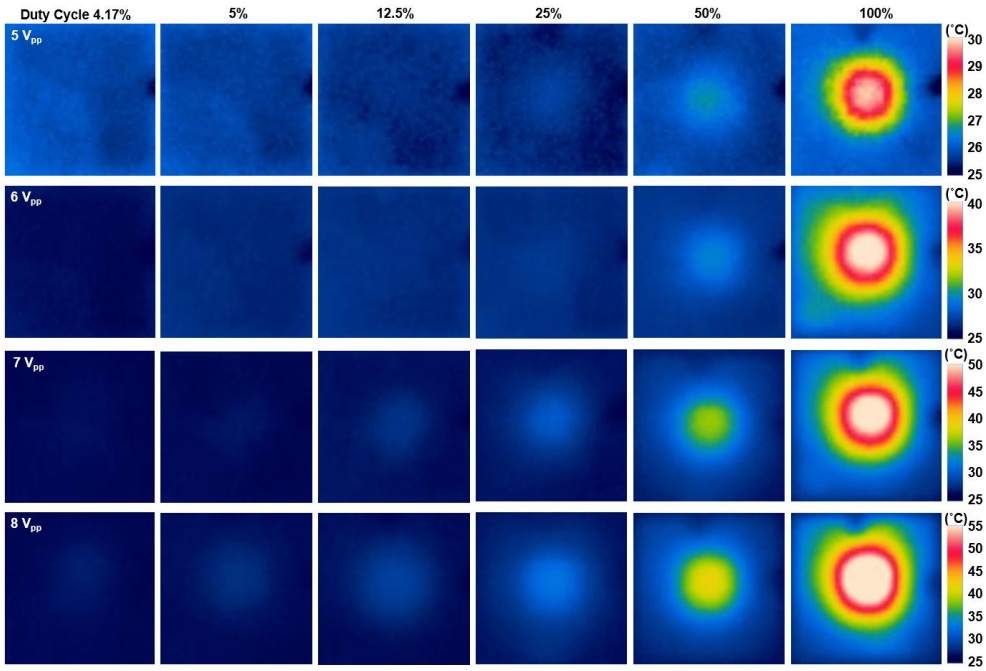

Figure 4.9. IR camera images of the QLED display. Two-dimensional temperature distribution of the QLED display depending on the amplitude and duty cycle of the applied voltage.

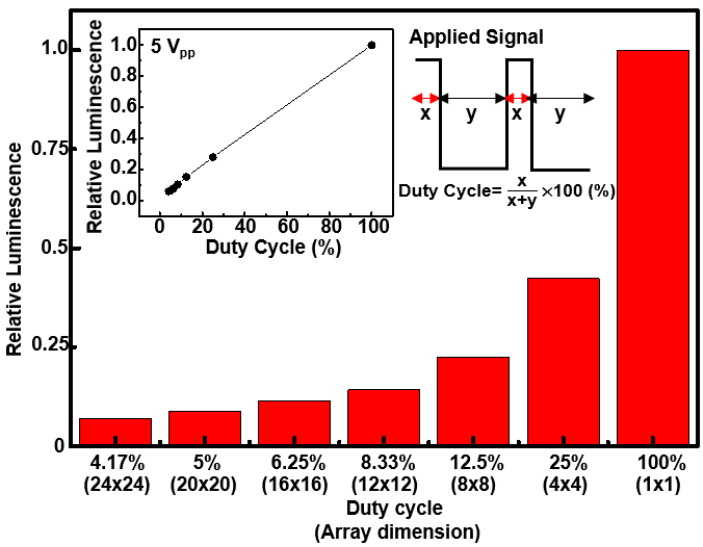

Figure 4.10. Relative luminescence depending on duty cycle. Relative luminescence of the QLED display depending on the duty cycle of the applied voltage. A linear relationship exists between the relative luminescence and duty cycle (top-left inset). The definition of the duty cycle is schematically explained in the top-right inset.

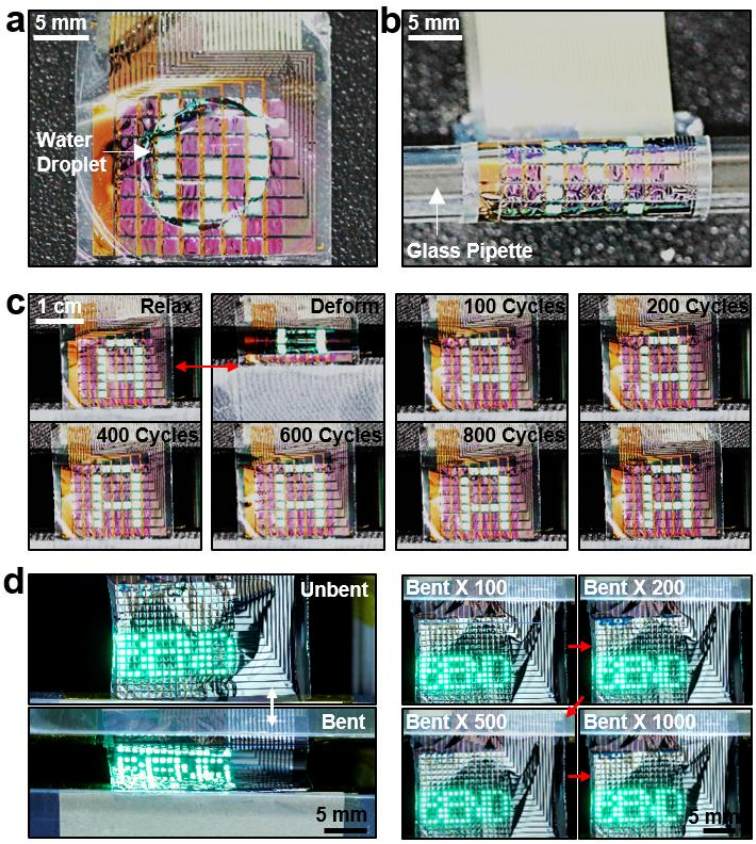

Figure 4.11. Reliable operation of the skin-like QLED display under various conditions. **a-b,** Photographs of the skin-like QLED display demonstrating **a,** it's waterproof property and stable operation in **b,** rolled condition. **c-d,** Photographs of the skin-like QLED display demonstrating durability after repeated bending of 1,000 cycles for the case of **c,** 8×8 QLED display and **b,** 16×16 QLED display.

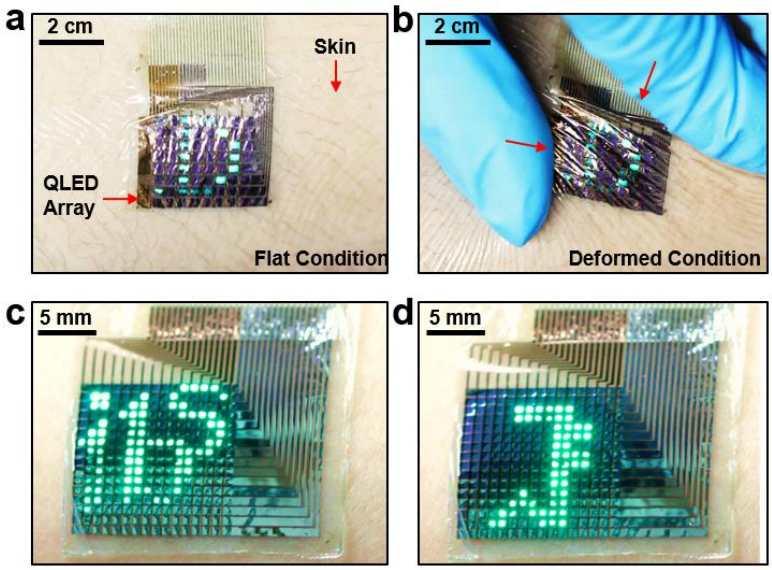

Figure 4.12. Skin-like QLED display laminated on the skin. a-b, 8×8 QLED display laminated on the skin **a,** without deformation and **b,** with deformation. **c-d,** Various images shown on the 16×16 QLED display laminated on the skin.

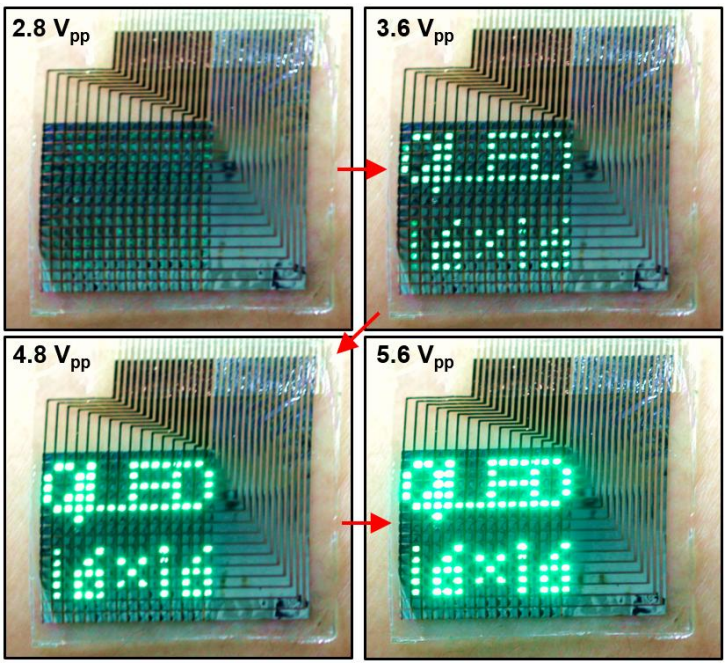

Figure 4.13. Luminescence control. Sequential photographs showing the luminescence change depending on the amplitude of the applied voltage.

4.3.5. Skin-like QLED display integrated with wearable electronics

The developed 8×8 skin-like QLED display (Figure 4.14a, v) is integrated with a touch sensor (Figure 4.14a, vi) and flexible electronics. The flexible electronics is composed of driving circuits (Figure 4.14a, iii and iv) and sensors (temperature sensor and accelerometer; Figure 4.14a, i and ii) on a flexible printed circuit board. Data flows between the electronic components, a skin-like display (text scrolling), and a touch sensor UI are schematically illustrated in the Figure 4.14b. The design of the flexible printed circuit board and the information of the electrical components are provided in the Figure 4.15 and Table 4.2, respectively. The microcontroller unit (MCU; Figure 4.14a, iii) processes the temperature (Figure 4.16a) and acceleration (Figure 4.16b) data as well as calculates the magnitude of the acceleration vector for estimating step counts (Figure 4.16b). The integrated touch sensor works as an efficient UI, through which the user can change sensing modes (Figure 4.16c). The capacitance change between the touch sensor and a finger induces the change in the resistive–capacitive (RC) delay (Figure 4.16c, inset). The MCU monitors this RC delay in real time and distinguishes the motion between the tapping and intimate contact of the finger to the touch sensor (Figure 4.16d).

The fully integrated wearable system—the skin-like QLED display co-integrated with the flexible electronics—can be readily worn on the user's wrist (Figure 4.17a). We demonstrated the real-time visualization of

the temperature and step counts measured by the integrated sensors, while the ambient temperature was increased and/or the user was running (Figure 4.17b-c). The wearer can toggle between different modes, *i.e.* the temperature monitor and pedometer, by using the touch sensor. We additionally demonstrated that letters, numbers, and various symbols can be displayed on the skin-mounted device (Figure 4.18) The detailed pseudo-code implemented for the demonstration is shown in Figure 4.19.

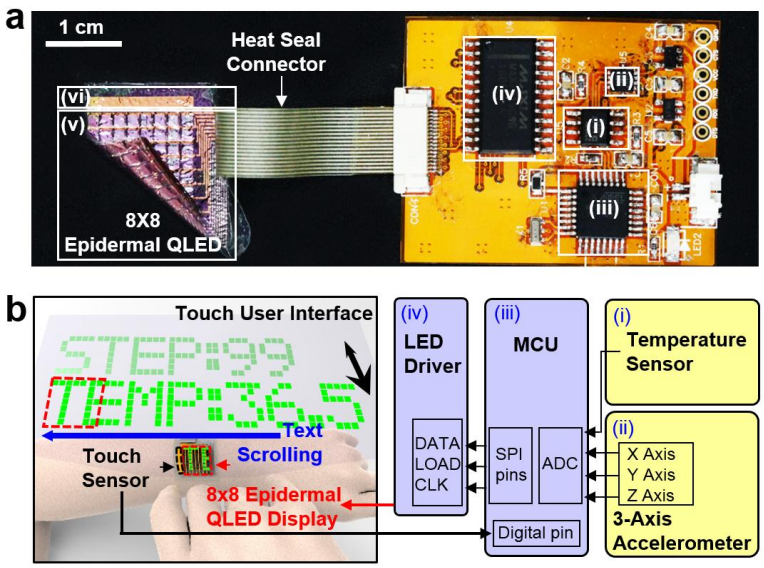

Figure 4.14. QLED display integrated with wearable electronics. a, Photograph of the skin-like QLED display integrated with the wearable electronics. **b,** Schematic illustrations showing data flows between the integrated electronic components and display.

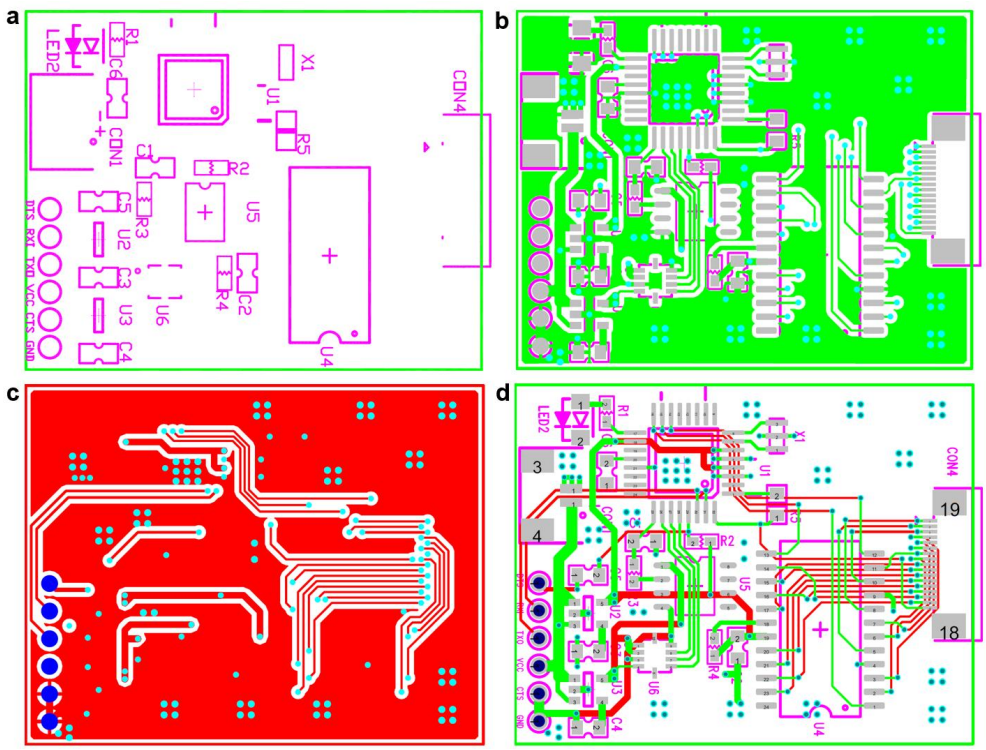

Figure 4.15. Design of the flexible printed circuit board. a-d, Layout of the flexible printed circuit board showing **a,** the component numbers, **b,** connection map 1, **c,** connection map 2, and **d,** combined connection map.

Table 4.2. Chip information of the wearable electronic circuits.

Component number	Type	Value	Model
R1	MCU LED Resistor	330 Ω	R1608G3300F1-10W50V
R2	DTS Resistor	10 kΩ	R1608G1002F1-10W50V
R3	TEMP Sensor Filter Resistor	1 kΩ	R1608G1001F1-10W50V
R4	LED Driver Resistor	10 kΩ	R1608G1002F1-10W50V
R5	Touch Sensor Resistor	10 MΩ	RH73H2A10MKTN
C1	TEMP Sensor Filter Capacitor	0.1 µF	C2012Y5V104Z50V
C2	VCC Capacitor	0.1 µF	C2012Y5V104Z50V
C3	5.0 V Regulator Bypass Capacitor	10 nF	C2012X7R103K50V
C4	3.3 V Regulator Bypass Capacitor	10 nF	C2012X7R103K50V
C5	DTS Capacitor	0.1 µF	C2012Y5V104Z50V
C6	AREF Capacitor	0.1 µF	C2012Y5V104Z50V
X1	Resonator	8 MHz	CSTCE8M00G55-R0
U1	Microcontroller (MCU)	N/A	ATMEGA328P-AU
U2	5.0 V Regulator	N/A	LP2985-50DBVR
U3	3.3 V Regulator	N/A	LP2985-33DBVR
U4	LED Driver	N/A	MAX7219CWG+
U5	TEMP Sensor	N/A	AD22103KRZ
U6	Accelerometer	N/A	KXTC9-2050-FR
CON1	Battery Connector	N/A	0532610271
CON4	FPC Connector	N/A	1-1734839-7
LED2	MCU Status LED	N/A	LY N971-HL-1

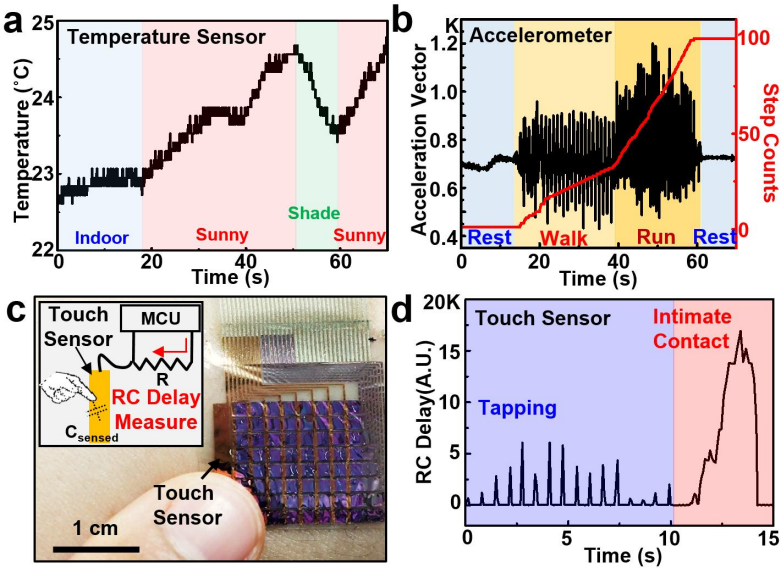

Figure 4.16. Temperature, step counts, and touch measurement. a, Measured temperature change depending on the locations. **b,** Amplitude change in the acceleration vector (black) and calculated step counts (red),when the wearer is resting, walking, and running. **c,** Photograph of the touch sensor integrated with the skin-like QLED display. The inset shows a schematic illustration of the measurement setup. **d,** Measured RC delay when the touch sensor is tapped or intimately contacted by a finger.

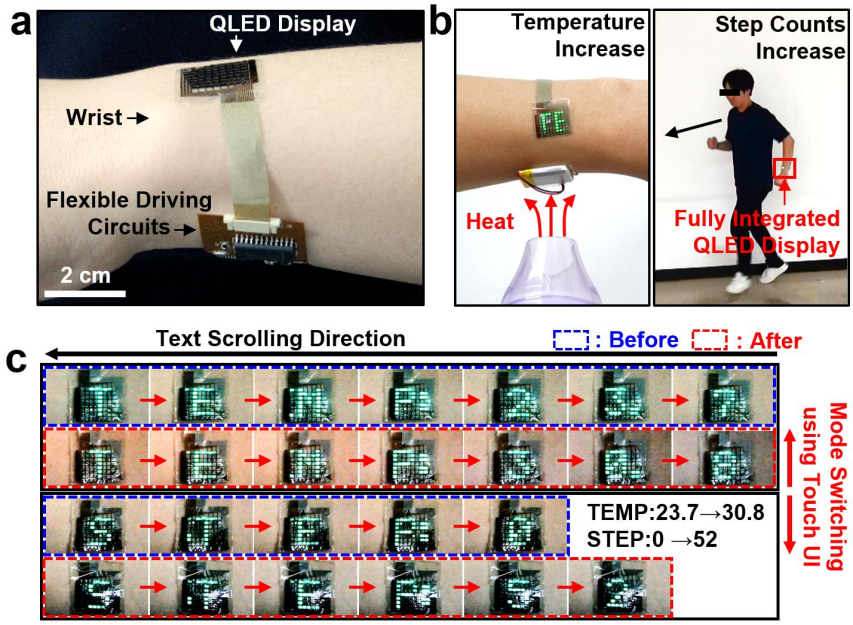

Figure 4.17. Demonstration using the fully integrated QLED display. a, Photograph of the integrated wearable system worn on a user's wrist. **b,** Photograph of the integrated wearable system subjected to external heat (left) and that of the running wearer (right). **c,** Sequential photographs of the skin-mounted QLED display visualizing the measured temperature and pedometer data in the scroll mode.

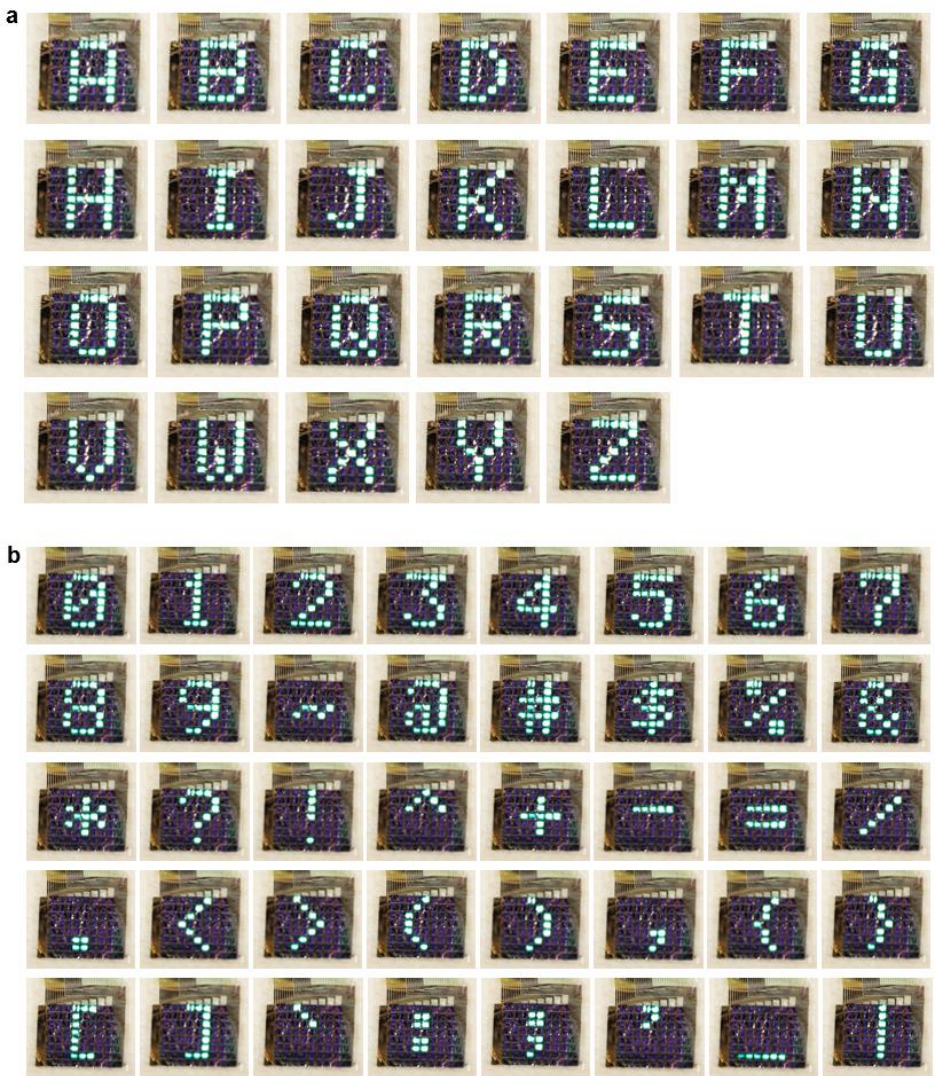

Figure 4.18. Skin-mounted QLED display freely visualizing various patterns. a, Uppercase letters visualized in the skin-like 8×8 QLED display laminated on the wearer's skin. **b,** Numbers and symbols visualized in the skin-like 8×8 QLED display laminated on the wearer's skin.

a

```
#include <avr/pgmspace.h>
#include <LedControl.h>
#include <CapacitiveSensor.h>

//Temp, Acc Constants and Functions
const int Temp = A2;
const int AccX = A5;
const int AccY = A4;
const int AccZ = A3;
const float Vref = 3.7;
void readsensorval();
void pedocal();
float TempVal = 0;
long AccXVal = 0;
long AccYVal = 0;
long AccZVal = 0;
long totvect = 0;
float sec = 0;
long pedocalnum =0;

//for step calculation
#define HISTORY_SIZE 50
int history[HISTORY_SIZE];
int hc=0;
int avg;
boolean overPeak;
int threshold = 100;
int steps = 0;

//LED and Touch Constants
const int DIN = 12;          //DataIn pin (18)
const int CLK = 11;          //Clock pin (17)
const int LOAD = 10;         //Load pin (16)
const int numDevices = 1;    //Number of MAX7219 LED Driver Chips (1-8)
const long scrollDelay = 50;
const long touch_th = 50000;   //Touch threshold
const int SensorPin1 = A0;
const int SensorPin2 = A1;
const int SensorPin3 = A2;
const int sensornum = 2; //number of sensors
char Final_Display[15];
char SensorVal1[15];
char SensorVal2[15];

const char font5x7 [] PROGMEM = {     //Numeric Font Matrix (Arranged as 7x font
data + 1x kerning data)
   B00000000,  //Space (Char 0x20)
   B00000000,
   B00000000,
   B00000000,
   B00000000,
   B00000000,
   B00000000,
   6,

   B10000000,  //!
   B10000000,
   B10000000,
   B10000000,
   B00000000,
   B00000000,
   B10000000,
   2,
   .....};

unsigned long bufferLong [14] = {0};  //Buffer for scrolling text
LedControl lc=LedControl(DIN,CLK,LOAD,numDevices);
CapacitiveSensor   cs_4_2 = CapacitiveSensor(3,2);      // 10M resistor between
pins 4 & 2, pin 2 is sensor pin, add a wire and or foil if desired
int mode = 0;
unsigned long touchcount = 0;
boolean touched = false;
char TempBuffer[10];
char StepBuffer[10];

int startflag=1;
```

b

```
void setup() {
  for (int x=0; x<numDevices; x++){
     lc.shutdown(x,false);     //The MAX7219 is in power-saving mode on startup
     lc.setScanLimit(x,6);     //Scan limit to make it brighter
     lc.setIntensity(x,15);    // Set the brightness to the highest value
     lc.clearDisplay(x);       // and clear the display
  }
  Serial.begin(9600);
  pinMode(13, OUTPUT);
}

void loop() {
  // read the analog in value:
  Final_Display[0]='\0'; // initialize char array
  if(startflag==1){
   strcat(Final_Display, "START!!");
  }
  else if (mode==0){
   strcat(Final_Display," TEMP:\0");
   strcat(Final_Display, TempBuffer);
  }
  else if (mode==1){
   strcat(Final_Display," STEP:\0");
   dtostrf(steps, 3, 0, StepBuffer);
   strcat(Final_Display, StepBuffer);
  }

  scrollMessage(Final_Display);
  startflag=0;
}
```

c

```
void readsensorval(){
  TempVal; //Temperature Value Measurement
  dtostrf(TempVal, 5, 1, TempBuffer); //Assign Temperature Value to TempBuffer
  AccXVal ;  AccYVal;  AccZVal;  //Acceleration value measurement
  totvect;  //totvect value = sqrt((AccXVal*AccXVal)+(AccYVal*AccYVal));
}

void pedocal(){
  //calculate moving average
  if (hc<HISTORY_SIZE) hc++;  else hc=0;  history[hc]=(int)totvect;  long sum;
  if (pedocalnum>100){
  for(int i=0;i<HISTORY_SIZE;i++){//sum all value in history array}
  avg=sum/HISTORY_SIZE;
  if(totvect>(avg+threshold)){//if the value is larger than threshold+avg, steps++,
overpeak=true}

int touchcheck() {
  long start = millis();
  long total1 =  cs_4_2.capacitiveSensor(30);
  //once touch is applied mode++, turn on the led
}

void scrollFont() {
   for (int counter=0x20;counter<0x80;counter++){
      loadBufferLong(counter);}
}

void scrollMessage(char * messageString) {
   int counter = 0;  int myChar=0;
   do {// read back a char
      myChar = messageString[counter]; //get a character from the messageString
      //myChar =  pgm_read_byte_near(messageString + counter);
      if (myChar != 0){loadBufferLong(myChar);} counter++;
   } while (myChar != 0);}

void loadBufferLong(int ascii){// Load character into scroll buffer
for (byte x=0; x<count;x++){rotateBufferLong(); printBufferLong(); touchcheck();
readsensorval(); pedocal();   delay(scrollDelay);
}
}

void rotateBufferLong(){// Rotate the buffer
}
void printBufferLong(){// Display Buffer on LED matrix
}
```

Figure 4.19. Pseudo-code used in the demonstration. a, Parameter setting portion of the code. **b,** Setup and loop functions of the code. **c,** Pseudo-code for sensing touch, measuring temperature and acceleration, calculating amplitude of the acceleration vector and step counts, and visualizing information on the 8×8 QLED display.

4.4 Conclusion

In summary, we developed an ultra-thin skin-like QLED display that can visualize various types of information retrieved from the wearable electronics, in close proximity to the wearer's skin. The optimized shell thickness of the QDs maximized the EL performance. As a result, the skin-like QLED display successfully visualized various information with high brightness and low operation voltages. The skin-like QLED display showed a minimal temperature increase during operation, rendering it safe for use against the skin. Furthermore, its waterproof property and robustness under harsh mechanical deformations confirmed its reliability in use. The developed skin-like QLED display was integrated with flexible circuits to form a wearable system. The integrated system reliably monitored temperature and body motion changes, analyzed the data, and directly visualized them against the wearer's skin. These results provide new insights and opportunities for advancing next-generation wearable displays and electronics.

References

1. Park, S. I., Xiong, Y. J., Kim, R. H., Elvikis, P., Meitl, M., Kim, D. H., Wu, J., Yoon, J., Yu, C. J., Liu, Z. J., Huang, Y. G., Hwang, K., Ferreira, P., Li, X. L., Choquette, K., Rogers, J. A. Printed assemblies of inorganic light-emitting diodes for deformable and semitransparent displays. *Science* **325**, 977-981 (2009).

2. Kim, H. S., Brueckner, E., Song, J. Z., Li, Y. H., Kim, S., Lu, C. F., Sulkin, J., Choquette, K., Huang, Y. G., Nuzzo, R. G., Rogers, J. A. Unusual strategies for using indium gallium nitride grown on silicon (111) for solid-state lighting. *Proc. Natl. Acad. Sci. USA* **108**, 10072-10077 (2011).

3. Yokota, T., Zalar, P., Kaltenbrunner, M., Jinno, H., Matsuhisa, N., Kitanosako, H., Tachibana, Y., Yukita, W., Koizumi, M., Someya, T. Ultraflexible organic photonic skin. *Sci. Adv.* **2**, e1501856 (2016).

4. Wang, C., Hwang, D., Yu, Z. B., Takei, K., Park, J., Chen, T., Ma, B. W., Javey, A. User-interactive electronic skin for instantaneous pressure visualization. *Nat. Mater.* **12**, 899-904 (2013).

5. Jung, S., Kim, J. H., Kim, J., Choi, S., Lee, J., Park, I., Hyeon, T., Kim, D. H. Reverse-micelle-induced porous pressure-sensitive rubber for wearable human-machine interfaces. *Adv. Mater.* **26**, 4825-4830 (2014).

6. Lee, H., Choi, T. K., Lee, Y. B., Cho, H. R., Ghaffari, R., Wang, L., Choi, H. J., Chung, T. D., Lu, N. S., Hyeon, T., Choi, S. H., Kim, D. H. A graphene-based electrochemical device with thermoresponsive microneedles for diabetes monitoring and therapy. *Nat. Nanotech.* **11**, 566-572 (2016).

7. Jung, S., Lee, J., Hyeon, T., Lee, M., Kim, D. H. Fabric-based integrated energy devices for wearable activity monitors. *Adv. Mater.* **26**, 6329-6334 (2014).

8. Kim, J., Lee, M., Shim, H. J., Ghaffari, R., Cho, H. R., Son, D., Jung, Y. H., Soh, M., Choi, C., Jung, S., Chu, K., Jeon, D., Lee, S. T., Kim, J. H., Choi, S. H., Hyeon, T., Kim, D. H. Stretchable silicon nanoribbon electronics for skin prosthesis. *Nat. Commun.* **5**, 5747 (2014).

9. Kim, J., Son, D., Lee, M., Song, C., Song, J. K., Koo, J. H., Lee, D. J., Shim, H. J., Kim, J. H., Lee, M., Hyeon, T., Kim, D. H. A wearable multiplexed silicon nonvolatile memory array using nanocrystal charge confinement. *Sci. Adv.* **2**, e1501101 (2016).

10. Lim, S., Son, D., Kim, J., Lee, Y. B., Song, J. K., Choi, S., Lee, D. J., Kim, J. H., Lee, M., Hyeon, T., Kim, D. H. Transparent and stretchable interactive human machine interface based on patterned graphene heterostructures. *Adv. Funct. Mater.* **25**, 375-383 (2015).

11. Son, D., Lee, J., Qiao, S., Ghaffari, R., Kim, J., Lee, J. E., Song, C., Kim, S. J., Lee, D. J., Jun, S. W., Yang, S., Park, M., Shin, J., Do, K., Lee, M., Kang, K., Hwang, C. S., Lu, N. S., Hyeon,

T., Kim, D. H. Multifunctional wearable devices for diagnosis and therapy of movement disorders. *Nat. Nanotech.* **9**, 397-404 (2014).

12. Chortos, A., Liu, J., Bao, Z. A. Pursuing prosthetic electronic skin. *Nat. Mater.* **15**, 937-950 (2016).

13. Zhu, B. W., Wang, H., Leow, W. R., Cai, Y. R., Loh, X. J., Han, M. Y., Chen, X. D. Silk fibroin for flexible electronic devices. *Adv. Mater.* **28**, 4250-4265 (2016).

14. Kim, D. H., Lu, N. S., Ma, R., Kim, Y. S., Kim, R. H., Wang, S. D., Wu, J., Won, S. M., Tao, H., Islam, A., Yu, K. J., Kim, T. I., Chowdhury, R., Ying, M., Xu, L. Z., Li, M., Chung, H. J., Keum, H., Mccormick, M., Liu, P., Zhang, Y. W., Omenetto, F. G., Huang, Y. G., Coleman, T., Rogers, J. A. Epidermal electronics. *Science* **333**, 838-843 (2011).

15. Kaltenbrunner, M., Sekitani, T., Reeder, J., Yokota, T., Kuribara, K., Tokuhara, T., Drack, M., Schwodiauer, R., Graz, I., Bauer-Gogonea, S., Bauer, S., Someya, T. An ultra-lightweight design for imperceptible plastic electronics. *Nature* **499**, 458-463 (2013).

16. Liang, J. J., Li, L., Niu, X. F., Yu, Z. B., Pei, Q. B. Elastomeric polymer light-emitting devices and displays. *Nat. Photon.* **7**, 817-824 (2013).

17. White, M. S., Kaltenbrunner, M., Glowacki, E. D., Gutnichenko, K., Kettlgruber, G., Graz, I., Aazou, S., Ulbricht, C., Egbe, D. a. M., Miron, M. C., Major, Z., Scharber, M. C., Sekitani, T.,

Someya, T., Bauer, S., Sariciftci, N. S. Ultrathin, highly flexible and stretchable PLEDs. *Nat. Photon.* **7**, 811-816 (2013).

18. Sekitani, T., Nakajima, H., Maeda, H., Fukushima, T., Aida, T., Hata, K., Someya, T. Stretchable active-matrix organic light-emitting diode display using printable elastic conductors. *Nat. Mater.* **8**, 494-499 (2009).

19. Choi, S., Lee, H., Ghaffari, R., Hyeon, T., Kim, D. H. Recent advances in flexible and stretchable bio-electronic devices integrated with nanomaterials. *Adv. Mater.* **28**, 4203-4218 (2016).

20. Yang, J., Choi, M. K., Kim, D. H., Hyeon, T. Designed assembly and integration of colloidal nanocrystals for device applications. *Adv. Mater.* **28**, 1176-1207 (2016).

21. Colvin, V. L., Schlamp, M. C., Alivisatos, A. P. Light-emitting-diodes made from cadmium selenide nanocrystals and a semiconducting polymer. *Nature* **370**, 354-357 (1994).

22. Shirasaki, Y., Supran, G. J., Bawendi, M. G., Bulovic, V. Emergence of colloidal quantum-dot light-emitting technologies. *Nat. Photon.* **7**, 13-23 (2013).

23. Kagan, C. R., Lifshitz, E., Sargent, E. H., Talapin, D. V. Building devices from colloidal quantum dots. *Science* **353**, 885 (2016).

24. Supran, G. J., Song, K. W., Hwang, G. W., Correa, R. E., Scherer, J., Dauler, E. A., Shirasaki, Y., Bawendi, M. G., Bulovic, V. High-performance shortwave-infrared light-emitting

devices using core-shell (PbS-CdS) colloidal quantum dots. *Adv. Mater.* **27**, 1437-1442 (2015).

25. Gong, X. W., Yang, Z. Y., Walters, G., Comin, R., Ning, Z. J., Beauregard, E., Adinolfi, V., Voznyy, O., Sargent, E. H. Highly efficient quantum dot near-infrared light-emitting diodes. *Nat. Photon.* **10**, 253-257 (2016).

26. Mashford, B. S., Stevenson, M., Popovic, Z., Hamilton, C., Zhou, Z. Q., Breen, C., Steckel, J., Bulovic, V., Bawendi, M., Coe-Sullivan, S., Kazlas, P. T. High-efficiency quantum-dot light-emitting devices with enhanced charge injection. *Nat. Photon.* **7**, 407-412 (2013).

27. Caruge, J. M., Halpert, J. E., Wood, V., Bulovic, V., Bawendi, M. G. Colloidal quantum-dot light-emitting diodes with metal-oxide charge transport layers. *Nat. Photon.* **2**, 247-250 (2008).

28. Kim, T. H., Cho, K. S., Lee, E. K., Lee, S. J., Chae, J., Kim, J. W., Kim, D. H., Kwon, J. Y., Amaratunga, G., Lee, S. Y., Choi, B. L., Kuk, Y., Kim, J. M., Kim, K. Full-colour quantum dot displays fabricated by transfer printing. *Nat. Photon.* **5**, 176-182 (2011).

29. Choi, M. K., Yang, J., Kang, K., Kim, D. C., Choi, C., Park, C., Kim, S. J., Chae, S. I., Kim, T. H., Kim, J. H., Hyeon, T., Kim, D. H. Wearable red-green-blue quantum dot light-emitting diode array using high-resolution intaglio transfer printing. *Nat. Commun.* **6**, 7149 (2015).

30. Kim, B. H., Onses, M. S., Lim, J. B., Nam, S., Oh, N., Kim, H., Yu, K. J., Lee, J. W., Kim, J. H., Kang, S. K., Lee, C. H., Lee, J., Shin, J. H., Kim, N. H., Leal, C., Shim, M., Rogers, J. A. High-resolution patterns of quantum dots formed by electrohydrodynamic jet printing for light-emitting diodes. *Nano Lett.* **15**, 969-973 (2015).

31. Choi, M. K., Park, I., Kim, D. C., Joh, E., Park, O. K., Kim, J., Kim, M., Choi, C., Yang, J., Cho, K. W., Hwang, J. H., Nam, J. M., Hyeon, T., Kim, J. H., Kim, D. H. Thermally controlled, patterned graphene transfer printing for transparent and wearable electronic/optoelectronic system. *Adv. Funct. Mater.* **25**, 7109-7118 (2015).

32. Son, D., Chae, S. I., Kim, M., Choi, M. K., Yang, J., Park, K., Kale, V. S., Koo, J. H., Choi, C., Lee, M., Kim, J. H., Hyeon, T., Kim, D. H. Colloidal synthesis of uniform-sized molybdenum disulfide nanosheets for wafer-scale flexible nonvolatile memory. *Adv. Mater.* **28**, 9326-9332 (2016).

33. Bae, W. K., Kwak, J., Park, J. W., Char, K., Lee, C., Lee, S. Highly efficient green-light-emitting diodes based on CdSe@ZnS quantum dots with a chemical-composition gradient. *Adv. Mater.* **21**, 1690-1694 (2009).

34. Mahler, B., Spinicelli, P., Buil, S., Quelin, X., Hermier, J. P., Dubertret, B. Towards non-blinking colloidal quantum dots. *Nat. Mater.* **7**, 659-664 (2008).

35. Bae, W. K., Park, Y. S., Lim, J., Lee, D., Padilha, L. A., Mcdaniel, H., Robel, I., Lee, C., Pietryga, J. M., Klimov, V. I. Controlling the influence of Auger recombination on the performance of quantum-dot light-emitting diodes. *Nat. Commun.* **4**, 2661 (2013).

36. Lim, J., Jeong, B. G., Park, M., Kim, J. K., Pietryga, J. M., Park, Y.-S., Klimov, V. I., Lee, C., Lee, D. C., Bae, W. K. Influence of shell thickness on the performance of light-emitting devices based on CdSe/Zn1-XCdXS core/shell heterostructured quantum dots. *Adv. Mater.* **26**, 8034-8040 (2014).

요약 (국문초록)

피부 부착이 가능한 생체 통합 센서, 전하 트랩 메모리, 및 양자점 정보 디스플레이의 개발

최근 다양한 생리학적 데이터를 얻을 목적으로 인체에 붙일 수 있는 전자 장치를 개발하기 위해 많은 연구자들이 지속적인 노력을 기울여 왔습니다. 그러나 부드럽고 곡면으로 이루어 진 인체의 피부에 딱딱한 전자 장치를 장착하기 어려운 까닭에, 변형 가능한 전자 장치의 개발에 대한 필요성이 대두 되었습니다. 이와 관련하여, 유기 반도체 물질과 같은 본질적으로 유연한 물질뿐만 아니라 벌크 형태일 때에는 변형성이 부족하지만 그 두께 및 크기를 조절하여 변형이 용이하게 만들어진 나노 입자, 나노 와이어 및 나노 리본과 같은 초박형/초소형 물질이 인체 부착 형 전자 장치의 고성능 동작을 위한 주요 물질로 사용되기 시작하였습니다. 본 논문은 이러한 나노 물질을 다양한 목적으로 통합시킨, 피부와 유사한 기계적 성질을 가지는 피부 부착 형 전자 장치의 세 가지 예에 대한 연구 내용을 소개하고 있습니다.

첫 번째로, 초박막, 단결정 실리콘 나노 리본을 활용한 변형률, 압력 및 온도 센서 어레이와 더불어, 눅눅한 정도를 느낄 수 있는 습도 센서, 체온 모사를 위한 히터 및 신경 자극을 위한 신축성 다중 전극 어레이가 활용 된 스마트 인공 피부 보철 장치를 개발 하

였습니다. 본 연구에서 개발된 피부 보철 장치는 사람의 피부와 비슷한 신축성을 가진 동시에, 사람의 피부가 느낄 수 있는 외부 자극을 느낄 수 있고, 사람의 체온을 모사 하는 등, 최대한 사람의 피부와 비슷한 특성 및 성능을 지니도록 고안되어 향후 로봇 팔, 의수 등에 적용 가능할 거라 기대합니다.

두 번째로, 나노 결정으로 이루어진 플로팅 게이트를 갖춘 피부 부착 형 비휘발성 메모리 어레이를 개발 하였습니다. 나노 결정 플로팅 게이트는 Langmuir-Blodgett 방법을 사용하여 넓은 영역에 걸쳐 균일하게 조립됩니다. 균일한 나노 결정 플로팅 게이트는 성능의 균일성을 향상시킴과 동시에, 메모리 윈도우 마진과 정보 저장 성능을 향상시킵니다. 또한, 초박형 실리콘 나노 멤브레인으로 제작 된 회로를 기반으로 한 증폭기와 늘일 수 있는 피부 부착 형 전극을 이용하여 심전도를 측정하고 심장 박동 수의 변화를 개발된 메모리에 저장하는 데모를 선보였으며, 이는 향후에 피부 부착 형 소자를 의료 어플리케이션에 적용할 수 있는 가능성을 열었다 할 수 있습니다.

세 번째로, 피부에 붙일 수 있는 초박형 양자점 발광 다이오드 디스플레이를 개발하였습니다. 먼저 낮은 작동 전압으로 높은 휘도를 얻기 위해 양자점을 구조적으로 최적화 시켰습니다. 이렇게 최적화된 양자점을 활용하여 양자점 발광 다이오드 어레이로 구성된 양자점 디스플레이를 디자인 하였으며 이의 활용성을 보이기 위하여 문자, 숫자, 기호 및 애니메이션으로 구성된 다양한 패턴이 피부에 부착된 양자점 디스플레이를 통해 보여 질 수 있음을 시연 하였습니다. 개발된 양자점 디스플레이의 사용 중 안정성을 입증하기 위해 구겨짐 및 반복되는 구부림과 같은 다양한 기계적 변형에도 성능에 영

향이 없음을 확인 하였습니다. 또한, 입을 수 있는 전자 소자로의 활용성을 보이기 위하여 유연한 전자 장치를 디스플레이와 함께 집적하여 주변 온도 및 걸음 수를 측정하고 곧바로 피부에 부착된 디스플레이로 이를 확인할 수 있음을 시연 하였습니다.

본 논문에서 개발된 세 전자 장치는 미래의 피부 부착 형 전자 장치의 실현에 중요한 구성 요소입니다. 이번 연구 결과를 활용하여 변형 가능한 센서, 액추에이터, 데이터 저장 장치 및 디스플레이 분야에서 새로운 기회가 창출 되고, 완전히 통합된 피부 부착 형 전자 장치의 개발이 가속화되기를 기대합니다.

주요어: 변형 가능한 전자소자, 입을 수 있는 전자소자, 유연한 디스플레이, 피부 부착 형 데이터 저장소자, 인공 피부

학 번: 2012-30955